Spring 2003

Two Dimensional Numerical Simulation of Highly-Strained Hydrogen-Air Opposed Jet Laminar Diffusion Flames

Kyu C. Hwang
Old Dominion University

TWO DIMENSIONAL NUMERICAL SIMULATION OF HIGHLY-STRAINED HYDROGEN-AIR OPPOSED JET LAMINAR DIFFUSION FLAMES

by

Kyu C. Hwang
M. S., December 1995, Old Dominion University
B. S., May 1992, Virginia Polytechnique Institute and State University

A Dissertation Submitted in Partial Fulfillment of
the Requirement for the Degree of

DOCTOR OF PHILOSOPHY
in
MECHANICAL ENGINEERING

Old Dominion University
May 2003

Approved by

Dr. Surendra N. Tiwari (Director)

Dr. Gerald L. Pellett

Dr. Sushil K. Chaturvedi

Dr. Taj O. Mohieldin

Dr. Arthur C. Taylor III

ABSTRACT

TWO DIMENSIONAL NUMERICAL SIMULATION OF HIGHLY-STRAINED HYDROGEN-AIR OPPOSED JET LAMINAR DIFFUSION FLAMES

Kyu C. Hwang
Old Dominion University
Director: Dr. Surendra N. Tiwari

Many practical high speed combustion devices rely strongly on flow turbulence to enhance the mixing of fuel and oxidizer gases. And resultant turbulent diffusion flames can often be considered an ensemble of idealized laminar diffusion flamelets, stretched and distorted by turbulent eddys. Consequently, the structure, properties, and extinction limits of laminar counterflow diffusion flames have been the subject of research for many years. However, with the exception of a few recent and very limited studies, only one-dimensional numerical approaches have been used to approximate these flowfields, which may deviate significantly from 1-D ideality under certain conditions.

In this study, a detailed 2-D numerical technique is utilized to investigate the structure, and flame extinction and restoration characteristics of laminar hydrogen-air opposed jet diffusion flames, using both plug (uniform) and parabolic inflow boundary conditions for 3 millimeter jet tubes, spaced 6 millimeters apart and imbedded in low velocity coflows.

First, by using the most recent of two chemical kinetic models, excellent agreement was obtained between calculated distributions of temperature and major species, and published UV laser Raman scattering measurements, for 50% and 100% hydrogen-air flames over a range of input strain rates. Agreement with measured OH profiles was reasonably good at high strain rates, but generally less so at low strain rates. Also, the numerically simulated extinction limit of the

100% hydrogen-air diffusion flame was predicted within -5.1% (Jachimowski kinetic model) and +4.7%(Yetter et. al model) of a published grand-average measurement of global applied stress on the airside (average input velocity/tube-diameter), obtained using parabolic inflow profiles with a 2.7 millimeter tube opposed jet burner system.

Second, the study showed counterflow flame extinction limits for 100% hydrogen-air were most consistent when compared using flame core maximum radial strain rates on the center-line. By this measure, flame extinction occurred at similar strain rates (within 9.6%) for the two very different inflow boundary types. Also, the respective radial strain rates were linearly proportional to both centerline maximum axial strain rate and global applied stress rate, up to and just before the extinction state. Thus, both of these measurable reference rates provided a suitable relative basis for characterizing flame extinction limits.

However, the ratio of radial to axial strain rates varied significantly with input flow boundary types. The plug input flame resulted in a slightly smaller (0.92x) radial flame core strain rate on the centerline than the maximum axial strain rate, and this measure can be compared to the parabolic inflow flame which had a relatively larger (1.47x) radial strain rate. Furthermore, the respective radial/axial ratios (0.92 and 1.47) were not even close to the "classic" 0.50 ratio for the near-extinction state derived from the simplest 1-D stream-function approximation (Heimentz or potential flow) method. However, this same 1-D result was observed to apply closely (0.50 ratio) with 2-D nonreacting jet impingement cases for 3 millimeter opposed jets having both plug and parabolic inflows.

In essence, with the exception of the radial strain rate in the flame core, there was no other absolute centerline maximum axial strain rate, or radial strain rate at the stagnation point, or aver-

age global applied stress rate that uniquely defined the extinction state of a 100% hydrogen-air counterflow diffusion flame, independent of the input flow boundary types.

Finally, a previously observed ring-shaped post-extinction 100% hydrogen-air flame was numerically simulated when the stretching limit of the parabolic input velocity (for a 3 millimeter opposed jet) was exceeded beyond the critical extinction point. The post-extinction flame was tri-brachial, with fuel-rich and fuel-lean diffusion and premixed branches, displaying a quite different flame structure than the typical counterflow diffusion flame. The restoration of the diffusion flame was achieved at one-half of the extinction applied stress rate, which was in good agreement with the published measurement data. Thus, the large hysteresis that was clearly demonstrated by two distinct flames, each of which formed over a substantial range of identical inflow conditions, indicated that strain rate itself is not sufficient to characterize the local state of a laminar flamelet for a turbulent diffusion flame.

ACKNOWLEDGEMENTS

I would like to express my sincere gratitude to my advisor, Dr. Surendra N. Tiwari, for his guidance, support, and encouragement during the course of my doctoral study. I gratefully acknowledge the insight, guidance, and support of Dr. Gerald L. Pellett of the Hypersonic Air-breathing Propulsion Branch at the NASA Langley Research Center. He inspired my interest in combustion.

My appreciation extends to the rest of my committee members, Drs. Sushil K. Chaturvedi, Taj O. MOhieldin, and Arthur C. Taylor III for their timely support and encouragement toward my research. I am indebted to the Hypersonic Airbreathing Propulsion Branch at NASA Langley Research Center for the computer resources and, for most of all, opportunity as an on-site researcher throughout my doctoral study. I thank Dr. Saied Emami of Lockheed Martin Aeronautics for his technical expertise and encouragement. A special thanks to Mr. Roger W. Jones of NCI Information Systems, Inc. for the graphical supports.

Last, but by no means least, I would like to thank my wife and our parents for their understanding, love, and patience. I would also like to thank my daughter who gave me love, devotion, and happiness during my ordeal in completing this dissertation.

This work was supported by the NASA Langley Research Center through Institute for Scientific and Educational Technology (ISET) in Cooperative Agreement NCC1-349.

TABLE OF CONTENTS

LIST OF TABLES

LIST OF FIGURES

LIST OF SYMBOLS

A, B, C	Convective Jacobians
A_f, A_b	Preexponent Frequency-Factor of Arrhenius Finite Reaction Rate
C_j	Species Concentration
D_{ij}	Binary Diffusion Coefficient
$E_{f,b}$	Activation Energy of Arrhenius Expression
G	Gibbs Free Energy
H	Total Enthalpy
I	Identity Matrix
J	Jacobian Matrix
K	Thermal Conductivity
MW	Molecular Weight
$\dot{m}$	Mass Flow Rate
N_r	Number of Chemical Reactions
N	Number of Chemical Species
P	Pressure
q	Heat Flux
R_u	Universal Gas Constant
T	Temperature
U, V, W	Mean Velocity Components
X_i	Species Mole Fraction
Y_i	Species Mass Fraction

Greek Symbols

β	Preconditioning Parameter
Γ	Preconditioning Vector
μ	Viscosity
ν	Kinematic Viscosity
ρ	Density
τ	Shear Stress
ω_{ij}	Rate of Change in Species Concentration

CHAPTER I

INTRODUCTION

Significant research has been conducted in recent years to develop practical scramjet engines. Efforts have been directed toward enhancing the rate of fuel-air mixing in the engine which minimizes the combustor length and yet maximizes combustion efficiency. In very high speed vehicle configurations currently being considered, achieving a high combustor efficiency in a relatively smaller combustor length is quite difficult. The degree of fuel-air mixing achieved through natural convective and diffusive processes is reduced with higher combustor Mach numbers, leading to projected decrease in combustion efficiency and thrust. Consequently, many practical nonpremixed combustion devices, such as scramjets, rely on turbulence to increase the heat release and mass transfer rates [1].*

In turbulence, the bulk motion of flow causes the turbulent energy to continuously transfer from a large eddy to multiple small eddies, resulting in a large scale mixing of gases [2]. As a result, the separate regions of fuel and air are rolled up into the vortex within the eddy structure, causing these layers to interact in a molecular level through the diffusion process (Fig. 1.1). A flame exists along the interface region, stretched by a vorticity, where the large transverse gradients of temperature and species concentration occur. The chemical reaction occurs in the flame sheet inside vortex as initially separated fuel and oxidizer approach each other in a locally counter

---

* The numbers in brackets indicate references. In general, the AIAA Journal format has been adopted in preparing this dissertation.

flow manner. The local thickness of this region depends on the residence time and strength of the vortex, the local diffusion coefficients, and the chemical kinetics.

The turbulence/chemical interaction in such devices is quite complex, even from the statistical point of view, but their overall characteristics can be generalized through the relationship between the turbulence Reynolds and Damkohler numbers [3, 4]. The Damkohler number represents the ratio of turbulent length scale to chemical length scale, as shown in the Klimov-Williams diagram presented in Fig. 1.2. At smaller Damkohler number limit, the chemical reaction is relatively slow compared to the fluid dynamic time, causing reactant mixing and reactions to occur homogeneously. In this limit, the kinetic and transport properties depend strongly, in coupled manner, on the flow and gas characteristics. At large Damkohler number limit, or the weak turbulence region, the reaction rate is faster than the flow rate, assuming the local kinetics and transport associated with the combustion depend only on the gas characteristics. This allows the flame to be laminar in which case turbulence has little or no effect on its characteristics. Most of the supersonic combustion problems fall between these limits. In particular, the turbulent diffusion flame is considered closer to the larger Damkohler number limit. Consequently, the turbulent diffusion flame is often modeled as an ensemble of thin laminar flamelets, or a burning region, associated with an eddy stretched and distorted by the turbulent flowfield [5, 6]. This requires that the Kolmogorov scale, the smallest length scale of turbulent eddies, be much larger than the thickness of the reaction zone.

Unlike premixed flame, the counter flow diffusion flame does not propagate, and the burning velocity cannot be defined [7]. Initially, the diffusion flame has a separate fuel and oxidizer, and combustion occurs at the interface between the fuel and oxidant gases. The burning process depends more upon the rate of mixing than the rates of the chemical processes involved. There-

fore, the characteristics of diffusion flames are markedly dependent on the aerodynamics of the particular flow situation. Consequently, the complete spectrum of diffusion flame behavior cannot be discussed without invoking aerodynamic considerations. The chemical reaction rate within a diffusion flame is generally much faster than the diffusion velocity of the gas, resulting in a much smaller characteristic chemical time than a diffusion time. This indicates that the chemical reaction will occur in a narrow zone between the fuel and the oxidizer, where the concentrations of both reactants are very low.

1.1 Analytical Studies

In limited cases, the analytical study of the flame is done using the classic flame sheet theory. The theory assumes that the chemical reaction rate is infinitely fast, resulting in an infinitesimally thin reaction zone. This requires that the concentrations of fuel and oxidizer become zero at the flame surface. Specifically, the diffusion rates of the fuel and oxidizer at the flame surface must be in stoichiometric proportions, defining the locus of the flame surface. The theory significantly reduces the complexity of the governing equations by simplifying the terms associated with chemical kinetics. The first successful detailed analysis of a diffusion flame using this theory was given by Burke and Schumann [8]. They obtained a fairly accurate predication of the flame shape proving that the theory is quite useful for studying a laminar diffusion flame. Since then, the theory has been extended to be a powerful tool for theoretical studies, especially in boundary layer combustion, heat transfer, and burning rates of solid and liquid fuels [7]. However, there is a key problem concerning the diffusion flame which cannot be elucidated with the flame sheet theory. In the diffusion flame, the combustion rate is controlled by the rate at which the fuel and oxidizer diffuse to the reaction zone. The combustion rate increases with the diffusion rate which is

strongly dependent on the aerodynamics of flow, especially the convective flow velocity. Unfortunately, as the flow velocity is increased and the flame becomes more strained, the characteristic aerodynamic and diffusion times decrease to the point that the chemical reaction time can no longer be assumed infinitely fast, nullifying the local assumption of chemical equilibrium. This is clearly observed at flame extinction where the chemical reaction can not keep pace with the supply of fuel and oxidant, and the reaction ceases abruptly.

The method of matched asymptotic expansions has been used recently to solve the counterflow flame in the limit of large interaction between the hydrodynamics and chemical reactions in the reaction zone [9-13]. The analysis requires the chemical time scale to be short compared to the convective and diffusion time scales. However, the analysis assumes the combustion takes place within an asymptotically thin but not an infinitesimally thin region. This allows a Damkohler number of the second kind, which is the ratio of the diffusion time to the reaction time scales, to be large. Subsequently, as observed with one step large activation energy asymptotics, the activation energy, in chemical terms, can be related to the Damkohler number by a distinct asymptotic limit. Therefore, when the Damkohler number tends to infinity, the non-dimensional activation energy also tends to infinity. In addition, the asymptotic analysis with the reduced four step mechanism indicates that the activation energies do not play any role as an expansion parameter, and the overall thickness of the reaction zone is governed solely by the Damkohler number of the slowest reaction mechanism. Consequently, the complexity of the governing equations can be reduced by requiring the Damkohler number of the reactions to be large. However, the method is limited with the reduced chemical mechanism, allowing only a qualitative study of the flame.Yet, the method of Damkohler number asymptotics is very useful in predicting the overall characteristics of flame ignition and extinction.

1.2 Experimental Studies

Tsuji [7] designed an experimental configuration, the counterflow setup, where a flame is established in the forward stagnation region of a porous cylinder/sphere by injecting a fuel into the incoming oxidizer. Alternatively, Potter and Butler [14] developed an opposed jet configuration. Two gaseous jets flow toward each other, establishing a stagnation region with a flame between the fuel and the oxidizer. In the latter configuration, the distance between the two jets is chosen to be close enough to deduce the imposed strain rates, and far enough to stabilize the "free floating" flame and avoid flame anchoring. Both configurations are widely utilized because they are simple to set up experimentally, yet they provide a stable nonpremixed flame which allows the effects of aerodynamics on the flame to be examined independently. In these setups, the stretching of a flame by a flowfield is quantified by means of a single parameter, the strain rate, which reflects the relative rates of convective to diffusive transport characterizing the flow residence time within a flame, thus, allowing statistical and qualitative approaches to laminar diffusion flames.

For many years, extensive studies were performed experimentally with hydrocarbon systems, with emphasis on the flame ignition, structure, and extinction at various strained conditions. Recently, work has progressed to the hydrogen system because hydrogen is considered as an alternate fuel for high speed aerodynamic propulsion due to its high thrust per mass weight ratio, and for clean combustion technology [1, 15-17]. However, a majority of these works have been limited to obtaining empirical data on flame extinction. Few studies are available on the flame structure, and these are limited to the flame diagnostic measurements at highly diluted and/or lightly strained conditions [18, 19]. The lack of a wide spectrum in flame structural data, in particular, at highly concentrated fuel and highly strained conditions, is mainly due to the unique characteris-

tics of hydrogen. The hydrogen-air system has very high reaction and molecular diffusion rates, which produce a structurally thin flame (much thinner than the methane flame) - a typical pure hydrogen flame thickness at the extinction limit is less than one millimeter. As a result, high precision and high spatial resolution measurement technique are required for useful structure measurements. Also, a typical hydrogen-air flame is about 30 times stronger than methane-air; consequently, very high strain rates are needed to achieve extinction. Since the axial input strain rate and Reynolds number vary with velocity divided by diameter, and velocity times diameter, respectively, the achievement of high strain rates and laminar flow requires small nozzles or tubes with their dimensions on the order of 2-3 millimeters. In essence, these scale and flow requirements have contributed to the notable absence of hydrogen-air data for highly concentrated fuel [17].

Even with these difficulties and limitations, persistent efforts have been made to diagnose the hydrogen-air opposed jet diffusion flame using various measurement techniques. The temperature and the flow composition within a flame are effectively measured using Coherent AntiStokes Raman Scattering (CARS) [15] and Laser UV Raman techniques [20, 21]. The free radical concentration of OH in the diffusion flame is analyzed with the Planar Laser Induced Fluorescence (PLIF) technique [22-24]. The velocity field surrounding a flame is characterized using Laser Doppler Velocimetry (LDV) [15, 17, 18, 25, 26]. Recently, the Particle Imaging Velocimetry (PIV) technique, in conjunction with alumina and hollow silica particle seeding, was used to visualize the free floating jet impingement, and the resultant flow transition from axial to radial direction[27]. In addition, other nonintrusive techniques like focusing schlieren, shadowgraph and thermometry [27] are often deployed to characterize the overall structure of opposed jet flames.

Details of measurement techniques along with comprehensive literature reviews on the conterflow diffusion flames are collectively presented in [17, 22, 23].

1.3 One Dimensional Numerical Studies

The opposed jet laminar diffusion flame can be stabilized and characterized as a near one dimensional thin flame, with relatively ideal axial and radial strain rates. Thus, the problem is similar to a boundary layer type flow, in which viscous effects are restricted to the boundary layer, as opposed to the entire flowfield. Hence, the multi-dimensional governing equations representing the counterflow diffusion flame may be transformed into a set of ordinary differential equations of the boundary value type by using a stream function similarity transformation. This is usually accomplished by one of two methods. In the first approach, the hydrodynamics are solved by assuming a Hiemenz potential flow stream function, where the flowfield is characterized by a potential flow velocity gradient. In this case, both the axial and radial velocities are described by a single strain rate parameter [28, 29]. Unfortunately, the approach is unnecessarily restrictive due to the potential flow assumption automatically fixing the outer boundary conditions. At the same time, most flame experiments do not satisfy the ideal flow assumption, which can only be realized when infinite size nozzles are located infinitely far apart. The second (more recent) method removes the restriction of infinite separation distance by introducing a radial stream function, where axial velocity, temperature, species mass fraction, and the transport properties are functions of a changing radial distance along the axis of symmetry [30-32]. The equations are identical in both formulations but differ by the radial pressure gradient eigenvalues, which are computed in the recent approach but prescribed in the earlier one. The two formulations mainly differ in boundary conditions, which in the second formulation, allows for the specification of a finite jet

separation as well as the inlet flow composition, temperature, and velocity. The latter one dimensional approximation for plug flow simplifies the governing equations, and the applied boundary condition, and has been used extensively to study opposed jet and counterflow diffusion flames at various compositions of hydrogen and hydrocarbon fuels [28-30, 34-36].

The computational works accomplished in the diffusion flame area are vast, leaving a massive task of compiling their efforts. However, in the context of a laminar counter flow flame, comprehensive literature reviews, including fuel and air contamination effects, are documented in [7, 17]. Therefore, within the scope of the H_2-air flame, selected works that contribute to the body of knowledge about counterflow diffusion flames are discussed.

In the numerical study, the air side axial strain rate is recognized as an important parameter to characterize the flame [28-34]. It has been shown that the position of a diffusion flame, with respect to the stagnation plane, varies with fuel dilution, strain rate, and transport properties. The higher diffusivity of hydrogen causes the flame to locate farther upstream on the airside from the stagnation plane than for the methane flame. At the same time, the lower flammability limit of hydrogen-air causes the hydrogen flame to locate even farther upstream on the airside, which helps promote a much higher extinction limit than for the methane flame [17, 32].

The extinction of a nitrogen diluted flame at a lightly strained condition is recognized by excessive thermal heat loss to the flowfied, whereas the extinction of an undiluted highly strained flame is caused by severe reduction in the chemical reaction time within the flame. Thus, the extinction of a flame is very dependent on the transport properties [32] and chemical kinetics [34]. Also, both the ignition and extinction of strained hydrogen-air diffusion flames are significantly influenced by the input flow temperature. At a critical input temperature, the numerical results predict that the extinction of a flame is no longer possible; rather a prolonged existence of the

flame is observed.[37]. Overall, the effects of thermal diffusivity on the structure and extinction of a flame are negligible [32]. Although the radiational heat loss at low strain rate is considered be significant, influencing the overall characteristics of the flame structure and extinction, the radiational effect on the flame at highly strained conditions is reported to be small [38]. The addition of active nitrogen chemistry is found to have an insignificant effect, in that it exerts only a small influence on the flame structure and extinction. Nonetheless, its considerable influence on a flame is found at high pressure conditions where temperatures are higher [39].

The structure and extinction of hydrogen-air diffusion flames in the counterflow configuration have been investigated extensively with both full and reduced sets of chemical-kinetic mechanism at very low strain rates[39] and highly strained flow conditions [35]. The two step mechanism is proposed to be the minimum set required to compare with measured extinction data and shows good qualitative agreement [37, 39].

The effect of the inflow boundary of flame have been assessed experimentally, where the extinction data lie between the one dimensional potential and plug flow limits [34]. Extensive works are available for methane-air[16, 29, 30, 34] and hydrogen-air [27, 32, 35-37, 39, 40] using the potential flow assumption. The predicted extinction characteristics of the methane-air flame support the experimental data qualitatively. However, the measured extinction limits of the hydrogen-air flame for plug-flow (and parabolic inflow) velocity profiles are up to 40% lower than the calculated limits, and the discrepancies are more distinct as the flow becomes highly strained [17].

A major problem is that the potential flow assumption cannot properly account for the physics of a highly strained flame where the flow is most likely rotational and the input velocity profile differs from the assumed one. Numerous works have been performed using stream func-

tion assumptions, and extensive results are available for methane-air flames [30, 34] at various fuel compositions.

Nonetheless, few experimental results are available for the hydrogen-air flame, which are limited to highly diluted fuel compositions (<21% H_2) [35, 36, 42] with the exception of [17], which includes 14 to 100% H_2. The plug flow assumption presented an axial velocity in an eigen-function form, preventing an independent analytical expression for axial strain rates.

Overall, the one dimensional approximations generated discrepancy and unavailability in results that could be compared to the measurements. In addition, the one dimensional approximations required the flame thickness and its gap to the stagnation plane to be small compared to the characteristic dimension of a tube/nozzle. This is not true in the experiment, where the flame shows a finite thickness with offset gap considerable to the characteristic tube/nozzle dimension. This becomes most pronounced with the pure hydrogen-air flame near the extinction, where the flame thickness and its offset distance to the stagnation plane, are on the order of the tube/nozzle diameter.

1.4 Two Dimensional Numerical Studies

Recently, two dimensional numerical studies of nonpremixed opposed jet diffusion flames were reported. Zhao [40] and Zhao and Isaac [41] simulated the axisymmetric opposed jet flame, with both the parabolic and plug inflow velocity profiles, to characterize the resultant flowfield at an input strain rate of 100 per second condition. It included coflowing nitrogen streams that surround the fuel and air jets, preventing secondary combustion. The study utilized an explict finite volume technique to solve the Navier-Stokes equations, except the chemical source term was solved implicitly. Overall, the scheme was second order accurate, and the CHEMKIN database

was utilized to calculate the temperature dependent thermodynamic and transport properties. In their study, the difference in inflow velocity profiles had a large influence on maximum flame stretching, which also strongly depended on the jet separation distance. In fact, the flame stretching increased as the jet separation decreased. By comparing with non-reacting flows, the heat release in reacting flows influenced the surrounding flowfield, and consequently, strain rates. They observed the flame to respond easily to changes of fuel/air velocity ratio, coflow gas, and domain size. Overall, the study included only one global reversible reaction, indicating only qualitative insight on the methane-air flame.

Takagi et al. [43] studied the effects on flame curvature and preferential diffusion produced by a lean fuel or air microjet impinging on a flat opposed jet hydrogen-air diffusion flame. In this study, the perturbation of the diffusion flame had a characteristic length scale comparable to the flame thickness, making the resulting flame structure highly two dimensional. To complement the experimentation, a numerical simulation was obtained using a two dimensional upwind difference of third order accuracy for convective terms, but second order of central difference scheme for the diffusive terms, conjunction with CHEMKIN for thermodynamic and transport properties. The simulation was performed using sixteen reversible reactions and eight species; H_2, O_2, N_2, O, H, OH, H_2O, and HO_2. Notably, no coflowing gas was used. Even though the study included a detailed chemistry model, the simulation was limited to a single low plug flow type input of highly diluted fuel (15% in volume) with a relatively large tube diameter configuration (10 mm).

Kim and Kim [44] applied a two dimensional Navier-Stokes model together with detailed and temperature dependent chemical kinetics and transport properties, although their diffusivity was approximated with a constant Lewis number. They analyzed the effects of multidimensional-

ity on flame characteristics in a highly nitrogen-diluted (14% and 30% H_2 in volume) hydrogen-air counterflow setup. They employed a second order accurate central differencing scheme for the diffusive terms, and the TVD upwind scheme in a predictor-corrector sequence for the convective terms. Also, the operator splitting method was utilized to separate the chemical kinetic terms from the rest of equations. Their kinetic scheme utilized nine species and 21 steps tabulated in [42]. The model domain included a low speed pure nitrogen coflow gas which prevented secondary combustion. Their study was carried out to investigate the plug and parabolic inflow flame structures at low exit average velocities of 1.2 and 1.5 meters per second (or airside maximum strain rates of 260 and 280 per second) for the respective 14 and 30% H_2 inputs. They concluded that the jet exit profiles influenced the overall characteristics of the flame, including axial strain rate profile, thickness, peak temperature, and extinction characteristics. They reported that the parabolic inflow flame produced higher scalar dissipation rate, and larger oxidizer and fuel leakages in the flame, causing an earlier extinction of the flame than the plug inflow flame. Also, they clearly showed the multidimensionality of the opposed jet diffusion flames induced by plug and parabolic inflow conditions. Nonetheless, their works were limited to low speed, and with relatively large tube diameter and the separation distance where the relative flame thickness and Reynolds number assumptions associated with the one dimensional approximation would be applicable. As a result, their works did not offer any significance and uniqueness in results relating to the flame extinction and structure, otherwise provided with the two dimensional approach. In essence, their works would be repeated with proper modelling of the one dimensional approximation.

Numerically, Katta and Roquemore [22] investigated the unsteady characteristics of an opposed jet diffusion flame responding to sinusoidal input flow perturbations. The opposed jet had four centimeter diameter nozzles, and the perturbation was driven toward the flame to

observe interactions. Separately, sinusoidal input flows were used to examine the characteristics of flame extinction.

The investigation [22] was conducted with time dependent and axisymmetric Navier Stokes equations written in the cylindrical coordinate system. The finite difference form of the momentum equations were solved using the implicit QUICKEST scheme. The species and energy equations were solved using the hybrid scheme of upwind and central differencing. The pressure field was calculated using pressure Poisson equations. Also, the lower and upper diagonal matrix decomposition technique was employed to advance the computation in time. A detailed chemical kinetics model was used to describe the hydrogen-air combustion, using 13 species and 74 reaction equations that included nitrogen chemistry. The flame was simulated for 38% hydrogen fuel by volume, at fuel and air velocities (plug inflows) of 0.69 and 0.50 meters per second, respectively. In this analysis, a nonuniform staggered grid system, with a maximum grid density of ten per millimeter, was utilized to simulate a domain of four centimeters length and diameter.

In this study, Katta and Roquemore identified two types of unsteady flames; traveling and stationary. The traveling flame was observed as an uneven vortex generated from both ends of the nozzles, where a flame moved with the vortex heads. The stationary flame was observed when equal magnitude vortice from both nozzles impinged against each other. They reported that the stationary flame had a lower limit of extinction strain rate than the traveling flame. Overall, their works were limited to flames at highly diluted and lightly strained conditions.

Frouzakis et al. [45] simulated 20% hydrogen/nitrogen versus air laminar opposed jet counterflow diffusion flames. The study was performed at low speed (0.16 meters per second) using parabolic and uniform inflow velocity profiles at the nozzle exits. The diameter and the separation distance in this study were set at one centimeter. The simulation was conducted with a two

dimensional Navier-Stokes code, based on a spectral element method of spatial discretization, and a high order splitting scheme which separates the thermochemistry from the hydrodynamic sub-system. The hydrodynamic subsystem was solved explicitly in two dimensional form. However, the thermochemistry was simplified and solved implicitly in an ordinary differential form. Their computational model utilized detailed chemical kinetic and transport properties which were dependent of temperature. They examined the two dimensional effects of hydrodynamics, and assessed the validity of assumptions made in the traditional one-dimensional simulations for low input strain rate, lean hydrogen-air opposed jet diffusion flames. Although they reported that the structure of the flame is two dimensional, their results did not offer any major uniqueness in flame structure differentiating it from the one dimensional solution. Conclusively, their study indicated that the one dimensional approximation for uniform inflows would be more effective and ideal to analyze the highly diluted flames at lightly strained conditions.

Later, their numerical simulation were extended to investigate a 40% hydrogen/nitrogen versus air post-extinction flame, in the absence of an inert coflow curtain [46]. This study was performed at relatively low speed with a parabolic inflow velocity profile, and with the tube (nozzle) diameter and separation distance set at 2.7 millimeters. The ring shaped post-extinction flame, also a type of edge flame, was formed from the disk shaped diffusion flame by increasing the strain rate above the subcritical value for extinction. The edge flame formed as it propagated against a stream of partially premixed non-uniform opposed jet flows. The flame propagation velocity depended on the species mixture concentration gradient, flame curvature, and transport properties in the transverse direction. The edge flame system, often referred as a tribrachial flame, consisted of fuel rich and lean premixed arms that bound a central stoichiometric premixed flame, with a much weaker centrally-located trailing diffusion flame. This system shows much different

structural characteristics as compared to the preextinction diffusion flame. They found that the transition from edge to full diffusion flame (restoration) was not observed even at a substantially subcritical strain rate, due to higher local radial flow speed than the flame propagation speed. They showed the coexistence of two distinctive flames would be possible at identical input conditions, concluding that the strain rate as a parameter to determine the local reignition in flamelet models is not sufficient. They also compared their results with previous measurements of flame blowoff and restoration [17]. Their numerical flame extinction was achieved at a 24% lower oxidizer input velocity than the measurement [17], showing a modest discrepancy in results.

1.5 Objectives of Study

The hydrogen-air counterflow laminar diffusion flame has been extensively studied by many researchers from theoretical as well as numerical view points. In the context of opposed jet configurations, each numerical technique associated with its assumptions, applications, and limitations is examined in previous sections. So far, none of the techniques have been effective and adequate to address the extinction characteristics of highly concentrated (up to 100%) hydrogen-air diffusion flames. Even with the one dimensional numerical approximation for plug flow inputs, where the simplification in the equations was effective in addressing the overall characteristics of the opposed jet flames, the technique was not directly capable of defining a maximum airside strain rate to compare calculated and measured extinction characteristics. Few studies have investigated the problem two dimensionally, and these are confined to highly diluted fuel with relatively low to modestly strained flows, where the practicality and effectiveness of a two dimensional technique are often minimal.

The objective of this study is to investigate the axisymmetric 100% hydrogen-air opposed

jet laminar diffusion flame at moderate to high strain rates, using a two dimensional numerical technique to evaluate flame structure and extinction limits based on both plug and parabolic input flows. For a thorough investigation, the study is divided into three major parts. In the first part, the impingement characteristics of nonreacting opposed jet flows are examined using both plug and parabolic input velocity profiles. This part is extended to investigate the response of flow impingement characteristics to details of domain such as tube wall extinction, tube wall thickness, and radial domain geometry and boundary conditions, including mild wall transpiration co-flows and smooth walls with slip. In the second part of the study, the structure and extinction characteristics of a plug inflow induced, 100% hydrogen-air opposed jet diffusion flame are examined. It begins with the comparative investigation of impingement characteristics between nonreacting and reacting flows using a 4 step skeletal scheme by Clarke [48]. The reaction scheme is then extended to investigate the structure and multidimensionality of a flame at both lightly strained and extinction conditions using two 19-step chemistry models, one proposed by Yetter et al. [64] and later modified by Kim, Yetter and Dryer [49], and the other by Jachimowski [50]. This part includes the comparative assessment of chemical models as well as an assessment of the validity and limitations of the computational model, by comparing results with recent flame structure and extinction measurements. In the third part, the parabolic inflow induced hydrogen-air opposed jet flame is examined. It includes a comparative investigation of flame structure and extinction characteristics of parabolic- and plug flow-input flames. Also the responses of flame extinction to different chemistry models are assessed at the highly strained 100% hydrogen condition. Finally, the study is extended to investigate some detailed structural aspects of the postextinction flame.

The study is organized as follows: The general formulation of governing equations and the physical model are presented in Chap. II. Then, the methods of solution and the numerical model

are adduced in Chap. III. For the results, the nonreacting aspect of the opposed jet flows is addressed in Chap. IV. Then, the opposed jet laminar diffusion flames, induced by respective plug and parabolic inflow boundaries are discussed in Chaps. V and VI. Finally, concluding remarks on the 100% hydrogen-air opposed jet diffusion flame are given in Chap. VII.

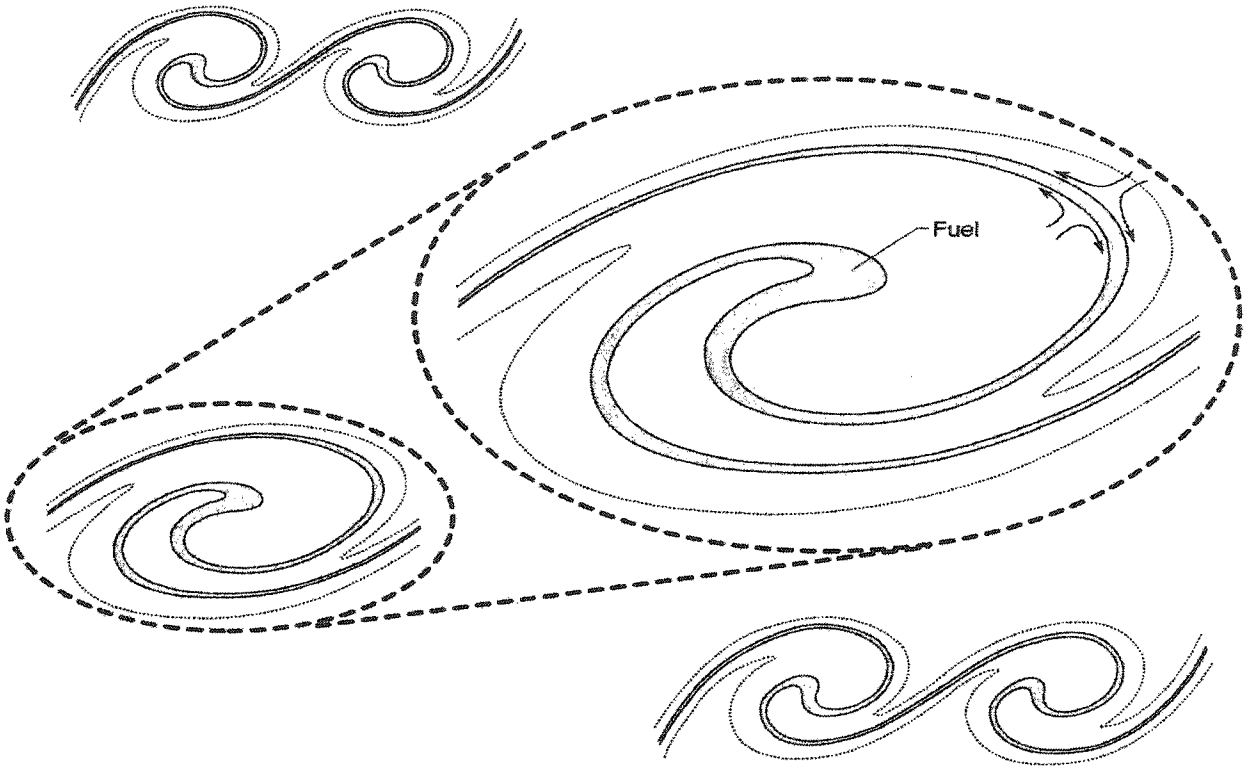

Fig. 1.1 A schematic representation of mixture of fuel and oxidizer in a vortex.

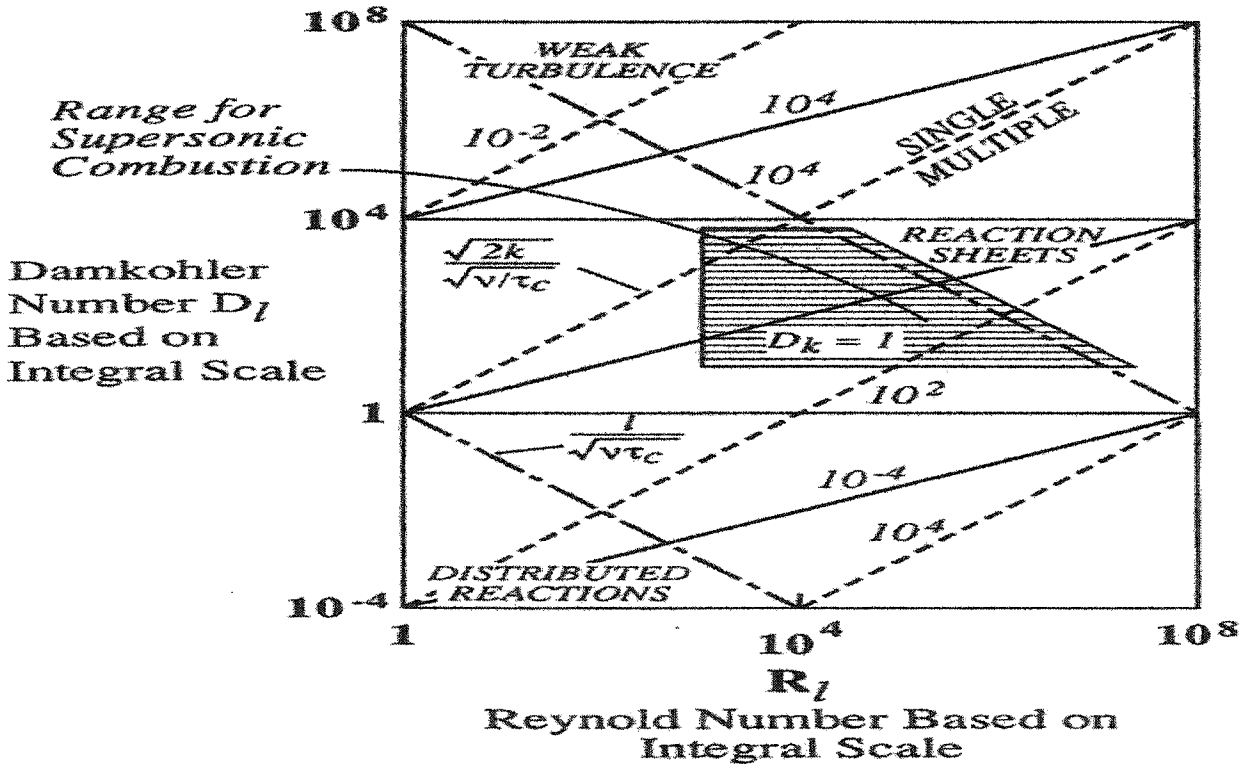

Fig. 1.2 The parametric characterization of nonpremixed turbulent combustion [3, 4].

CHAPTER II

PHYSICAL MODEL AND GENERAL FORMULATIONS

In the mixing and combustion of high speed flows, the highly convoluted laminar flame sheets, presented in a locally nonpremixed field, are subject to stretching and distortion by turbulence. Therefore, a detailed analysis of the flame structure and extinction characteristics of laminar flames, under the influence of strained flow conditions, is needed to properly model the interaction between aerodynamics and chemistry. Alternately, the opposed jet configuration is used here to explore their interaction. Unlike co-flow configurations, where the heat and mass transfer rates are usually very low, the opposed jet configuration provides a strong forced convection that enhances the mixing of gases. Most importantly, the opposed jet configuration allows for direct assessment of the effects of aerodynamic strain on the diffusion flame structure, while being free from interactions between the flame and the burner rim. The opposed jet flames observed in the laboratory have shown that the "all important" primary disk flame (within one nozzle diameter) typically has a subtle two dimensional structure, with a radial variation in axial velocity and hence composition and temperature fields. Clearly, the finite nature of hydrogen-air combustion depends somewhat on two dimensional convective and diffusive processes in the primary flame. Therefore, to assess these two dimensional characteristics, the axisymmetric (2-D) compressible Navier-Stokes and species continuity equations are used to describe multiple species undergoing a finite rate chemical reaction.

In this chapter, the details of the physical model are presented in Sec. 2.1. The general formulation of the governing equations is discussed in Sec. 2.2. Next, the details of thermodynamics

and transport are addressed in Sec. 2.3. Finally, the theoretical and mathematical descriptions of the chemical model, along with three different hydrogen-air combustion mechanisms are presented in Sec. 2.4.

2.1 Physical Model

Figure 2.1 represents a physical domain of an opposed jet configuration. The fuel and oxidizer tubes of equal size and length are spaced 6 millimeters apart. These are close enough to deduce imposed strain rates, and far enough to stabilize free floating flames, especially in the laboratory. The length and diameters of the tubes are 3 millimeters, to generate laminar flames at high strain rates, similar to 2.7 millimeter tube and nozzle opposed jet burners in [17]. The tube walls are assumed to be nonreactive and adiabatic, with the wall thickness 6% of tube radius. The fuels used are various compositions of hydrogen diluted by nitrogen, however, the oxidizer consists of 21% oxygen and 79% nitrogen by volume. In a typical computational series, the air velocity starts out low and is increased in increments until flame extinction is achieved. The fuel velocity corresponding to the air input is calculated based on the one dimensional approximation of the momentum equation. In this study, the input velocity profiles are either parabolic or plug-like, with only an axial component. The coflowing zone, with a 16 millimeter outer diameter, is placed on both sides of the domain surrounding the tubes. The coflow has a uniform input velocity of 0.1 meters per second. The coflow zone is created to prevent secondary combustion and a flame-tube wall interaction. More importantly, the coflow velocities provide additional axial balance of the flame, thus stabilize the flame in downstream (radial) flow. The domain is extended 50 millimeters downstream to capture the whole flame structure, minimizing the adverse downstream boundary effects on the flame. The nonreacting and isothermal (300K) wall is assigned to

both sides of the domain in the far downstream, guiding the hot combusted gases to the domain exit. The domain is initially at 300K and 101.3KPa filled with pure nitrogen.

2.2 Mathematical Model

The time dependent compressible Navier-Stokes and species transport equations for a chemically reacting gas of N species, written in general curvilinear coordinates, are expressed as

$$\frac{\partial}{\partial t}\tilde{Q} + \frac{\partial}{\partial \xi}(\tilde{E} - \tilde{E}_v) + \frac{\partial}{\partial \eta}(\tilde{F} - \tilde{F}_v) + \frac{\partial}{\partial \zeta}(\tilde{G} - \tilde{G}_v) = \tilde{H} \tag{2.1}$$

where the conservative fluxes $\tilde{Q}$, $\tilde{E}$, $\tilde{E}_v$, $\tilde{F}$, $\tilde{F}_v$, $\tilde{G}$, $\tilde{G}_v$, and $\tilde{H}$ are defined as

$$\tilde{Q} = Q/J$$

$$\tilde{E} = \frac{1}{J}(\xi_t Q + \xi_x E + \xi_y F + \xi_z G)$$

$$\tilde{E}_v = \frac{1}{J}(\xi_x E_v + \xi_y F_v + \xi_z G_v)$$

$$\tilde{F} = \frac{1}{J}(\eta_t Q + \eta_x E + \eta_y F + \eta_z G)$$

$$\tilde{F}_v = \frac{1}{J}(\eta_x E_v + \eta_y F_v + \eta_z G_v)$$

$$\tilde{G} = \frac{1}{J}(\zeta_t Q + \zeta_x E + \zeta_y F + \zeta_z G)$$

$$\tilde{G}_v = \frac{1}{J}(\zeta_x E_v + \zeta_y F_v + \zeta_z G_v)$$

$$\tilde{H} = \frac{1}{J}H$$

In the expressions of Eq.(2.1), τ, ξ, η, and ζ are the time and spatial coordinates in generalized coordinates, and ξ_t, η_t, and ζ_t are the grid speed terms. The variables, ξ_x, ξ_y, ξ_z, η_x, η_y, η_z, ζ_x, ζ_y, and ζ_z are the metric terms and J is the transformation Jacobian. The vectors Q, E, F, G, E_v, F_v, G_v, and H are defined as

$$Q = (\rho, \rho u, \rho v, \rho w, \rho E, \rho Y_1 \ldots, \rho Y_{N-1})^T$$

$$E = (\rho u, \rho u^2 + P_g, \rho uv, \rho uw, (\rho E + P_g)u, \rho uY_1, \ldots, \rho uY_{N-1})^T$$

$$F = (\rho v, \rho uv, \rho v^2 + P_g, \rho vw, (\rho E + P_g)v, \rho vY_1, \ldots, \rho vY_{N-1})^T$$

$$G = (\rho w, \rho uw, \rho vw, \rho w^2 + P_g, (\rho E + P_g)w, \rho wY_1, \ldots, \rho wY_{N-1})^T$$

$$E_v = (0, \tau_{xx}, \tau_{xy}, \tau_{xz}, u\tau_{xx} + v\tau_{xy} + w\tau_{xz} + q_x, S_{x1}, \ldots, S_{xN-1})^T$$

$$F_v = (0, \tau_{yx}, \tau_{yy}, \tau_{yz}, u\tau_{yx} + v\tau_{yy} + w\tau_{yz} + q_y, S_{y1}, \ldots, S_{yN-1})^T$$

$$G_v = (0, \tau_{zx}, \tau_{zy}, \tau_{zz}, u\tau_{zx} + v\tau_{zy} + w\tau_{zz} + q_z, S_{z1}, \ldots, S_{zN-1})^T$$

The source term H is

$$H = (0, 0, 0, 0, 0, \omega_1, \ldots, \omega_{N-1})^T$$

where ρ, P, U, V, W, and Y_i represent the density, pressure, Cartesian velocity components, and species mass fraction, respectively. The ω_i is the chemical source term reflecting a rate of change in species i due to chemical reactions.

The total internal energy is defined as

$$E_t = e + \frac{1}{2}(u^2 + v^2 + w^2)$$

where e is the thermodynamic internal energy. The stress, heat, and species diffusion fluxes are given by

$$\tau_{xx} = 2\mu\frac{\partial u}{\partial x} - \frac{2}{3}\mu\left(\frac{\partial u}{\partial x} + \frac{\partial v}{\partial y} + \frac{\partial w}{\partial z}\right)$$

$$\tau_{yy} = 2\mu\frac{\partial v}{\partial y} - \frac{2}{3}\mu\left(\frac{\partial u}{\partial x} + \frac{\partial v}{\partial y} + \frac{\partial w}{\partial z}\right)$$

$$\tau_{zz} = 2\mu\frac{\partial w}{\partial z} - \frac{2}{3}\mu\left(\frac{\partial u}{\partial x} + \frac{\partial v}{\partial y} + \frac{\partial w}{\partial z}\right)$$

$$\tau_{xy} = \mu\left(\frac{\partial u}{\partial y} - \frac{\partial v}{\partial x}\right)$$

$$\tau_{xz} = \mu\left(\frac{\partial u}{\partial z} - \frac{\partial w}{\partial x}\right)$$

$$\tau_{yz} = \mu\left(\frac{\partial v}{\partial z} - \frac{\partial w}{\partial y}\right)$$

$$q_x = k\frac{\partial T}{\partial x} + \rho\sum_{i=1}^{N} h_i D_{im}\frac{\partial Y_i}{\partial x}$$

$$q_y = k\frac{\partial T}{\partial y} + \rho\sum_{i=1}^{N} h_i D_{im}\frac{\partial Y_i}{\partial y}$$

$$q_z = k\frac{\partial T}{\partial z} + \rho \sum_{i=1}^{N} h_i D_{im} \frac{\partial Y_i}{\partial z}$$

$$S_{xi} = \rho D_{im} \frac{\partial Y_i}{\partial x}$$

$$S_{yi} = \rho D_{im} \frac{\partial Y_i}{\partial y}$$

$$S_{zi} = \rho D_{im} \frac{\partial Y_i}{\partial z}$$

where T, μ, k, and D_{im} are the temperature, viscosity, thermal conductivity and effective binary diffusivity, respectively.

It is well known that numerical methods developed for compressible flows are often ineffective at low Mach numbers [51]. There are two reasons for this difficulty. First, the system's eigenvalues become stiff at low flow velocities due to large disparity between the acoustic wave speed, u+a, and the convective fluid speed, u. In theory, this can be circumvented by using a large Courant-Friedrichs-Lewy (CFL) number in the implicit scheme. However, this causes the large approximate factorization errors in a discretized system that leads to a different and unintended solution. In addition, the wide disparities among eigenvalues yield multiple CFL numbers, posing a difficulty determining the optimal numbers.

Alternately, a time preconditioning technique is proposed to increase the convergence rate without raising the CFL number. There are two basic views of preconditioning methods [52, 53], but only one method is considered here in context of the central difference scheme. A matrix form of a preconditioning term is applied to the time derivatives in the system of governing equations

to rescale the speed of acoustic waves down towards the fluid speed. Thus, the convergence of the iterations can be accelerated. This method operates in a pseudo-transient environment devoiding the time accurate solution. But, once the convergence is achieved, the solution becomes identical to the original solution.

The second difficulty associated with low Mach number flow is often found with the pressure gradient term in the momentum equations. The nondimensional pressure term is of order $1/M^2$ while the convective term is of order unity in the nondimensional momentum equations. Consequently, when the Mach number approaches zero, the pressure term becomes singular yielding large round-off errors. This behavior smears the pressure variation and often produces inaccurate solutions. To circumvent this problem, the pressure term is rewritten with the gage pressure to account for the dynamic pressure responsible for the velocity-pressure coupling in the momentum equations. With this representation, the magnitude of the pressure gradient term becomes of order unity as the Mach number approaches zero, therefore, the singularity is removed from the system [51]. The static pressure in the system is then calculated independently as follows:

$$P = P_0 + P_g(x,y,z,t)$$

where P_0 represents either freestream or upstream pressure.

In conventional compressible flow algorithms, pressure is not one of the dependent variables but it is calculated from the dependent variables and the equation of state. This is not a preferable approach at low Mach numbers, because roundoff errors are introduced in P and P_g, nullifying the pressure decomposition measure. To avoid such a problem, gage pressure becomes a dependent variable and is solved directly. Therefore, Eq(2.1) is rewritten as

$$\Gamma\frac{\partial}{\partial\tau}\hat{Q} + \frac{\partial}{\partial t}\tilde{Q} + \frac{\partial}{\partial\xi}(\tilde{E}-\tilde{E}_v) + \frac{\partial}{\partial\eta}(\tilde{F}-\tilde{F}_v) + \frac{\partial}{\partial\zeta}(\tilde{G}-\tilde{G}_v) = \tilde{H} \qquad (2.2)$$

where τ is the pseudo time and the primitive variable vector, $\hat{Q}$, is defined as

$$\hat{Q} = \frac{1}{J}(P_g, u, v, w, E, Y_1 \ldots, Y_{N-1})^T$$

The preconditioning matrix term Γ is expressed as

$$\Gamma = \begin{bmatrix} 1/\beta & 0 & \ldots & \ldots & \ldots & \ldots & \ldots & \ldots & \ldots & 0 \\ u/\beta & \rho & 0 & \ldots & \ldots & \ldots & \ldots & \ldots & \ldots & 0 \\ v/\beta & 0 & \rho & 0 & \ldots & \ldots & \ldots & \ldots & \ldots & 0 \\ w/\beta & 0 & 0 & \rho & 0 & \ldots & \ldots & \ldots & \ldots & 0 \\ h/\beta - 1 & \rho u & \rho v & \rho w & \rho & 0 & \ldots & \ldots & \ldots & 0 \\ Y_1/\beta & 0 & 0 & 0 & 0 & \rho & 0 & \ldots & \ldots & 0 \\ \ldots & 0 & \ldots & \ldots & \ldots & 0 & \rho & 0 & \ldots & \ldots \\ Y_{N-1}/\beta & 0 & \ldots & \ldots & \ldots & \ldots & \ldots & \ldots & 0 & \rho \end{bmatrix}$$

where the quantity β is a preconditioning parameter for rescaling the eigenvalues of a new system of equations, and is defined as

$$\beta = u^2 + v^2 + w^2$$

and h is the specific enthalpy of the mixture gas defined as;

$$h = e + \frac{p}{\rho}$$

When a steady state solution is of interest, the physical time term is effectively dropped and only the pseudo time term is retained.

2.3 Thermodynamic and Transport Models

The mass averaged constant pressure specific heat and transport coefficients are expressed in the fourth order polynomial function of temperature as

$$\left(\mu_i, k_i, \frac{C_{pi}}{R_u}\right) = \sum_{s=1}^{4} (C_{\mu s}, C_{ks}, C_{ps}) T^s \tag{2.3}$$

where $C_{\mu s}$, C_{ks}, and C_{ps} are the curve fitted constants for viscosity, thermal conductivity, and specific heat and are derived with the least squares fit method [54, 55]. In this study, these coefficients are obtained in the temperature range between 200K and 3500K. The mixture specific heat is evaluated by a mass weighted summation over all species, i.e.,

$$C_p = \sum_{i=1}^{N} C_{pi} Y_i \tag{2.4}$$

whereas, the pressure of a gas mixture is obtained from the Dalton's law of partial pressure as

$$P = \rho R_u T \sum_{i=1}^{N} \frac{Y_i}{W_i} \tag{2.5}$$

The global enthalpy and total energy are derived based on the specific heat as

$$h_i = h_{f_i} + \int_{T_{ref}}^{T} C_{pi} dT \tag{2.6}$$

$$E_t = \sum_{i=1}^{N} Y_i h_i - \frac{P}{\rho} + \frac{1}{2}(u^2 + v^2 + w^2) \tag{2.7}$$

and

$$\sum_{i=1}^{N} Y_i = 1$$

Since the total energy and the specific heat coefficients for a gas mixture are known, the temperatures in the domain are inversely calculated using the Newton's method.

The thermal conductivity and the viscosity of a mixture are calculated using the Wilke's mixing rule, i.e. [56],

$$\mu, k = \sum_{i=1}^{N} (\mu_i, k_i) / \left[\frac{1}{x_i} \sum_{j=1}^{N} x_j \phi_{ij} \right] \tag{2.8}$$

where ϕ is the inter-collisional parameter and is given as

$$\phi_{ij} = \left[2\sqrt{8\left(1 + \frac{W_i}{W_j}\right)} \right]^{-1} \left[1 + 4\frac{\sqrt{(W_j \mu_i)}}{\sqrt{(W_i \mu_j)}} \right]^2$$

The binary mass diffusion coefficients are obtained using the Chapman-Enskog theory [57] for dense gases as

$$D_{ij} = 0.0018583 \sqrt{\frac{1}{W_i} + \frac{1}{W_j}} \left[\frac{T^{1.5}}{P \sigma^2{}_{ij} \Omega_{ij}} \right] \tag{2.9}$$

where the effective collision integral factor and temperature are approximated by

$$\Omega_{ij} = \frac{1}{T_D^{\,0.145}} + \frac{1}{(T_D + 0.5)^2}$$

$$T_D = \frac{T}{\sqrt{T_i T_j}}$$

The value of the effective collision diameter σ is taken to be an average of the separate molecular properties of each species, giving

$$\sigma_{ij} = \frac{1}{2}(\sigma_i + \sigma_j)$$

Once the binary diffusion coefficients for all species combinations are known, the overall diffusion coefficients are computed by lumping all of the species together into a mixture. An approximate form of the diffusion coefficients is as follows:

$$D_{im} = (1 - x_i) \Big/ \left(\sum_{j \neq 1}^{N} \frac{x_j}{D_{ij}} \right) \tag{2.10}$$

The diffusion velocity of each species is, then, found using Fick's law as

$$u_k Y_i = -D_{im} \frac{\partial Y_i}{\partial x_k} \tag{2.11}$$

2.4 Chemical Model

2.4.1 Theoretical Formulation

For a set of M elementary reactions involving N species, the finite rate chemical reaction can be expressed in the following general form

$$\sum \Upsilon'_{ij} C_i \leftrightarrow \sum \Upsilon''_{ij} C_i \tag{2.12}$$

where Υ'_{ij} and Υ''_{ij} are the stoichiometric coefficients for species i appearing as a reactant in the jth forward and backward reactions, respectively. The law of mass action states that the rate change in the concentration of a species i by a reaction j is given by

$$(\dot{C}_i)_j = (\Upsilon''_{ij} - \Upsilon'_{ij}) \left(K_{f_j} \prod C_i^{\Upsilon'_{ij}} - K_{b_j} \prod C_i^{\Upsilon''_{ij}} \right) \tag{2.13}$$

The forward and backward reaction rates are computed from the modified Arrhenius law,

$$K_{f_j, b_j} = A_{f_j, b_j} T^{N_{f_j, b_j}} e^{-\frac{E_{f_j, b_j}}{R_u T}} \tag{2.14}$$

Alternately, the influence of other bodies on a particular chemical reaction is modeled using a third body efficiency correction as

$$K_{f_j, b_j} = K_{f_j, b_j} \sum_{i=1}^{N} (Third)_{ij} C_i \tag{2.15}$$

The rate change in the concentration of a species i by all reactions is found by summing the contribution from each reaction. Consequently, the production rate of a species i is expressed as

$$\dot{\omega}_i = W_i \sum_{j=1}^{M} (\dot{C}_i)_j \tag{2.16}$$

It is common to have one reaction rate constant (i.e. forward reaction rate), and to calculate the other (i. e. backward reaction rate). This is done with the molar based equilibrium constant, i.e.,

$$K_c = \left[\exp\left(-\frac{\Delta G^o}{R_u T}\right)\right][R_u T]^{\sum \Upsilon' - \sum \Upsilon''}$$

where the molar Gibbs free energy is defined by the following expression

$$\Delta G^o = \sum \Upsilon''_i g_i - \sum \Upsilon'_i g_i$$

and the partial molar Gibbs free energy, g_i, is calculated from the polynomial representation as a function of temperature. Therefore,

$$K_{bi} = \frac{K_{fi}}{K_{ci}}$$

2.4.2 Hydrogen-Air Chemistry Models

The combustion process occurs at a finite rate when a fuel burns with oxidizer. From a microscopic point of view, the combustion begins when molecules are dissociated and recombined through a collisional process forming reactive species called free radicals (with unpaired electrons) which set off a series of reactions (chain initiation). Through complex phases of radical enlargement (chain branching), stagnation (chain propagation), and destruction (chain termination) of free radicals, the combustion process continues until a deficiency in fuel or oxidizer is reached. At this state, the vast majority of radicals are either recombined to form a stable species or destroyed by the collisions with a surface. Artificially, these processes can be represented by means of a set of chemical reactions known as the chemical mechanism.

In this study, three different sets of hydrogen-air combustion mechanisms are considered. The first is a reversible skeletal mechanism proposed by Clarke in 1963 [48], and is shown in Table 2.1. The mechanism was chosen because it has four steps which provide a relatively simple scheme in computational calculation. The scheme is ideal for analyzing a near equilibrium diffusion flame which is often observed at low strain conditions. In context, the mechanism is utilized to qualitatively characterize the difference in reacting and nonreacting opposed jet flows at low strain conditions. The mechanism includes seven species; H_2, H, H_2O, OH, O, O_2, and the inert gas N_2.

The next two mechanisms in consideration were proposed by Jachimowski [50] and Yetter et al. [49, 64], and are presented in Tables 2.2 and 2.3, respectively. These models from the early 1990's were chosen because they are well established and provide very recent kinetic coefficients. So far, no other well established models are found in the recent literature. Both models are similar since the mechanisms include nineteen step hydrogen-air combustion excluding the nitrogen

chemistry. However, each model stems from a different purpose. The Jachimowski model was originally proposed to analyze combustion problems associated with propulsion systems required to operate at flight speeds up to Mach 25. In extent, the model was proposed and has been widely used to determine ignition delay times, burning velocities, and the combustor performance of a scramjet. Alternately, the Yetter et al. model was proposed to provide a comprehensive reaction mechanism for wide range of hydrogen-air combustion problems. The coefficients were compiled based on shock tube and various type reactor experiments (where transport effects are negligible) for the temperature range of 700-2900K, fuel-oxidizer equivalence ratios of 0.0005-6.0, and pressures between 0.3 and 2.2 atmospheres. In essence, the two models are similar since both have nine species including H_2, O_2, H, O, OH, H_2O, HO_2, H_2O_2, and N_2; and dissimilar in a few of their reaction rate coefficients and especially in third body recombination efficiencies for steam (see rate comparison at 1400K in Fig. 2.2).

The collision efficiencies of species included in the three models are accounted for by including Chaperon efficiencies in the total concentration. Recently, Warnatz [58] reported that the species associated with different reaction equations exhibit different values of efficiency factor. Clearly, this has been observed with the reaction equation where the third body is chemically interacting with the collision complex, i.e., $2H + H_2 \rightarrow 2H_2$. Also, another study by Hsu [59] evidenced that the Chaperon efficiencies for a reaction like $H + O_2 + M$ vary with the temperature, showing a strong temperature dependency. However, due to the lack of accurate data on efficiency factors, the third body efficiency for each species associating with different recombination/dissociation reaction equations is assumed identical and independent of temperature for each respective model.

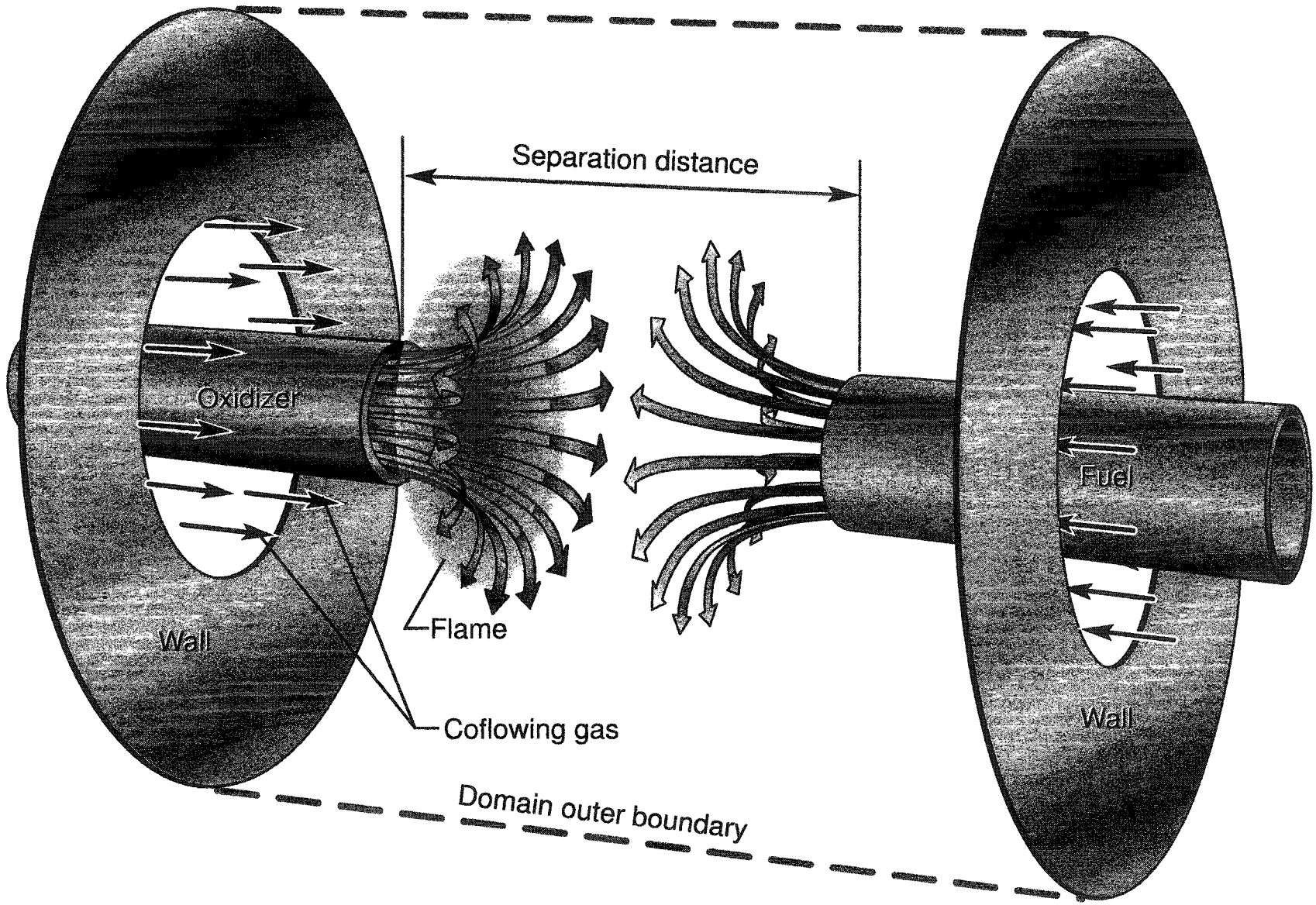

Fig. 2.1 Schematic of physical domain.

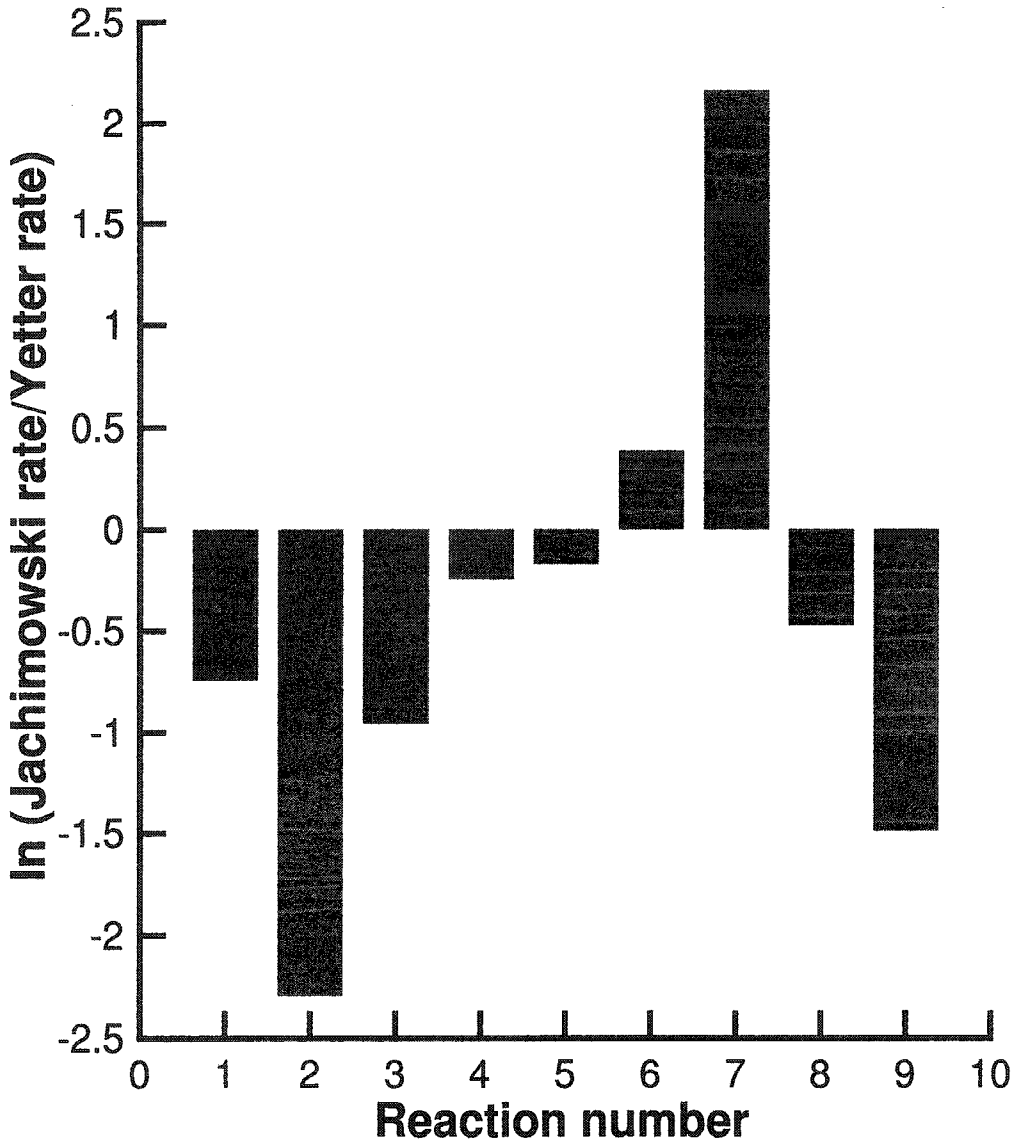

1. $2O + M \rightarrow O_2 + M$
2. $O + H + M \rightarrow OH + M$
3. $H + OH + M \rightarrow H_2O + M$
4. $H + O_2 + M \rightarrow HO_2 + M$
5. $HO_2 + H \rightarrow 2OH$
6. $HO_2 + OH \rightarrow H_2O + O_2$
7. $2HO_2 \rightarrow H_2O_2 + O_2$
8. $H_2O_2 + O \rightarrow OH + HO_2$
9. $H_2O_2 + OH \rightarrow H_2O + HO_2$

THIRD BODY EFFICIENCIES

JACHIMOWSKI MODEL
$H_2O = 16$; H2 = 2.5; OTHERS = 1

YETTER ET AL MODEL
$H_2O = 12$; H2 = 2.5; OTHERS = 1

Fig. 2.2 Rate comparison between Yetter et al. and Jachimowski chemical kinetic models at T=1400K.

Table 2.1 Reduced set of hydrogen-air chemistry model by Clarke [48].

#	Reaction	A	B	E
1_f	$H_2 + M <-> 2H + M$	1.85E17	-1.00	-54000
2_f	$H_2 + OH <-> H_2O + H$	3.00E11	0.00	-3020
3_f	$H + O_2 <-> OH + O$	3.00E11	0.00	-8810
4_f	$O + H_2 <-> OH + H$	3.14E11	0.00	-4030
1_b	$2H + M <-> H_2 + M$	1.00E10	0.00	0
2_b	$H_2O + H <-> H_2 + OH$	1.33E12	0.00	-10950
3_b	$OH + O <-> H + O_2$	2.48E10	0.00	-660
4_b	$OH + H <-> O + H_2$	1.30E11	0.00	-2490

*Reaction rate coefficients are in K = ATBexp(E/T).
*Related units are in moles, centimeters, seconds, kelvins, and joules.
*All species have a third body collision efficiency of unity.

Table 2.2 Hydrogen-air chemical kinetic model by Jachimowski [50].

#	Reaction	A	B	E	Third Body
1	$H + O_2 <-> O + OH$	2.20E14	0.00	-8454	
2	$O + H_2 <-> H + OH$	5.06E04	2.67	-3165	
3	$OH + H_2 <-> H + H_2O$	2.16E08	1.51	-1726	
4	$2OH <-> O + H_2O$	1.50E09	1.14	0	
5	$2H + M <-> H_2 + M$	7.30E17	-1.00	0	H_2/2.5/H_2O/16.0
6	$2O + M <-> O_2 + M$	1.10E17	-1.00	0	H_2/2.5/H_2O/16.0
7	$O + H + M <-> OH + M$	2.60E16	-0.60	0	H_2/2.5/H_2O/16.0
8	$H + OH + M <-> H_2O + M$	8.62E21	-2.00	0	H_2/2.5/H_2O/16.0
9	$H + O_2 + M <-> HO_2 + M$	2.30E18	-1.00	0	H_2/2.5/H_2O/16.0
10	$H_2 + O_2 <-> H + HO_2$	7.00E13	0.00	-28580	
11	$HO_2 + H <-> 2OH$	1.50E14	0.00	-503	
12	$HO_2 + O <-> OH + O_2$	2.00E13	0.00	0	
13	$HO_2 + OH <-> H_2O + O_2$	2.00E13	0.00	0	
14	$2HO_2 <-> H_2O_2 + O_2$	2.00E12	0.00	0	
15	$2OH + M <-> H_2O_2 + M$	1.60E22	-2.00	0	H_2/2.5/H_2O/16.0
16	$H_2O_2 + H <-> H_2O + OH$	1.00E13	0.00	-1801	
17	$H_2O_2 + H <-> H_2 + HO_2$	1.70E12	0.00	-1902	
18	$H_2O_2 + O <-> OH + HO_2$	2.80E13	0.00	-3221	
19	$H_2O_2 + OH <-> H_2O + HO_2$	7.00E12	0.00	-722.1	

*Reaction rate coefficients are in $K_f = AT^B\exp(E/T)$.

*Related units are in moles, centimeters, seconds, kelvins, and joules.

*Only species with non-unity third body collision efficiency are specified.

Table 2.3 Hydrogen-air chemical kinetic model by Kim, Yetter, and Dryer [49] and Yetter et.al [64].

#	Reaction	A	B	E	Third Body
1	$H + O_2 <-> O + OH$	1.91E14	0.00	-8273	
2	$O + H_2 <-> H + OH$	5.01E04	2.67	-3165	
3	$OH + H_2 <-> H + H_2O$	6.38E06	1.51	-1726	
4	$O + H_2O <-> 2OH$	2.10E08	2.02	-6743	
5	$H_2 + M <-> 2H + M$	4.57E19	-1.40	-52530	H_2/2.5/H_2O/12.0
6	$2O + M <-> O_2 + M$	6.17E15	-0.50	0	H_2/2.5/H_2O/12.0
7	$O + H + M <-> OH + M$	6.10E16	-1.00	0	H_2/2.5/H_2O/12.0
8	$H + OH + M <-> H_2O + M$	2.19E22	-2.00	0	H_2/2.5/H_2O/12.0
9	$H + O_2 + M <-> HO_2 + M$	6.70E19	-1.42	0	H_2/2.5/H_2O/12.0
10	$HO_2 + H <-> H_2 + O_2$	6.61E13	0.00	-1072	
11	$HO_2 + H <-> 2OH$	1.66E14	0.00	-438	
12	$HO_2 + O <-> OH + O_2$	1.74E13	0.00	201	
13	$HO_2 + OH <-> H_2O + O_2$	1.45E16	-1.00	0	
14	$2HO_2 <-> H_2O_2 + O_2$	3.02E12	0.00	820	
15	$H_2O_2 + M <-> 2OH + M$	1.20E17	0.00	-22900	H_2/2.5/H_2O/12.0
16	$H_2O_2 + H <-> H_2O + OH$	1.00E13	0.00	-1807	
17	$H_2O_2 + H <-> H_2 + HO_2$	4.79E13	0.00	-4001	
18	$H_2O_2 + O <-> OH + HO_2$	9.55E06	2.00	-1998	
19	$H_2O_2 + OH <-> H_2O + HO_2$	7.08E12	0.00	-4811	

*Reaction rate coefficients are in $K_f = AT^B\exp(E/T)$.

*Related units are in moles, centimeters, seconds, kelvins, and joules.

*Only species with non-unity third body collision efficiency are specified.

CHAPTER III

METHOD OF SOLUTION AND NUMERICAL DOMAIN

Typical numerical issues related to solving the governing equations for low speed, compressible, and chemically reacting problems are robustness, stability, convergence, CPU speed, and memory. These issues are directly related to the availability of numerical algorithms and their solvers, in conjunction with the accessibility of computer resources. During the past two decades, significant improvements have been made in those areas through the development of better numerical algorithms and the CFD solvers along with the improvements in computer hardware technology. The trend has evolved from explicit, decoupled schemes to strongly implicit and fully coupled schemes which are characterized by better robustness, stability, and convergence, at least of steady state calculations. Yet, the implicit scheme results in slow CPU time per iteration and requires a large computer memory. Recently, a technique has been proposed as a compromise between the hardware and numerical issues [51, 60]. The technique retains the overall structure of implicitly, thus the chemical and convective processes proceed at approximately the same numerical rate. Yet, the set of governing equations is partitioned into two segments, utilizing a small hardware memory. Accordingly, with this approach, the computational calculations can be performed within the qualitative limit of both numerical and hardware aspects.

The detailed mathematical formulations and numerical technique associated with the governing equations (along with numerical model and boundary conditions) are discussed in this chapter. The theoretical background of numerical discretization is given in Sec 3.1 Then, the mathematical formulations and numerical technique are presented in Sec. 3.2. Descriptions of the

numerical model and boundary conditions are addressed in Sec. 3.3. Finally, the ignition procedures associated with the opposed jet configuration are discussed in Sec. 3.4.

3.1 Theoretical Background

One of the advantages associated with the implicit scheme is that it imposes no formal time step restriction, at least in the linear stability sense. In practice, however, there is an effective time step limitation, but it is much less restrictive than with the explicit schemes, due to nonlinear effects and the accuracy requirements of a problem [61].

For compressible chemically reacting Navier-Stokes and species continuity equations, the construction of implicit schemes based on approximate factorization leads to the solution of M by M block tridiagonal systems of equations associated with each gridline, where M represents the total number of equations in consideration. Due to the sparseness of spatial matrices with diagonal coefficient dominance, the block tridiagonal systems of equations are then conveniently and directly solved with the block Thomas algorithm, where the operation count is in the order of NM^3 for the N blocks of equations. Clearly, this is preferred over the other direct method of Gauss elimination, where the full inversion and solution of sparse matrices are processed with the operational count in the order of $(NM)^3$. Yet, the operational count of a problem could be improved if the full block diagonal system is split into M scalar tridiagonal systems. Consequently, by reducing the size of the matrix, the computational time for inversion and solution of the matrix would be greatly reduced, where the total operation count would be in the order of NM. Therefore, there is an incentive to construct implicit algorithms with the decoupled equations, although, the full decoupling may cause incoherency in the physics of problems resulting in high residual errors. In essence, as the governing equations are partitioned such that the aerodynamic set of equations are

separated from the combustion, the computational time for solving two smaller block tridiagonal matrices would be much reduced without loosing the integrity of physics of the problem and high residual errors.

Even with an equation partitioning, the implementation of the block Thomas algorithm to solve block tridiagonal systems is rather computationally costly (direct method). Instead, the iterative method of Gauss Seidel is being implemented for the solution to improve the computational time. The method is chosen, because it is simplistic in technique and is known to be an efficient and useful tool for solving large systems of equations. In addition, the convergence of solution is guaranteed due to a diagonal dominance of matrix coefficients. Unlike Jacobi iteration, where the updated solutions are calculated based on old solutions, the current method utilizes both old and partially updated solution to advance in time. Therefore, the Gauss Seidel iteration ensures a faster convergence for a steady state solution. Alternately, the convergence rate could be further improved if the method of Gauss Seidel Successive Over Relaxation (GS-SOR) is implemented. However, the method requires a predetermined over-relaxation parameter prior to the solution, which is dependent on the grid size, boundary condition, and specific problem, hindering the successful determination of an optimal parameter. For these reasons, the GS-SOR is not considered here.

Similar to the direct method, solving a large matrix utilizing an iterative method is computationally costly. The split of a large matrix into multiple small matrices, in couple with an iterative method, would improve the computational efficiency. Hence, the division of a large matrix into two small (in terms of number of nonzero coefficients) matrices is proposed here, in conjunction of the approximated Lower-Upper (LU) factorization technique. The LU technique factorizes already approximately factorized equations (block diagonal form) into lower and upper diagonal

forms by constructing implicit spatial operators from one sided difference formulae. Then, the lower matrix is solved to obtain the pseudo intermediate flux by a forward substitution (from left hand boundary to right) using the Gauss Seidel method. Similarly, the upper matrix is solved with the pseudo intermediate flux by a backward substitution (from right hand boundary to left), completing one iteration. For the steady state, the iteration process continues until the global convergence criteria are satisfied.

3.2 Method of Solution

Based on the above considerations, the time dependent Navier-Stokes and species transport equations for a chemically reacting gas are solved implicitly with the Lower-Upper Symmetric Gauss-Seidel (LU-SGS) scheme. The chemistry source term is treated implicitly to alleviate the stiffness associated with fast chemical reactions. The system of equations is discretized with backward differencing for the physical time, an Euler implicit differencing for the pseudo time, and central differencing for the space, in conjunction with the dual time marching technique. This marching technique, namely in pseudo and physical times, allows for flexibility in selection of the different time step sizes in the two time spaces. The physical time step size is determined by the characteristic evolution of an unsteady flow under consideration. The pseudo time step size is determined based on the numerical stability of an algorithm, and can be adjusted to give an optimum convergence rate for the pseudo-time marching. At each physical time step, sub-iterations are performed in the pseudo time until a prescribed convergence criterion is satisfied. In the steady state, a physical time term is effectively eliminated by giving a huge time step, and the solution marches in the pseudo time until it converges.

The governing equations are decoupled into two sets; flow and species sets. Each set is

solved in a coupled manner, and a subsequent sweep through the sets in each pseudo time step constitutes one iteration. The decoupled set of governing equations is

$$\Gamma^s \frac{\partial}{\partial \tau}\hat{Q}^s + \frac{\partial}{\partial t}\tilde{Q}^s + \frac{\partial}{\partial \xi}(\tilde{E}^s - \tilde{E}_v^s) + \frac{\partial}{\partial \eta}(\tilde{F}^s - \tilde{F}_v^s) + \frac{\partial}{\partial \zeta}(\tilde{G}^s - \tilde{G}_v^s) = \tilde{H}^s + \tilde{D}^s{}_c \quad (3.1)$$

where s=1,2 represent the flow and species sets respectively. The primitive vector $\hat{Q}$ and the byproducts of a partially decoupled source term $\tilde{D}_c$ are defined as

$$\hat{Q}^1 = \left[\frac{1}{J}(P_g, u, v, w, h)\right]^T \quad (3.2a)$$

$$\hat{Q}^2 = \left[\frac{1}{J}(Y_1, \ldots, Y_{N-1})\right]^T \quad (3.2b)$$

$$\tilde{D}_c^1 = [0, 0, 0, 0, 0]^T \quad (3.2c)$$

$$\tilde{D}_c^2 = \left[\frac{1}{\beta}\frac{\partial}{\partial \tau}\left(\frac{P_g}{J}\right)[Y_1, \ldots, Y_{N-1}]\right]^T \quad (3.2d)$$

The decoupled time preconditioning terms are

$$\Gamma^1 = \begin{bmatrix} 1/\beta & 0 & 0 & 0 & 0 \\ u/\beta & \rho & 0 & 0 & 0 \\ v/\beta & 0 & \rho & 0 & 0 \\ w/\beta & 0 & 0 & \rho & 0 \\ h/\beta - 1 & \rho u & \rho v & \rho w & \rho \end{bmatrix} \quad (3.3a)$$

$$\Gamma^2 = \begin{bmatrix} \rho & \dots & 0 \\ \dots & \dots & \dots \\ \dots & \rho & \dots \\ \dots & \dots & \dots \\ 0 & \dots & \rho \end{bmatrix} \tag{3.3b}$$

With three level backward differencing for the physical time, and an Euler implicit differencing for pseudo time, the equations for the (p+1)th iteration in the pseudo time at the (n+1)th level in physical time can be represented as

$$\Gamma^s \frac{\hat{Q}^{sp+1} - \hat{Q}^{sp}}{\Delta\tau} + \frac{a_1 \tilde{Q}^{sp+1} + a_2 \tilde{Q}^{sn} + a_3 \tilde{Q}^{sn-1}}{\Delta t} + \tag{3.4}$$
$$\frac{\partial(\tilde{E}^s - \tilde{E}_v^s)^{p+1}}{\partial\xi} + \frac{\partial}{\partial\eta}(\tilde{F}^s - \tilde{F}_v^s)^{p+1} + \frac{\partial(\tilde{G}^s - \tilde{G}_v^s)^{p+1}}{\partial\zeta} = \tilde{H}^{sp+1} + \tilde{D}_c^{sp+1}$$

The terms at the (p+1)th time level in the previous expression need to be linearized for the construction of an implicit time marching scheme. Therefore, the inviscid Jacobians used in the linearization are defined as

$$T = \frac{\partial\tilde{Q}}{\partial\hat{Q}}, A = \frac{\partial\tilde{E}}{\partial\hat{Q}}, B = \frac{\partial\tilde{F}}{\partial\hat{Q}}, C = \frac{\partial\tilde{G}}{\partial\hat{Q}} \tag{3.5a}$$

and the differential operator is defined as

$$L_v(\hat{Q}) = \frac{\partial\tilde{E}_v}{\partial\xi} + \frac{\partial\tilde{F}_v}{\partial\eta} + \frac{\partial\tilde{G}_v}{\partial\zeta} \tag{3.5b}$$

The viscous terms can be linearized as

$$L_v(\hat{Q})^{p+1} = L_v(\hat{Q})^p + \left(\frac{\partial}{\partial\xi}R_{\xi\xi}\frac{\partial}{\partial\xi} + \frac{\partial}{\partial\xi}R_{\xi\eta}\frac{\partial}{\partial\eta} + \frac{\partial}{\partial\xi}R_{\xi\zeta}\frac{\partial}{\partial\zeta} + \frac{\partial}{\partial\eta}R_{\eta\xi}\frac{\partial}{\partial\xi} + \right. \tag{3.6}$$
$$\left. \frac{\partial}{\partial\eta}R_{\eta\eta}\frac{\partial}{\partial\eta} + \frac{\partial}{\partial\eta}R_{\eta\zeta}\frac{\partial}{\partial\zeta} + \frac{\partial}{\partial\zeta}R_{\zeta\xi}\frac{\partial}{\partial\xi} + \frac{\partial}{\partial\zeta}R_{\zeta\eta}\frac{\partial}{\partial\eta} + \frac{\partial}{\partial\zeta}R_{\zeta\zeta}\frac{\partial}{\partial\zeta}\right)\Delta\hat{Q}$$

In essence, the system of linearized governing equations in orthogonal curvilinear coordinates is

$$\left\{\Gamma^s + \frac{\Delta\tau}{\Delta t}T^s - \Delta\tau\left[T^s + \left(\frac{\partial A^s}{\partial\xi} - \frac{\partial R^s_{\xi\xi}}{\partial\xi}\frac{\partial}{\partial\xi}\right) + \left(\frac{\partial B^s}{\partial\eta} - \frac{\partial R^s_{\eta\eta}}{\partial\eta}\frac{\partial}{\partial\eta}\right) + \left(\frac{\partial C^s}{\partial\zeta} - \frac{\partial R^s_{\zeta\zeta}}{\partial\zeta}\frac{\partial}{\partial\zeta}\right)\right]\right\}\Delta\hat{Q}^s = -\Delta\tau R^{sp} \tag{3.7}$$

where

$$R^{sp} = \frac{\tilde{Q}^s - \tilde{Q}^s_{n-1}}{\Delta t} + \frac{\partial}{\partial\xi}(\tilde{E}^s - \tilde{E}^s_v) + \frac{\partial}{\partial\eta}(\tilde{F}^s - \tilde{F}^s_v) + \frac{\partial}{\partial\zeta}(\tilde{G}^s - \tilde{G}^s_v) - \tilde{H}^s - \tilde{D}^s{}_c - \tilde{D}^s_4$$

The details of inviscid Jacobians *A*, *B*, and *C*, and the viscid Jacobians $R_{\xi\xi}$, $R_{\eta\eta}$, and $R_{\zeta\zeta}$ in each spatial direction respectively are given by Shuen et al. [60]. By utilizing the time preconditioning with the lower-upper symmetry Gauss Seidel scheme, the left hand side inviscid terms need to be modified. For illustration purposes, the inviscid term in the ξ direction is derived as

$$\frac{\partial A^s}{\partial\xi} = \frac{\partial}{\partial\xi}\left(\Gamma^s\Gamma^{s^{-1}}A^s\right) = \frac{\partial}{\partial\xi}(\Gamma^s\hat{A}^s) \tag{3.8}$$

The term $\hat{A}^s$ is then split into two parts,

$$\hat{A}^s = \frac{1}{2}\left(\hat{A}^s + \alpha|\lambda_A|_{max}I\right) + \frac{1}{2}\left(\hat{A}^s - \alpha|\lambda_A|_{max}I\right) = \hat{A}^{s^+} + \hat{A}^{s^-} \tag{3.9}$$

where $|\lambda_A|_{max}$ is the absolute value of the maximum eigenvalue in the ξ direction at each grid point. The term $\frac{\partial A^s}{\partial\xi}$ is then approximated by the following one sided operator:

$$\frac{\partial A^s}{\partial \xi} = \frac{\partial^-}{\partial \xi}\left(\Gamma^s \hat{A}^{s^+}\right) + \frac{\partial^+}{\partial \xi}\left(\Gamma^s \hat{A}^{s^-}\right) \tag{3.10}$$

where

$$\Gamma^s \hat{A}^{s^\pm} = \frac{1}{2}\Gamma^s\left(\hat{A}^s \pm \alpha|\lambda_A|_{max} I\right) = \frac{1}{2}\left(\hat{A}^s \pm \alpha|\lambda_A|_{max}\Gamma^s\right)$$

The other two terms, $\frac{\partial B^s}{\partial \eta}$ and $\frac{\partial C^s}{\partial \zeta}$ could be derived in a similar manner, but are not illustrated here. Therefore, the discretized governing equations for an lower-upper symmetry Gauss Seidel scheme with time preconditioning can be written as follows:

$$\left\{\Gamma^s + \frac{\Delta\tau}{\Delta t}T^s - \Delta\tau\left[T^s + \left(\frac{\partial A^s}{\partial \xi} - \frac{\partial R^s_{\xi\xi}}{\partial \xi}\frac{\partial}{\partial \xi}\right) + \left(\frac{\partial B^s}{\partial \eta} - \frac{\partial R^s_{\eta\eta}}{\partial \eta}\frac{\partial}{\partial \eta}\right) + \left(\frac{\partial C^s}{\partial \zeta} - \frac{\partial R^s_{\zeta\zeta}}{\partial \zeta}\frac{\partial}{\partial \zeta}\right)\right] + D_2{}^s\right\}\Delta\hat{Q}^s = -\Delta\tau R^{sp} \tag{3.11}$$

The terms, D_2 and D_4 represent the second and fourth order dissipations and are defined as

$$D_2^s = -0.5\alpha\left[\frac{\partial^2}{\partial \xi^2}(|\lambda_a|\Gamma^s) + \frac{\partial^2}{\partial \eta^2}(|\lambda_b|\Gamma^s) + \frac{\partial^2}{\partial \zeta^2}(|\lambda_c|\Gamma^s)\right] \tag{3.12a}$$

$$D_4^s = \sigma\Gamma^s\left[|\lambda_a|\frac{\partial^4 \hat{Q}^s}{\partial \xi^4} + |\lambda_b|\frac{\partial^4 \hat{Q}^s}{\partial \eta^4} + |\lambda_c|\frac{\partial^4 \hat{Q}^s}{\partial \zeta^4}\right] \tag{3.12b}$$

where the parameters α and σ are the dissipation strengths. The terms $\lambda^s_{a,\,b,\,c}$ are the maximum eigenvalues in the ξ, η, and ζ directions, respectively. For the flow set of equations, these are defined as

$$\lambda_a = \frac{1}{2}\left[U_a\left(1+\frac{\hat{\beta}}{c^2}\right) \pm \left(U_a^2\left(1-\frac{\hat{\beta}}{c^2}\right)^2 + 4\hat{\beta}(\xi_x^2+\xi_y^2+\xi_z^2)\right)^{0.5}\right] \tag{3.13a}$$

$$\lambda_b = \frac{1}{2}\left[U_b\left(1+\frac{\hat{\beta}}{c^2}\right) \pm \left(U_b^2\left(1-\frac{\hat{\beta}}{c^2}\right)^2 + 4\hat{\beta}(\eta_x^2+\eta_y^2+\eta_z^2)\right)^{0.5}\right] \tag{3.13b}$$

$$\lambda_c = \frac{1}{2}\left[U_c\left(1+\frac{\hat{\beta}}{c^2}\right) \pm \left(U_c^2\left(1-\frac{\hat{\beta}}{c^2}\right)^2 + 4\hat{\beta}(\zeta_x^2+\zeta_y^2+\zeta_z^2)\right)^{0.5}\right] \tag{3.13c}$$

where the contravariant velocity components U_a, U_b, and U_c are expressed as

$$U_a = \xi_x u + \xi_y v + \xi_z w$$

$$U_b = \eta_x u + \eta_y v + \eta_z w$$

$$U_c = \zeta_x u + \zeta_y v + \zeta_z w$$

and

$$\hat{\beta} = max(\beta, U_{ref}^2)/(relax) \tag{3.14}$$

For the species set of equations, the maximum eigenvalues of the system are simply the contravariant velocity components as defined earlier. Overall, the pseudo time is then calculated by

$$\Delta\tau = CFL/(\lambda_a^2+\lambda_b^2+\lambda_c^2)^{0.5} \tag{3.15}$$

where *CFL* is the user defined value.

Because the governing equations are decoupled into two sets, the extra term found in the species equations is needed to evaluate the conservation of mass. This can be done by rearranging the continuity equation as follows:

$$\frac{1}{\beta}\frac{\partial}{\partial\tau}\left(\frac{P_g}{J}\right) = -\nabla\bullet(\rho\vec{v}) + \sum_p n_p \dot{m}_p \tag{3.16}$$

3.3 Numerical Domain and Boundary Conditions

Discretization of the governing equations is often accompanied with discretized domain. The accuracy of problem solution depends on (and can be greatly improved with) well constructed grids and proper representation of boundary conditions. Therefore, any inadequacy in numerical domain could cause instability and large errors in problem solution.

Figure 3.1 shows the numerical representation of the physical domain, which was described earlier. Only a sector of the physical domain is considered because a symmetry of flows exists along the axial centerline. In this study, the numerical domain is segmented into three blocks defined radially. Nonetheless, no segmentation is given in the axial direction even though a finite tube wall thickness is incorporated as a part of the numerical domain. The first block represents a tube radius height, where the upstream boundary conditions are applied on both ends of the block, reflecting the fuel and oxidizer inflows. At the upstream boundary, all the properties are pre-determined (specified) and remain constant, independent of interior properties. However, the pressure is obtained from the interior points using a second order extrapolation. Along the axis centerline, a singularity boundary condition is applied due to a collapse of many gridlines into one. In the calculation, the solution matrix does not include the points along the singularity where the centerline values are later extrapolated from the interior points. In this study, many fine grid spacings are assigned to the tube wall region radially to account for its physically small thickness. In typical, five equally spaced grid points are used to represent the nonreacting and adiabatic wall, where both pressure and enthalpy gradients are assumed to be zero.

The next block represents the coflow zones where the upstream boundary condition is

applied to both ends of the block. Also, special attention is given to the boundaries connecting the neighboring blocks because the information is exchanged between the blocks. In this connection, three interior points, with equal grid spacings from each neighboring block, are utilized for communication. Therefore, with higher degrees of accuracy, an equal weight in information is passed from one neighboring block to the other. At the juncture of the first and second blocks, a dense and compressed grid clustering is given radially to generate smooth and continuous grid spacing for the domain in large.

The last block represents the end zone, where the downstream boundary condition is applied to the upper end of the block. At the downstream boundary, only exit pressure is required to be specified and it remains constant. The other flow quantities are obtained from the interior points with a second order extrapolation. The block has wall boundary conditions on both sides to channel the hot combusted gases to the exit. The wall is assumed nonreactive, nonslip, and isothermal with zero pressure gradient.

Overall, a periodic boundary condition is applied to all three blocks on both ends of the angular direction. Consequently, the information on one end of the angular plane is adequately exchanged with the other, completing the characteristics of axisymmetric flows. An axially dense but uniform grid is given to represent the separation distance, whereas a coarse but compressed grid is given to the exit to represent tube flows. Radially, a dense but nonuniform grid represents the first two blocks, whereas a coarse grid represents the last block. The details of grid density for each blocks are be discussed in the next chapters.

3.4 Ignition

Ignition is a transient process representing an evolution between nonreactive and reactive

states. Ignition is often achieved with external stimuli that lead the thermochemical process in a rapid transition to self sustained combustion. The ignition process is very complex and involves many intricate physical and chemical parameters. Nonetheless, the process can be generalized in an overview of ignition characteristics. In general, the process requires the zone of a flowfield, prior to ignition, to be sufficient in concentration, and the mixing of fuel and oxidizer to occur at the molecular level. Deficiency in fuel or oxidizer at a molecular level would deprive a series of chemical reactions that allow combustion. In addition, the ignition relies on the temperature to be above a critical limit. Therefore, the rate of heat loss due to conduction, convection, and radiation must be less than the rate of heat production by chemical reactions. Lastly, the ignition process requires sufficient time for heat to be absorbed by reactants, so that enough free radicals are produced by chain reaction branching to overcome radical recombination processes.

In this context, the general ignition procedure of hydrogen-air opposed jet flows is outlined below. Clearly, the opposed jet flows can not generate a self induced flame, due to the low induction temperature and velocities at atmospheric pressure. Therefore, an external ignition source is introduced (through the energy equation) to artificially initiate the diffusion flame. In this process, a large amount of energy is introduced into a spatially localized zone, where the hydrogen and air coexist stoichimetrically, preferably on the oxidizer side near the stagnated region. The minimum strength of ignition is rather difficult to quantify; it depends on many physical and chemical parameters. But the ignition strength should be adequate enough to instigate the combustion in a short period of time. Any prolonged addition of weak energy or abrupt introduction of excessive energy into a spatially localized zone unacceptably changes the characteristics of the stoichiometric mixture, causing difficulty in retaining a stable flame (or no flame at all).

As ignition energy is added to the spatially localized zone, the temperature is increased and

maintained above the ignition limit until the flame becomes self-sustained. During the ignition process, the species, HO_2 and H_2O_2 are recognized as important intermediates which "bridge" the reactants (O_2 and H_2) and lead to the production of more reactive free radical species such as OH, O, and H. Therefore, in this study, sufficient concentrations of these intermediate species promote ignition. The ignition temperature limit appears to increase monotonically with increasing strain rate [62]. This indicates that high strain rate decreases the leakage of free radicals out of the reactive zone, which affects the ignition process by reducing the radial populations within a zone via recombination processes. In other words, the ignition process is affected by the higher input velocity, because it reduces the local flow residence time. Therefore, the ignition process is preferred at low speeds. Once a self sustained flame is established, the external source is terminated.

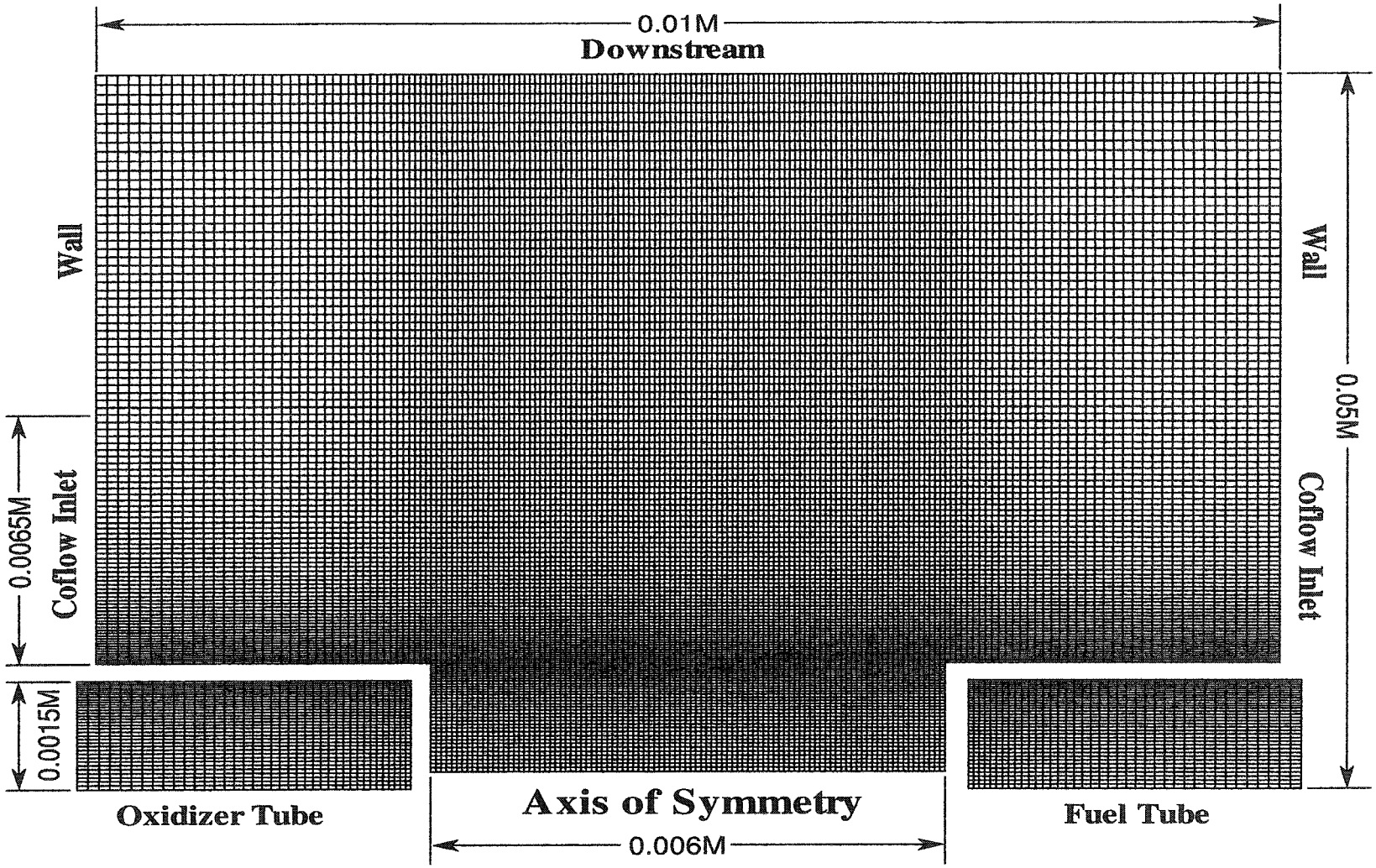

Fig. 3.1 Schematic of numerical domain.

CHAPTER IV

NONREACTING OPPOSED JET FLOWS

The opposed jet configuration has been the subject of combustion research interest for many years. Due to the strong theoretical basis for this configuration for laminar flames, and the relative ease in conducting experiments, studies of opposed jet flows have also been extended to premixed flames, unsteady flames, and even turbulent combustion. Of prime interest here are the effects of the laminar counterflow diffusion flame responding to the aerodynamics of flowfield. In particular, counterflow diffusion flames responding to different cold-inflow velocity profiles display distinctive flame structure and extinction characteristics. Therefore, the details of flow impingement dynamics at various inflow conditions, prior to the combustion, become an important precursor to understanding later flows with combustion.

Through the opposed jet experimental approach [14-21], many attempts have been made to investigate key phenomena. However, because of the small dimensions required for achieving extinction while maintaining laminar flow, in particular with pure hydrogen fuel, detailed and quantitative measurements of two dimensional jet impingement characteristics are quite difficult and not yet available.

Many experimental studies have been limited to the quantitative description of the flowfield along the axis centerline, or to global descriptions of the one dimensional flow characteristics. For example, (one-half) the maximum airside axial strain rate, and the radial strain rate experienced by a flame are approximated globally by using the average input velocity, based on mass flow rate divided by tube diameter [17]. Even various one dimensional computational

approachs [11, 12, and 29-42] only characterize the flow along the centerline axis, and necessarily ignore the detailed behavior of the entire jet impingement flowfield.

Few numerical attempts have been made to characterize the opposed jet flows two dimensionally [43-47]. Mostly, their works are confined to coupled 2-D flow-flame characteristics validating the measurement data - no 2-D flow characteristics are independently investigated from the flame.

This cold flow study starts with the general configuration of nonreacting impinging jets in an initially stagnant ambient fluid volume with both parabolic and plug inflow boundaries at a distance of approximately two jet diameters. Then, the study focuses on the fundamental characteristics associated with jet to jet impingement dynamics. In essence, the knowledge gained in this study will be used as diagnostics for various measurement techniques and, more importantly, as building blocks in characterizing the opposed jet diffusion flame in proceeding chapters.

This chapter is organized in the following manner. First, the general characteristics of opposed jet flows with both plug and parabolic inflow boundaries are discussed in Sec. 4.1. Then, the axial dimensional effects of domain are addressed in Sec. 4.2, in conjunction with effects of finite tube length and thickness on overall flowfield. Finally, the effects of different radial domain sizes on the impingement response characteristics are presented in Sec. 4.3.

4.1 General Characteristics of Cold Flows

In this study, the opposed jet flows are first simulated with pure nitrogen gas at injection velocities ranging from 0.5 to 4.5 meters per second. The flows are assumed to be isothermal, and no coflow gas is considered here. The input-boundary of velocity profiles are assumed both parabolic and plug flow types. Also, adiabatic and slip boundary conditions are applied to the inner

tube wall reducing the degradation of inflow velocity profiles. Isothermal and nonslip conditions are assigned to the domain walls in the farfield region to minimize adverse downstream disturbances to the impingement region.

Typically, the flow impingement results in a large flow gradient in the stagnation region, which must be adequately resolved. Thus a grid independency analysis is first performed using a plug-flow input at a velocity of 4.5 meters per second as shown in Fig. 4.1. The tube diameter is 8 millimeters, and the tube separation distance is 24 millimeters (L/D=3). The centerline nondimensional axial velocity, V/V_i, where V_i is the inflow axial velocity, is plotted against a portion of the axial distance that extends to half of the separation distance. As the grid density increases, the velocity profiles converge to the point where no significant change in the axial velocity is observed. Accordingly, grid independency in this cold flow solution is achieved at a grid density of four spaces per millimeter, for representing the axial jet separation distance. Radially, this same axial grid density is applied in the impingement region even though relatively less (gradient) variation in flow characteristics is observed. Also, dense grid clustering is assigned in the vicinity of the tube wall to account for its finite thickness. A continuous, but lesser, grid density is used to represent the outer regions as the jets dissipate into the surrounding flowfield. The solution convergence is achieved as the solution marches in pseudo-time until the L2 norm of the residual errors is reduced to four orders of magnitude smaller than the initial startup.

The general characteristics of the opposed jet flows at both plug and parabolic inflow conditions are presented in Fig. 4.2. Note the entire flowfield is divided into three distinct regions; these are internal tube, impingement, and free radial jet regions. The velocity vector plots illustrate that the impingement flows are characterized by two distinct features, namely, flow compression and divergence. Compression occurs due to the counterflow stagnation. The flow divergence

is seen as the axial momentum is redirected radially due to the presence of the stagnation region. Recent experimental work [63] reported the observation of these characteristics, where the impingement dynamics of nonreacting flows were visualized using Particle Image Velocimetry (PIV), with silica particles seeded upstream in the oxidizer flow (Fig. 4.3). The double exposure image shows the jet impingement in which the flow undergoes an axial stagnation and radial divergence. Both numerical and experimental results display nearly identical characteristics, qualitatively.

In the impingement region (width=separation distance and height=tube radius from the axial centerline), the exit flows undergo a transition, and the flow direction shifts from axially to radially. These transitions are clearly seen in Figs. 4.4 and 4.5 where the axial velocity gradient increases to a maximum along the centerline, although the axial velocity decreases along the axial centerline at zero radial distance. The radial velocity gains in magnitude as flow approaches the stagnation surface. The radial flow experiences a highest radial expansion rate (per second) at the axial stagnation point (maximum slopes at zero radial distance), causing a highest flow pressure there (Fig. 4.6). Consequently, the downstream velocity profiles ahead of the tube exits in Figs. 4.4 and 4.5 are distorted and different from the tube input profiles in Fig. 4.7.

The input profile distortion is strongly dependent on fluid properties, separation distance, inflow speed, and profile type. For instance, the parabolic inflows have a larger radial variation of normalized axial velocity component, V/V_i, near the axial centerline and the tube wall, than the near unity values of the middle core (in the radial direction) region, regardless of mean inflow velocity, V_i. However, the plug inflows have a radially uniform axial velocity component in Fig. 4.7 that varies considerably with mean inflow velocity, V_i.

Thus when the input velocity increases from the mean velocity of 0.5 to 2.5 meters per second, the jet impingement results in a greater flow divergence and compression at the stagnation point (Fig. 4.7). As a result, the higher plug-flow input reduces the magnitude of normalized axial velocity in the impingement region much more than the low speed input. The parabolic inflows have greater flow compression than the plug inflows, showing no significant changes in normalized axial velocity profile for the present average input velocity range. For both inflows, recirculations appear on both sides of the external tube region dispersing the flow into the downstream although no recirculation is observed in the impingement region.

When the impingement characteristics of both parabolic and plug inflows are compared at an identical mean input velocity of 0.5 meters per second, the centerline axial velocity of the parabolic inflow is twice the magnitude of the plug inflow. This translates to a global applied stress rate [17] -- average input velocity divided by exit diameter -- for both inflows to be 167 per second. However, the maximum radial velocity gradient (strain rate) at the stagnation plane is 2.53 times greater for parabolic inflows than for plug inflows (from Figs. 4.4 and 4.5).

For the plug inflows, the maximum axial and radial strain rates about the stagnation point are 384 and 193 per seconds, respectively (from Fig. 4.8). This indicates that the axial strain rate about the stagnation point is twice the radial strain rate, in agreement with 1-D theory [28, 29]. The ratio of radial strain rate to global applied stress rate is slightly more than unity (1.15).

For the parabolic inflows, the maximum axial and radial strain rates about the stagnation point are 972 and 488 per seconds. This implies that the axial strain rate is 5.82 times larger than the global applied stress rate, but the radial strain rate is still half of the axial rate.

Thus overall, both inflows generate a twice larger axial strain rate than the radial strain

rate. Also, the parabolic inflows generate 2.53 times larger axial and radial strain rates at the centerline stagnation point than the plug inflows.

Therefore, in the event of combustion, a greater radial stretching of a flame would be expected for the parabolic inflows, which would lead to an early extinction of the flame. However, as the radial flow propagates away from the centerline for parabolic inflows, its strength decreases rapidly. As a result, the parabolic inflows facilitate the formation of a post extinction ring-shaped flame easier than with the plug inflows.

The last simulation is performed with a nitrogen fuel jet, diluted 10% in mass by hydrogen, impinging against pure air (3 meters per second). The input flows are plug type, and the fuel input velocity is approximately balanced using the one dimensional momentum equation. Figure 4.9 represents the velocity vector and density isocontour of the opposed jet flows. The density isocontours reveal that the flow undergoes a strong preferential diffusion process, where the hydrogen gas diffuses deep into the oxidizer and the surrounding inert gas. This asymmetry is mainly due to the unique properties of hydrogen which exhibit higher diffusivity, lower density, and higher convective velocity (due to a required higher input velocity) than the oxidizer. As a consequence, after ignition, the flame is located on the oxidation side, resulting in a different locus of flow stagnation and flame front.

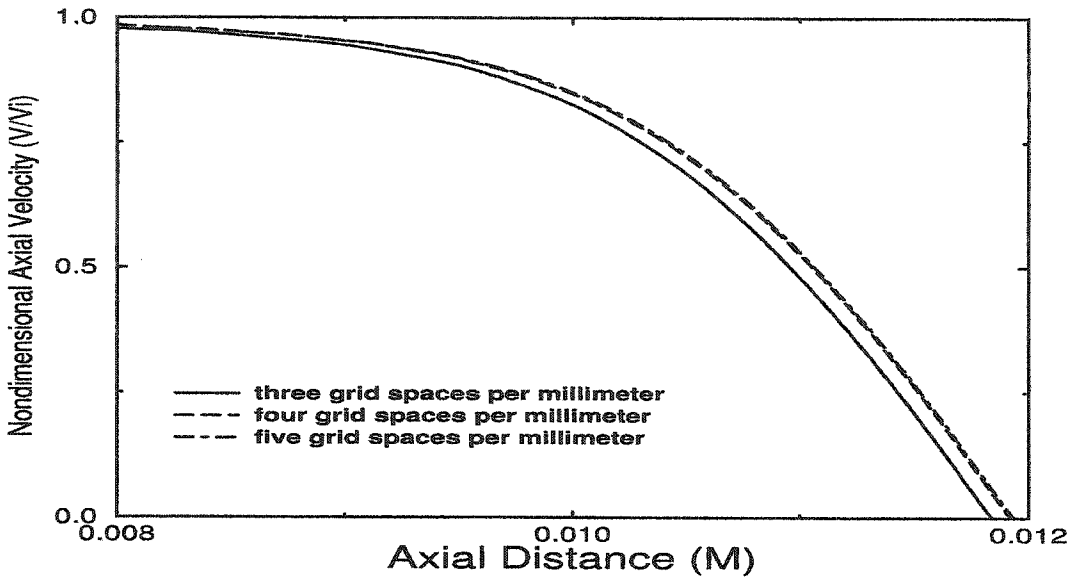

Fig. 4.1 Axial centerline distribution of nondimensional axial velocity at different grid densities at plug inflows of 4.5 meters per second (tube diameter and separation distance are 0.008 and 0.024 meters, respectively).

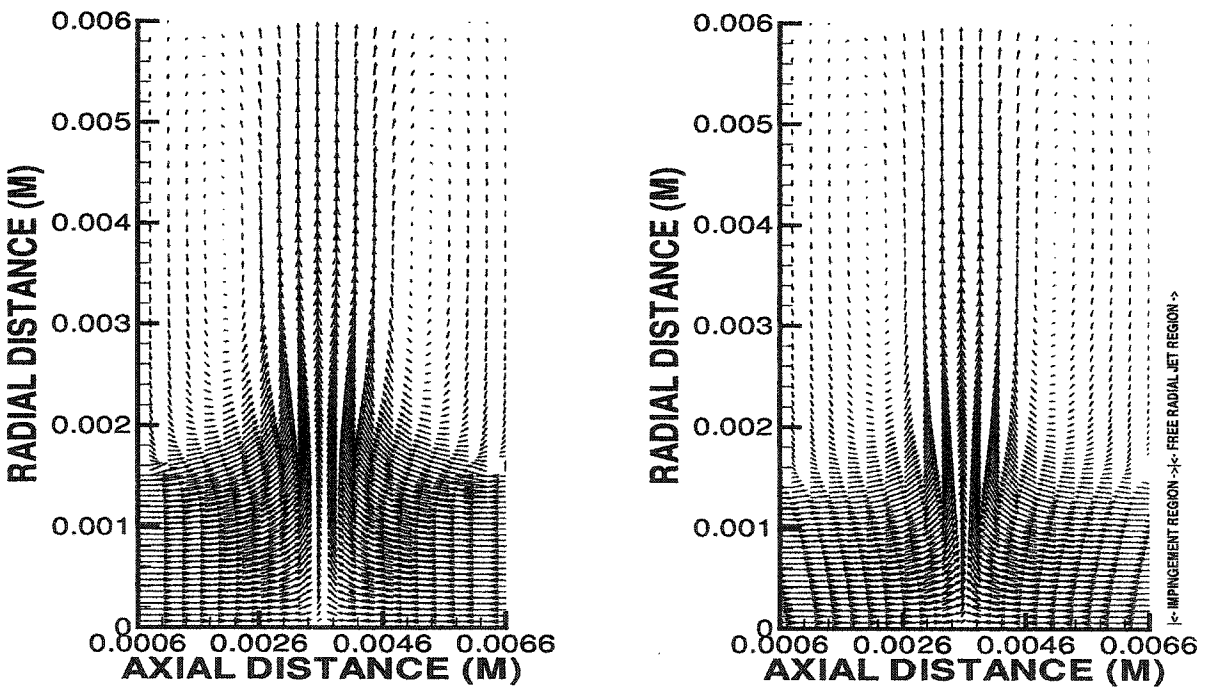

Fig. 4.2 Velocity vector of nonreacting opposed jet flows at mean inflow velocity of 0.5 meters per second.

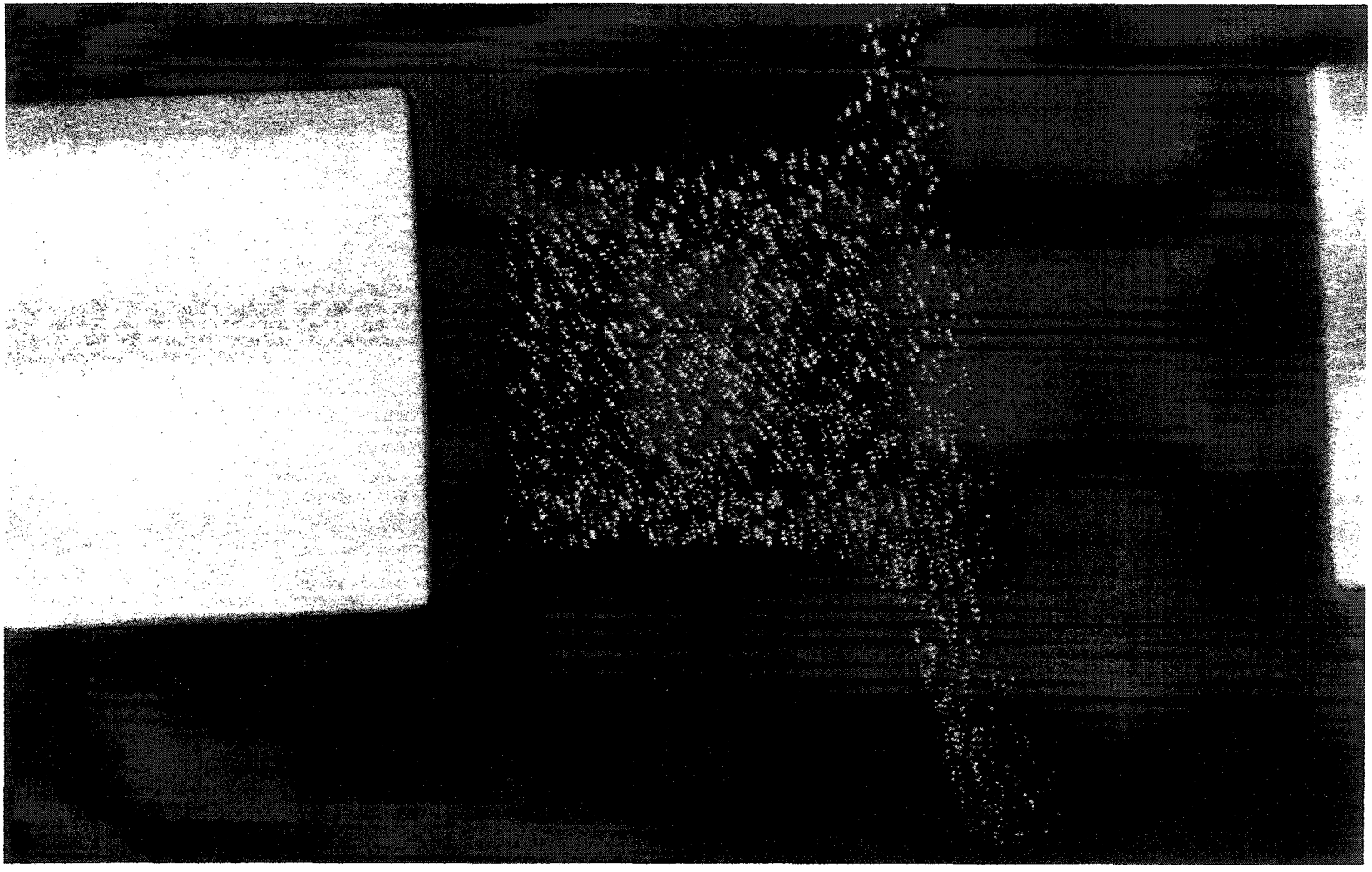

Fig. 4.3 Nonreacting opposed jet laminar flows using PIV in conjunction with silica particle seeding [63].

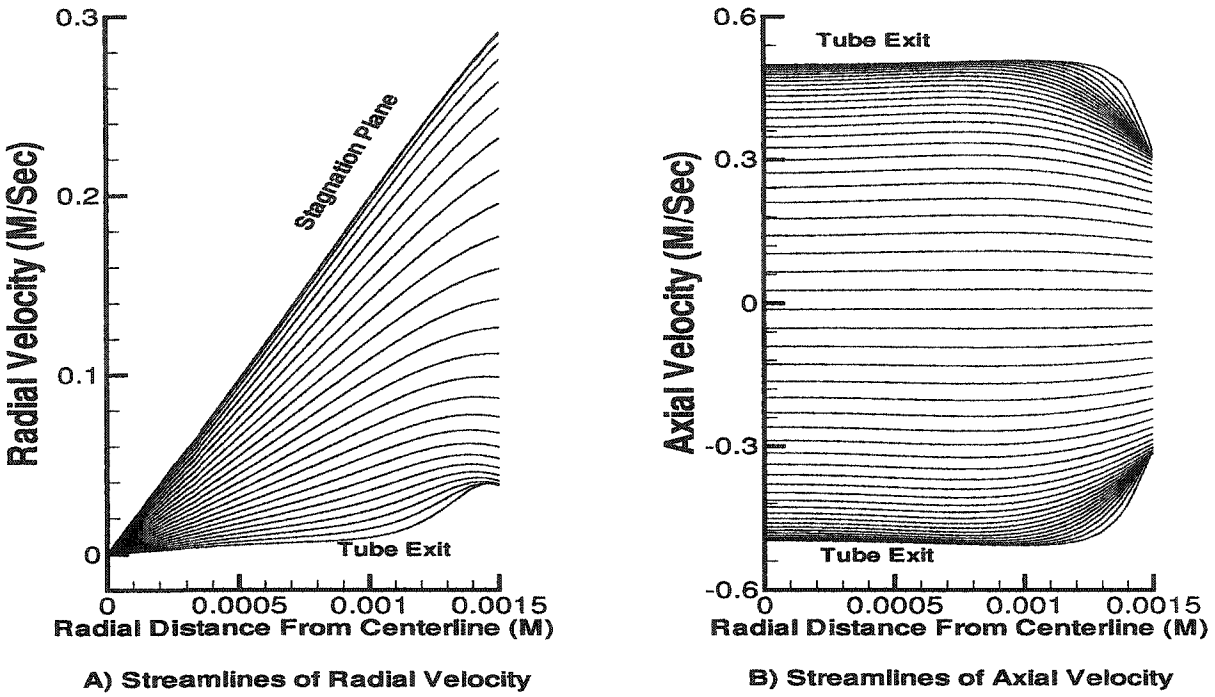

Fig. 4.4 Streamlines of radial and axial velocities in impingement region for plug inflows of 0.5 meters per second.

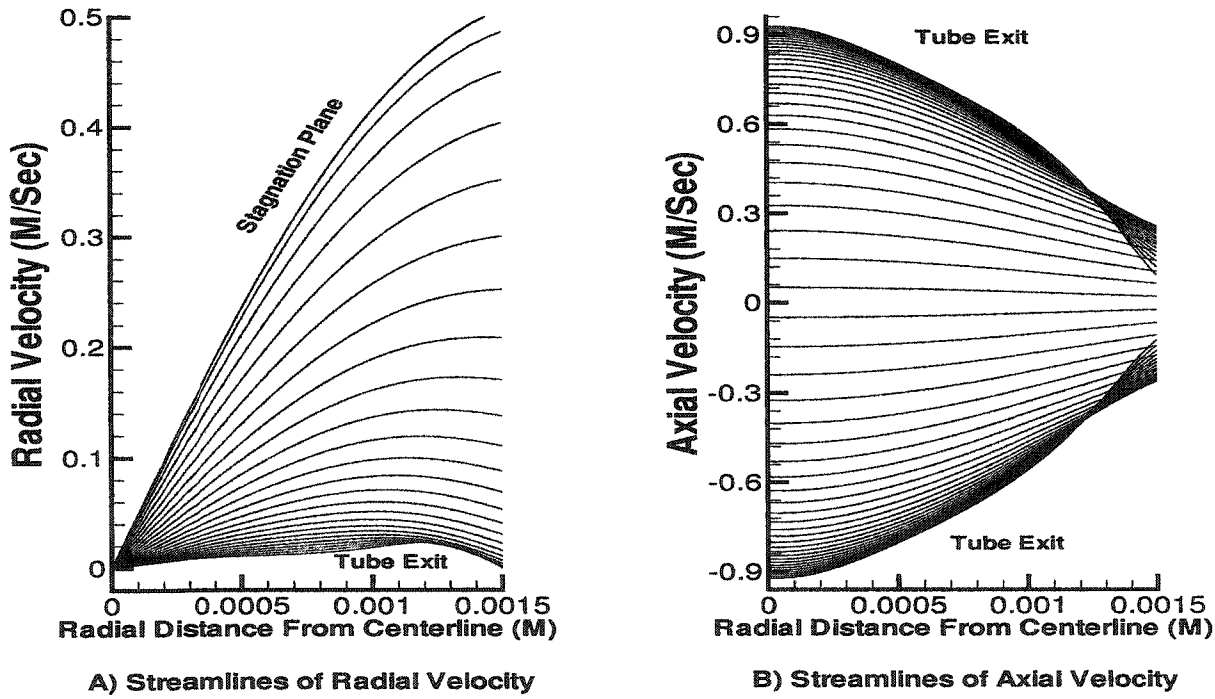

Fig. 4.5 Streamlines of radial and axial velocities in impingement region for parabolic inflows of mean velocity of 0.5 meters per second.

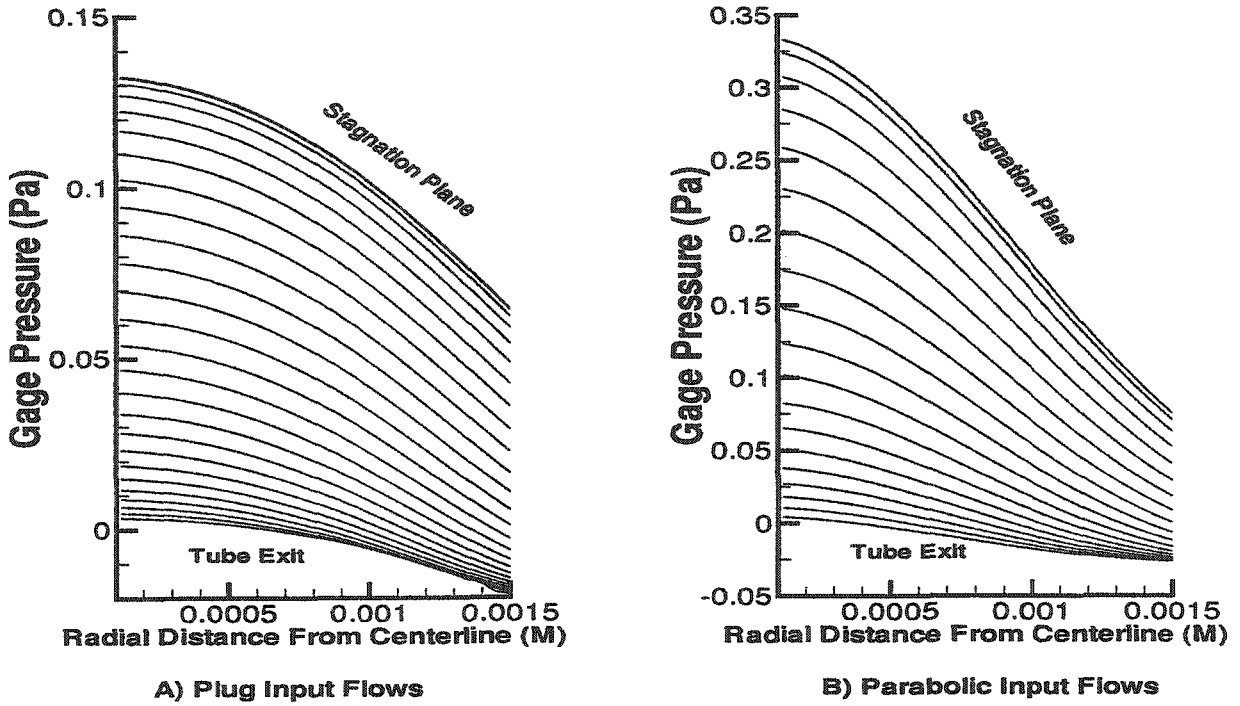

Fig. 4.6 Streamlines of gage pressure in impingement region for plug and parabolic inflows at mean velocity of 0.5 meters per second.

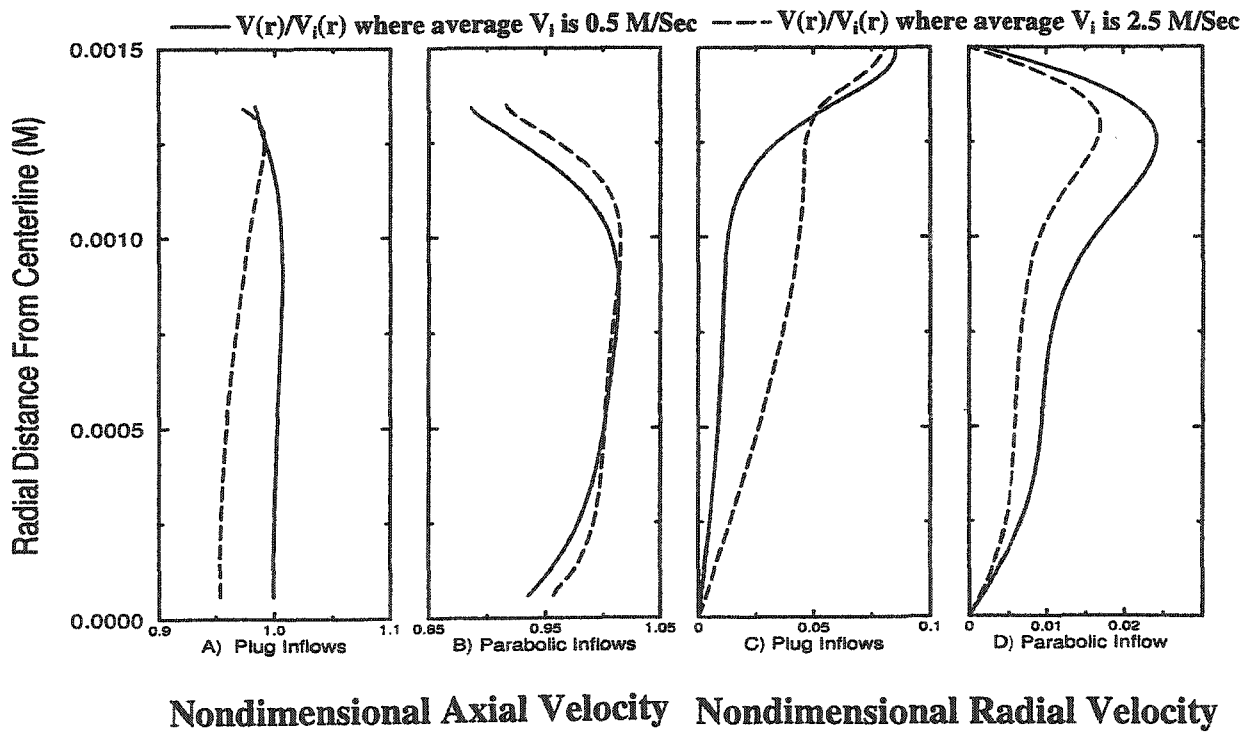

Fig. 4.7 Radial distribution of nondimensional axial and radial velocities at tube exit for mean inflow velocities of 0.5 and 2.5 meters per second.

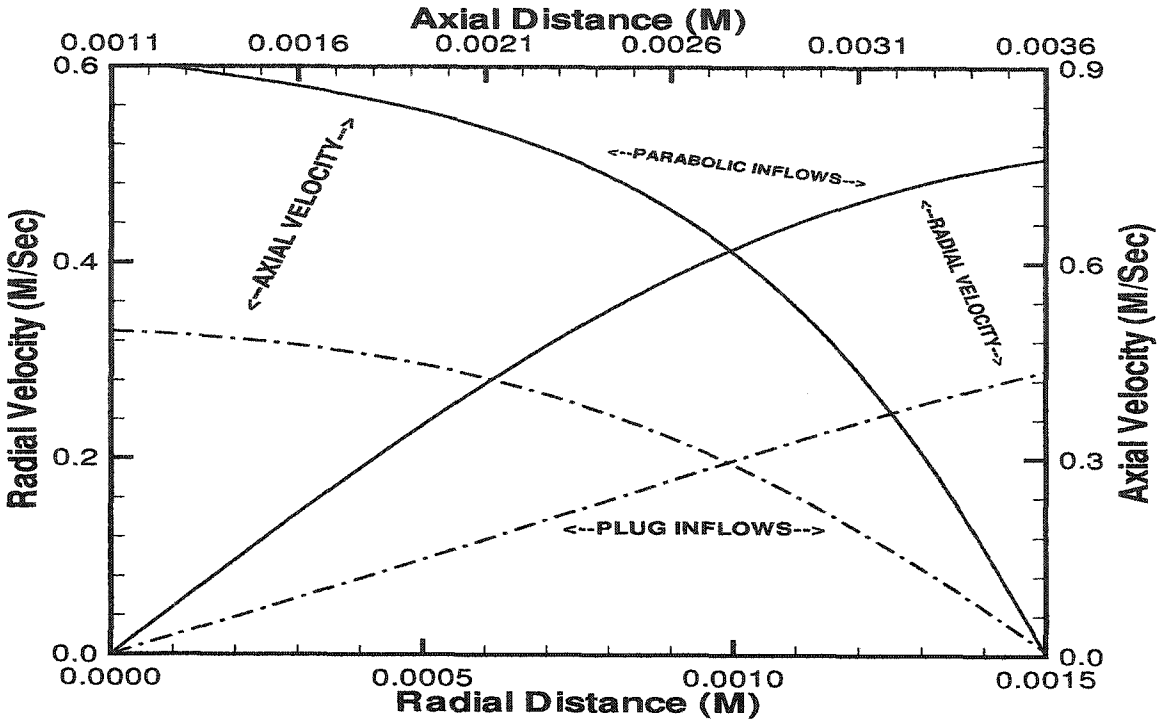

Fig. 4.8 Distributions of axial velocity at axial centerline, and radial velocity at stagnation plane; for both plug and parabolic inflow boundaries at average input velocity of 0.5 meters per second.

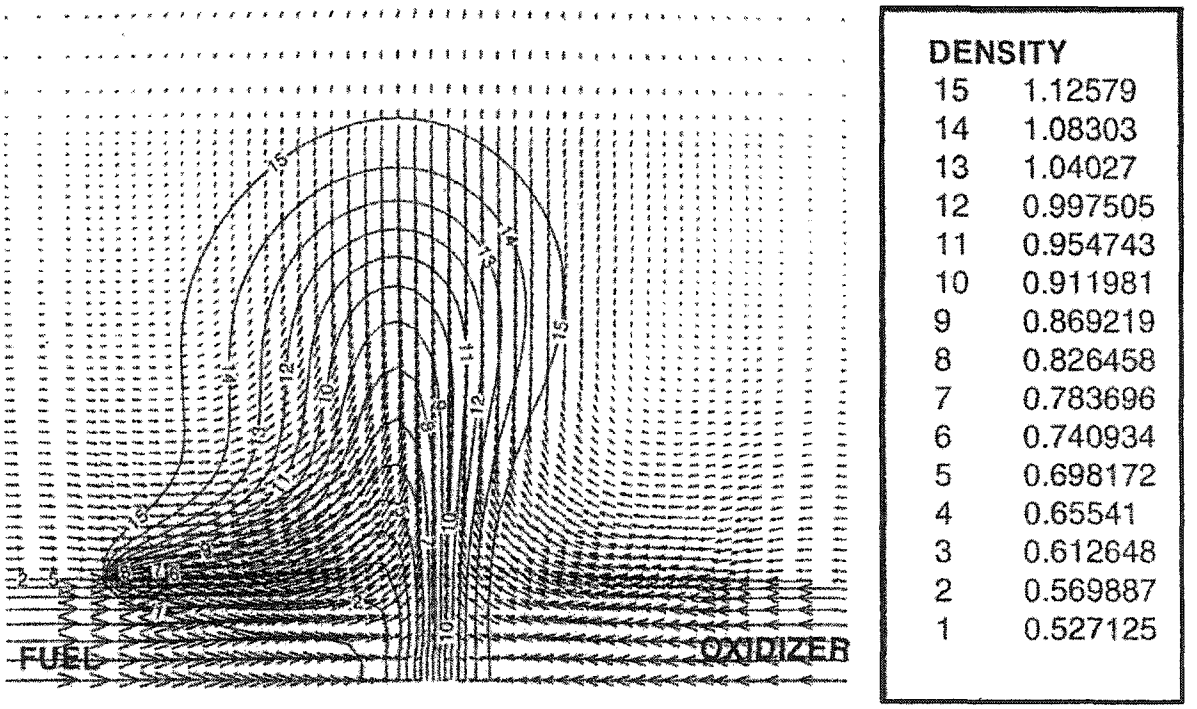

Fig. 4.9 Velocity vector and density isocontour fuel consisting of nitrogen, diluted 10% in mass with hydrogen, versus air opposed jets with 3 meters per second plug inflow boundaries.

4.2 Axial Effects of Domain

Previously, Frouzakis et al. [45] simulated the opposed jet flame using a two dimensional numerical technique. They modelled a domain where the tube (nozzle) separation distance (approximately twice the tube diameter) equals the axial length of the domain. The initial counter-flow jets were prescribed as a part of the domain boundary condition. They were able to capture the entire fuel-lean diffusion flame at a low strain rate condition. However, for the fuel-rich diffusion flame (for example, 100% H_2-Air), the typical maximum axial thickness of a flame in the downstream region was 8 to 10 times larger than the tube radius. The domain in [45] is not adequate for fuel rich low strain rate diffusion flame cases. This requires an extended axial domain, otherwise, the dimensional restriction could improperly constrict a flame axially that could adversely affect the overall flame structure and extinction characteristics. The separation distance could be increased to accommodate this axial flame expansion. However, larger separation distance causes difficulty in deducing the strain rate imposed by the aerodynamics of flows.

In this study, a numerical domain is used that can capture the entirety of a fuel-rich flame without expanding the separation distance. The domain (Fig. 2.1) includes tubes that are closely placed, defining a separation distance equal to twice the tube diameter. The jet flows are initiated from the inner tubes that protrude one tube diameter from the outer (radial) inert coflow region. In this configuration, the downstream axial domain is large enough to capture the entirety of a free floating flame (Fig. 2.2) without nearly wall quenching and dimensional limitation. The present domain (which is more realistic to the opposed jet experimental setup in [17]) differs from Frouzakis et al.'s configuration by including a 0.6 millimeter protruding tube as a part of domain.

Therefore, initial studies are conducted next to investigate the differences in impingement characteristics with channeled (protruding tubes) and unchanneled flows. In addition, a set of simulations is performed to identify the overall effects of tube wall thickness on the flowfield.

A set of simulations was thus performed to investigate the physical effects of channeled and unchanneled flows on the impingement characteristics. First, the jet flows are simulated with the domain, including a 0.6 millimeters long tube at a separation distance of 6 millimeters. The jet inflows were assumed plug type with a velocity of 0.5 meters per second. For comparison, a second part of the simulation was performed with a domain at the identical conditions except the protruding tubes were not included.

Figures 4.10-4.15 represent the isocontours of velocity components and gage pressures for each specified domain. In the impingement region, the tubes play the obvious role of guiding and directing the inflows toward the stagnation plane. As a result, a higher axial velocity at the tube exit, compressional pressure at the stagnation plane, and radial velocity are seen for the channelled flows. Alternatively, the unchanneled flows diverge and disperse precociously in the radial direction upon exit from the inflow boundary. Their axial magnitudes near the tube exits are slightly smaller than those of the channeled flows. Therefore, in the event of combustion, the channeled jet would give a slightly shorter flow residence time within a flame, in which higher flame stretching would be expected. Later, this could lead to a slightly early extinction of a flame, as the input velocity increases.

Next, the second set of simulations is conducted to investigate the overall effects of tube wall thickness in the flow domain. Three wall thicknesses are considered in this study, namely, three, six, and nine percent of the tube diameter. For a comparison, the centerline axial strain rate distribution at various wall thicknesses is plotted against the axial separation distance (over one-

half the distance due to symmetry), shown in Fig. 4.16a. Also, the radial velocity distribution (at one-half the axial distance between the tube exit and stagnation plane) is plotted against radial distance, shown in Fig. 4.16b. The latter distribution (plot) would represent the axial outer edge (on the oxidizer side) of a flame in the event of combustion. For the thicker walls, slightly higher centerline axial strain rates are seen at the tube exit and stagnation plane. Overall, the axial flow experiences a significant deceleration in magnitude upon exit from the tube, until stagnation. Simultaneously, a larger magnitude of radial velocity is observed with a thicker wall, at any given radial distance. This indicates that the thicker tube wall generates a greater flow disturbance, propagating axially toward the stagnation plane. This disturbance, in turn, channels the exit flows closer to the stagnation plane. As a result, the axial velocity has to decelerate to stagnate in a relatively shorter axial distance, causing a slightly higher axial strain rate. In parallel, a thicker tube wall yields a weaker radial expansion of flows developed relatively close to the stagnation plane. As the wall thickness decreases, the distributions converge to the point where no significant changes in the axial and radial velocity distributions are observed. Therefore, the flows becomes effectively independent of the tube wall thickness (at about six percent).

4.3 Radial Effects of Domain

For subsonic flows, any local disturbance in flow characteristics propagates to the entire domain at acoustic speed, $\frac{dp}{d\rho}$, faster than the typical convective speed. Therefore, any change in the domain will ultimately affect the downstream condition. Conversely, the downstream condition will influence flow in the domain. For this reason, in theory, a computational study is preferred with near-infinite radial domain dimension, where the downstream boundary effect on the overall flow characteristics would be nonexistent. However, due to computational limitations, the

numerical study must be performed with a finite radial domain in which the adverse effects of a downstream boundary are possible. Therefore, in this study, a set of simulations is performed to identify the effects of the radial domain on the impingement dynamics.

The first simulation is performed at the plug inflow velocity of 0.5 meters per second with the radial domain extended from the axial centerline by 30 tube radii. This is compared to a second set of impingement flows, with identical inflow parameters, except its radial extension is 6 tube radii. The comparison indicates that a larger radial extension of the domain does not influence the overall characteristics of the axial velocity; both sets of isocontours show a near identical distribution (Fig. 4.17). However, a noticeable difference in the characteristics of radial velocity is observed beyond 4.5 millimeter (three tube radii), where a reduced radial domain generates an underexpanded isocontour of radial velocity distribution (Fig. 4.18). Contributing from the downstream boundary, where only the exit pressure is assumed atmospheric and constant, the divergence of flows is influenced by the smaller radial domain, where a radial jet is prematurely smeared and dissipated into the surrounding medium.

To further investigate the effects of radial domain, a third simulation is performed, with plug inflows at an air velocity of four meters per second, and a radial dimension of 6 tube radii. In this analysis, 100% H_2 is used as the fuel injected against air consisting of 21% O_2 and 79% N_2. The fuel side velocity is calculated based on the one dimensional approximation of the momentum balance equation. The velocity vector plot shown in Fig. 4.19 indicates that the axial flows are rapidly diverged radially, leaving two vertically-displaced (dual) recirculations in the impingement region. The dual recirculations appear to define a stagnation surface, leaving the impingement characteristics significantly different from that seen in Fig. 4.2 for fuel and air streams, having the same density. It appears that the downstream pressure at the numerical bound-

ary adversely smears onto a compressional region, where the flow compression has been reduced. Overall, the smaller radial dimension influences the impingement dynamics, and these effects become more distinctive with the higher inflow velocities.

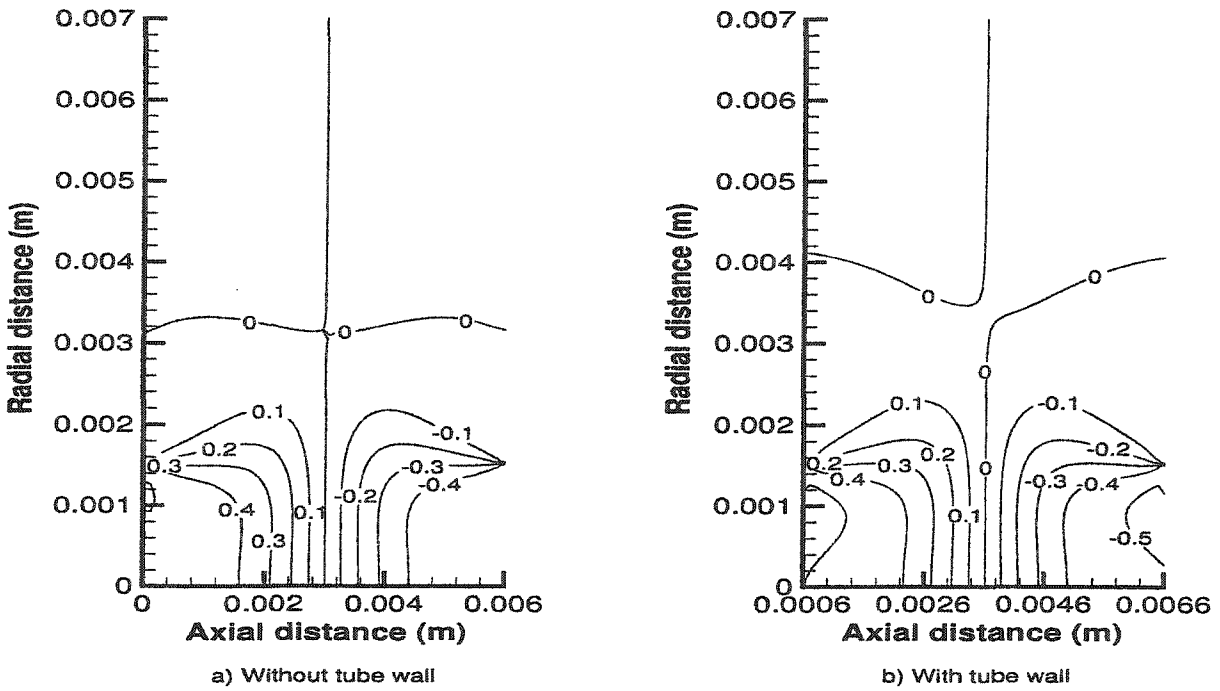

Fig. 4.10 Isocontours of axial velocity with channeled (tube length, 0.0006 meters; radius, 0.0015 meters) and unchanneled (no tube length; initial jet radius 0.0015 meters) flows at plug inflows of 0.5 meters per second.

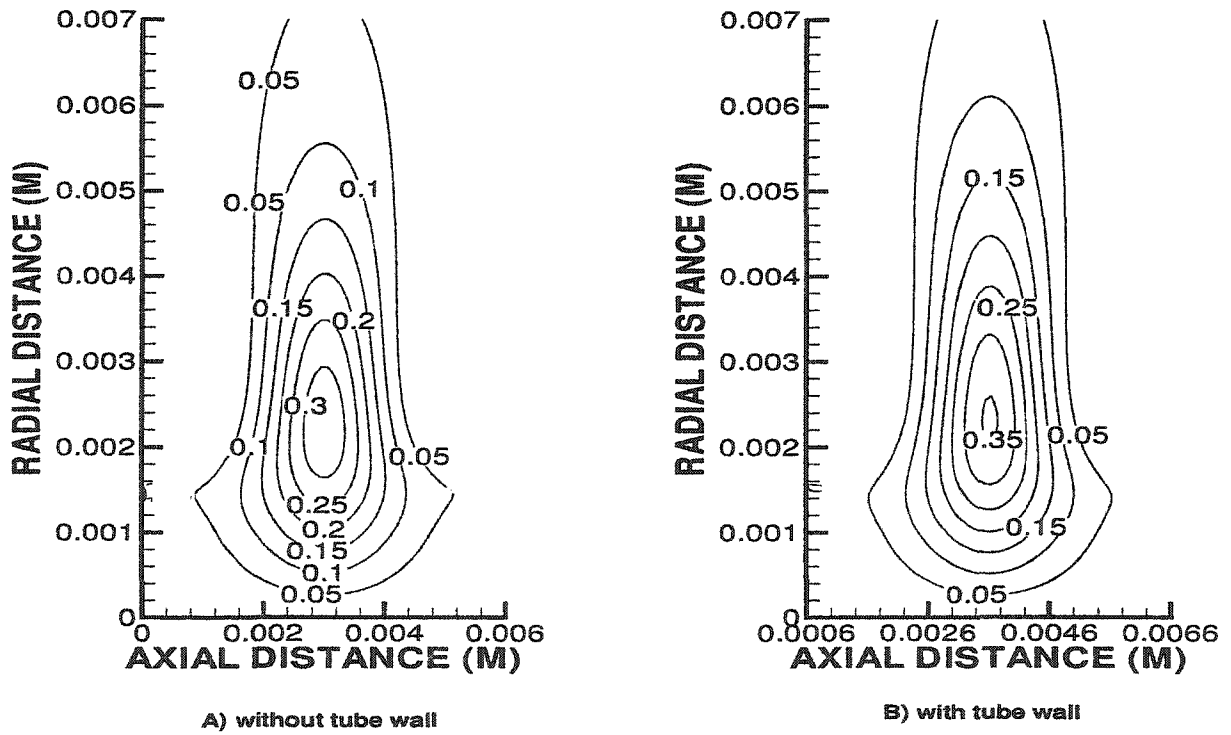

Fig. 4.11 Isocontours of radial velocity with channeled and unchanneled flows at plug inflows of 0.5 meters per second.

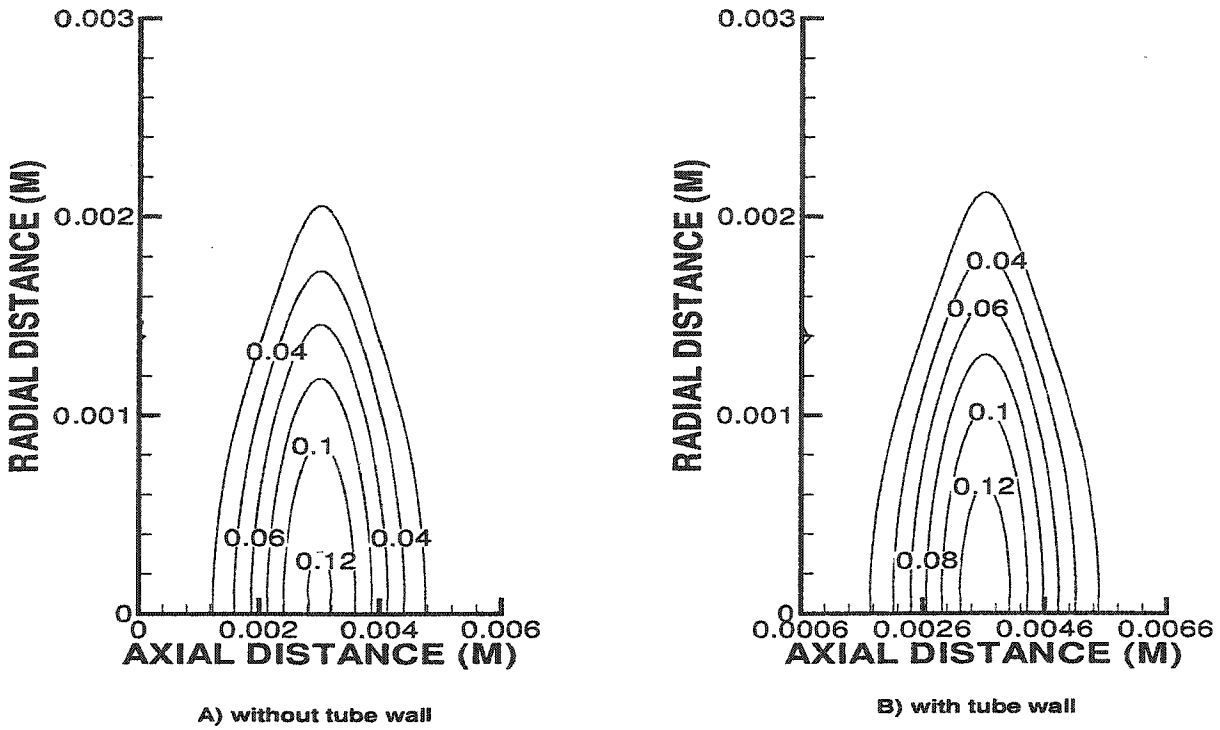

Fig. 4.12 Isocontours of gage pressure with channeled and unchanneled flows at plug inflows of 0.5 meters per second.

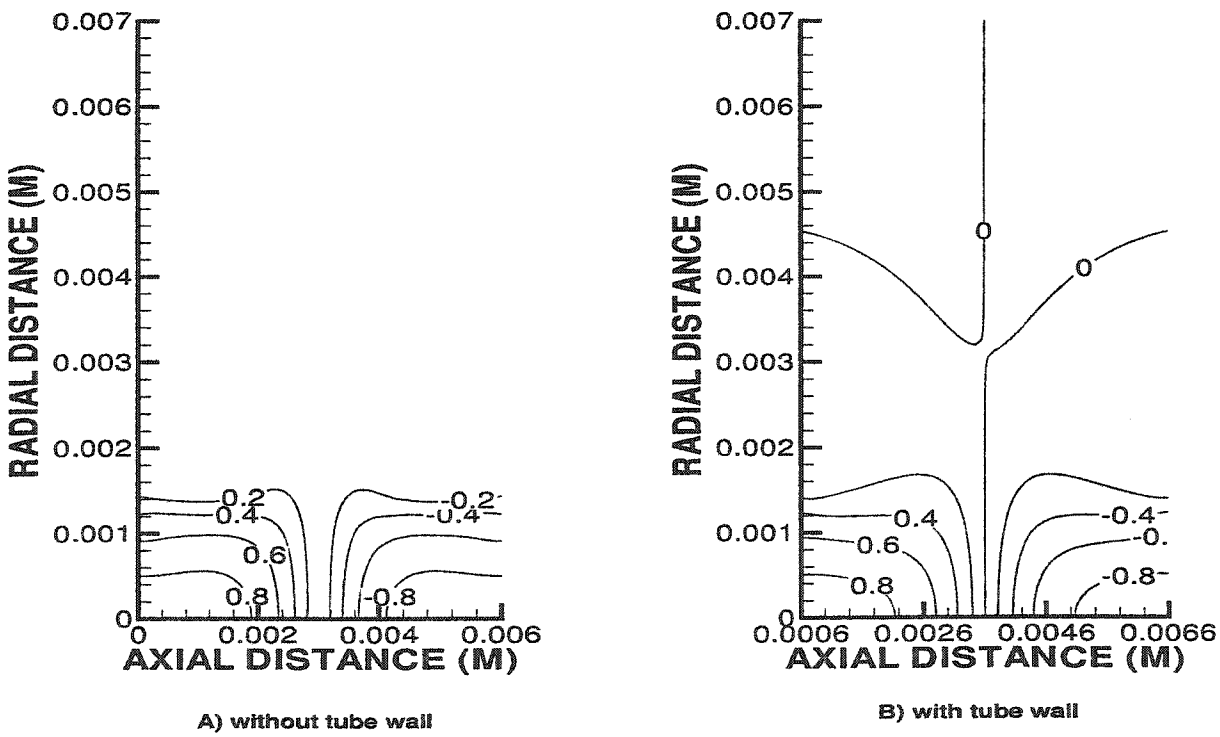

Fig. 4.13 Isocontours of axial velocity with channeled and unchanneled flows at parabolic inflows of mean velocity of 0.5 meters per second.

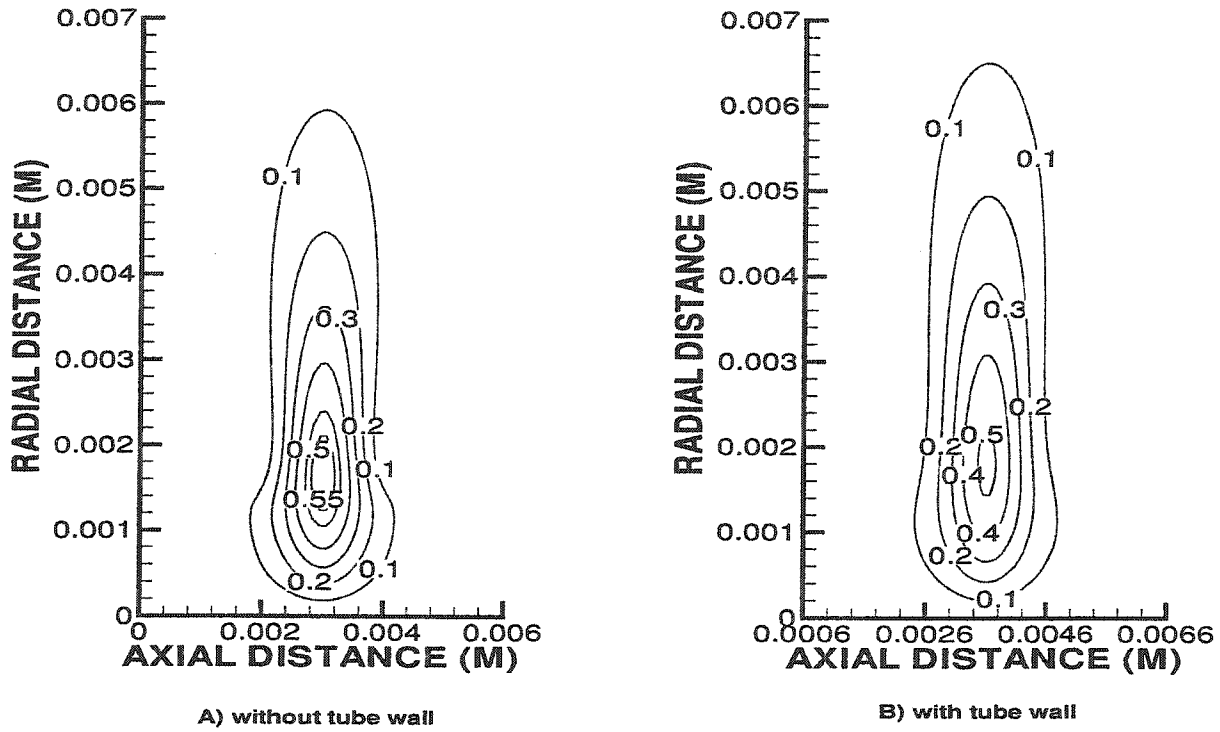

Fig. 4.14 Isocontours of radial velocity with channeled and unchanneled flows at parabolic inflows of mean velocity of 0.5 meters per second.

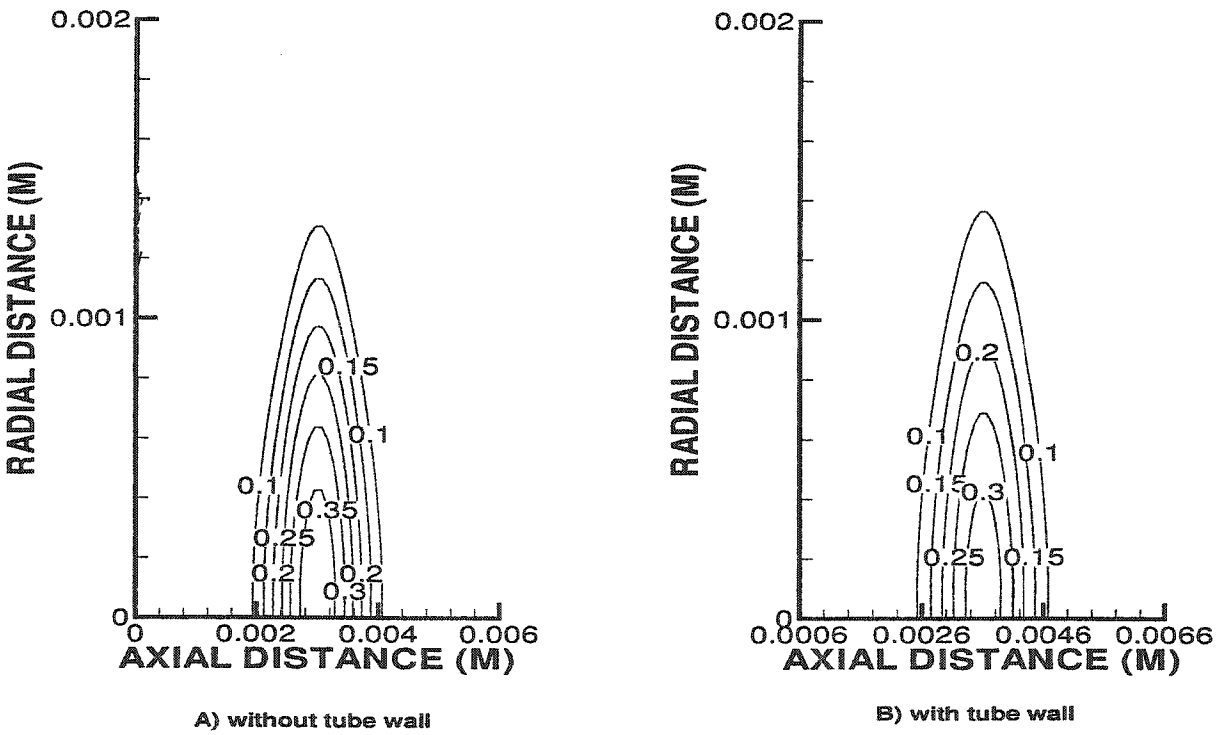

Fig. 4.15 Isocontours of gage pressure with channeled and unchanneled flows at parabolic inflows of mean velocity of 0.5 meters per second.

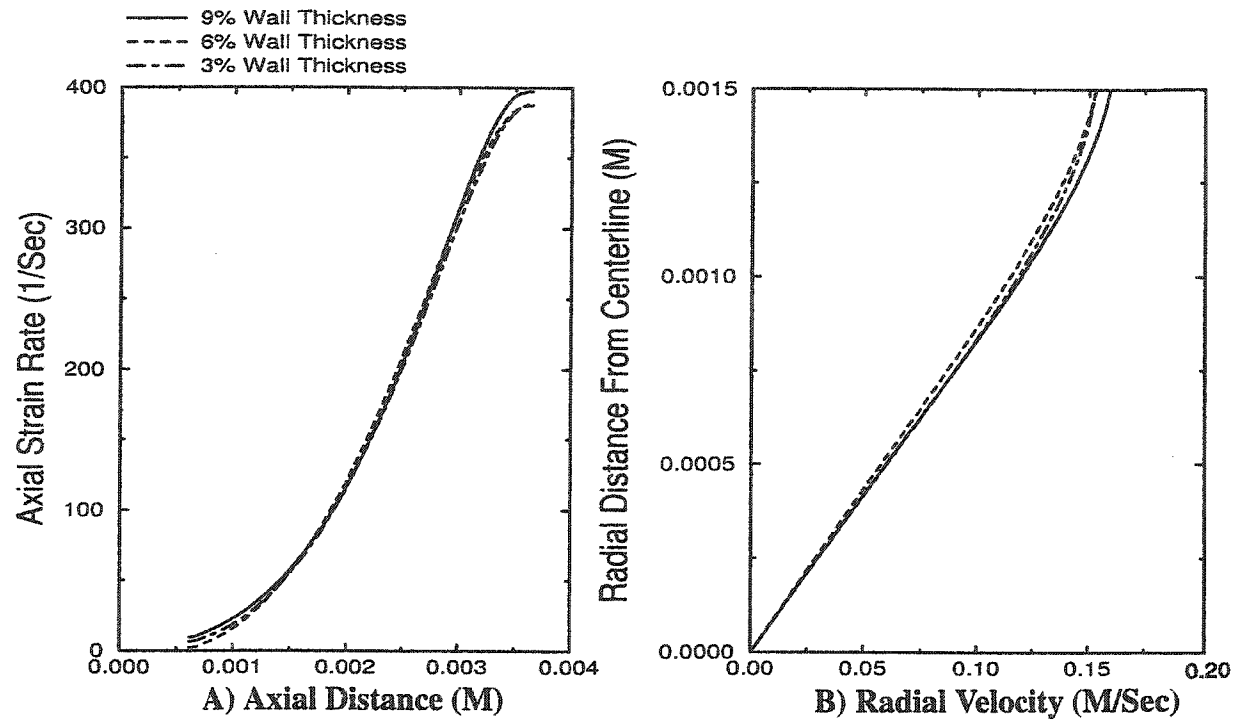

Fig. 4.16 Effects of wall thickness on (A)axial strain rate along the axial centerline; and (B)radial distribution of radial velocity, at one-half the axial distance between the tube exit and stagnation plane. Plug inflows are 0.5 meters per second.

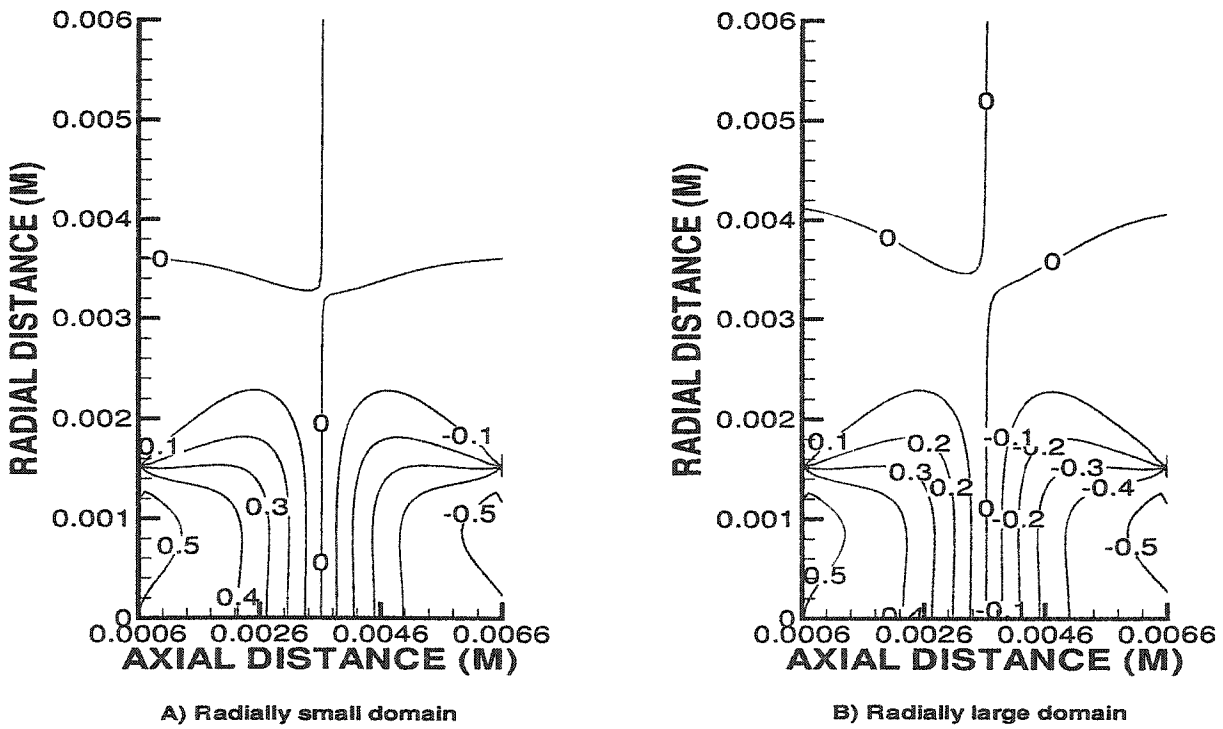

Fig. 4.17 Isocontours of axial velocity with (A)radially underextended and (B)extended domains, at plug inflows of 0.5 meters per second.

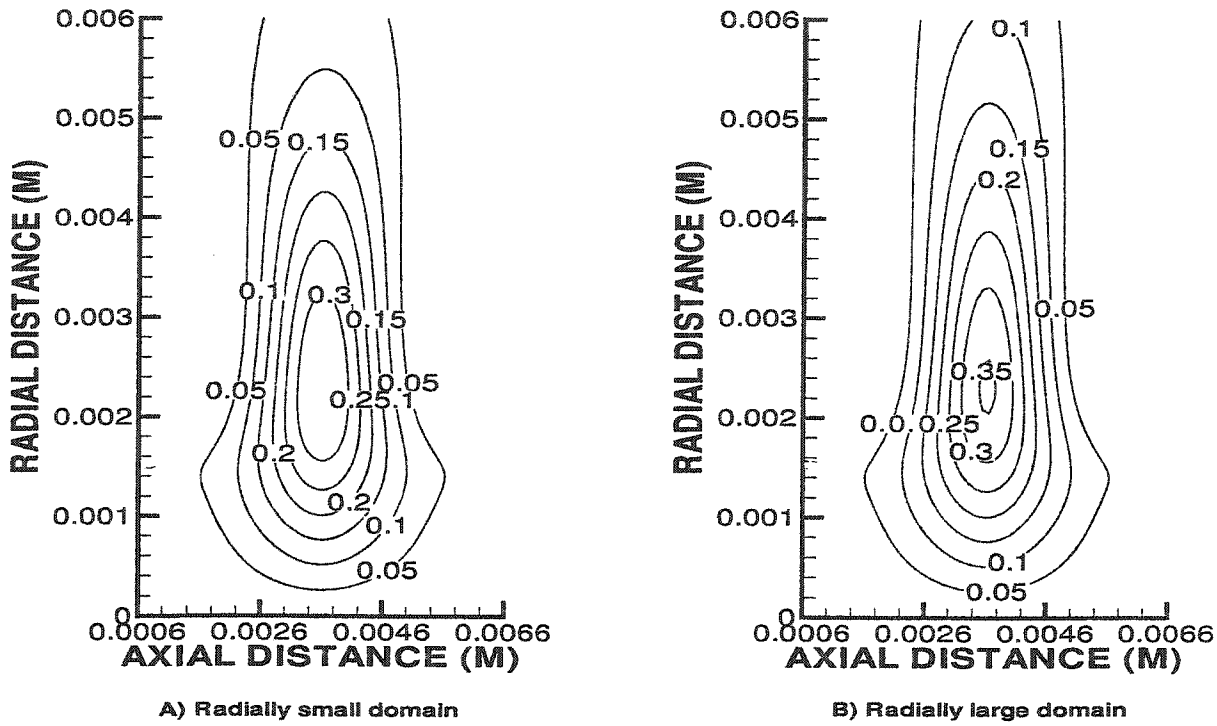

Fig. 4.18 Isocontours of radial velocity with (A)radially underextended and (B)extended domains, at plug inflows of 0.5 meters per second.

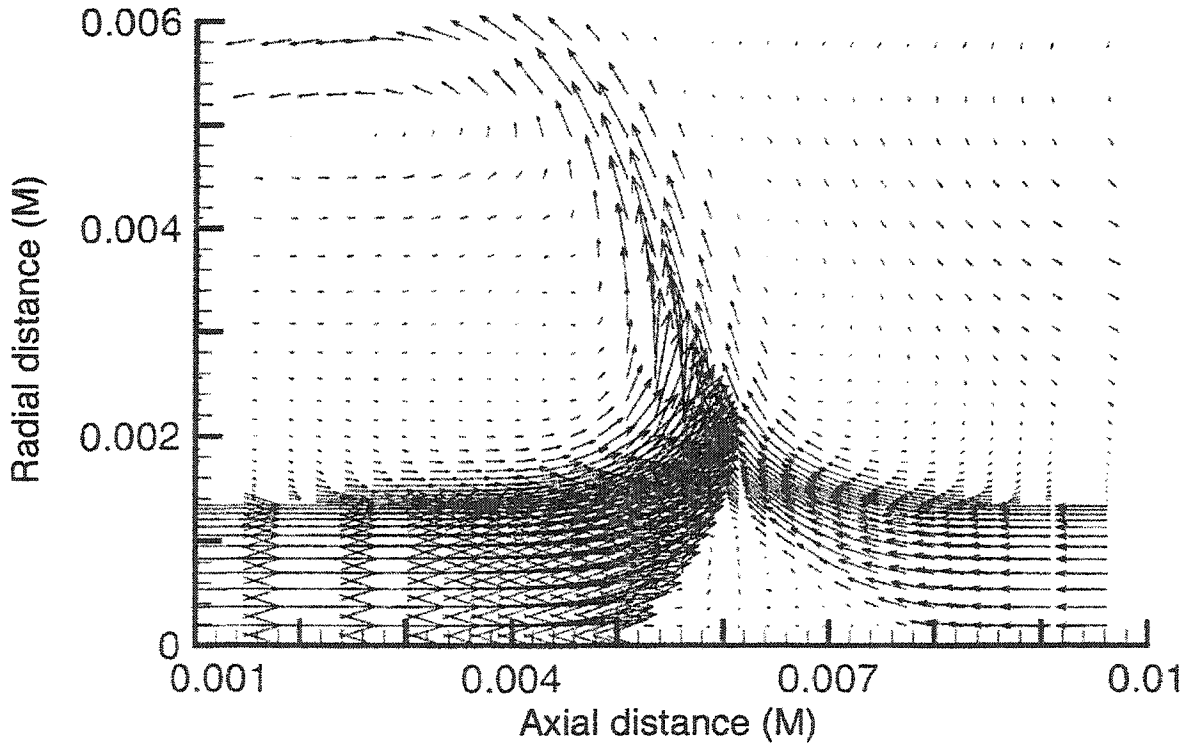

Fig. 4.19 Velocity vector plot of pure hydrogen versus air opposed jet flows with a radially under-extended domain at plug inflows of 4 meters per second. Oxidizer is on right side.

CHAPTER V

OPPOSED JET DIFFUSION FLAMES WITH PLUG INFLOW BOUNDARIES

Nearly all numerical studies on the flame structure and extinction characteristics of counterflow hydrogen-air nonpremixed flames have utilized one dimensional models based on a stream function similarity transformation, and one of four different input boundary conditions. The limitations associated with one dimensional approximations and their applications stem from the problem of characterizing radial gradients in flame composition and temperature. Desired idealities in various relationships between a uniform radial strain rate and a specific input axial strain rate - equal to the maximum axial velocity gradient of the cold oxidizer flow just ahead of the flame zone - cannot be realized. Obviously the requirement of infinite nozzles located infinitely far apart (plug and potential flow assumptions) cannot be realized experimentally. But the real problem that limits the usefulness of any one dimensional approximation for the axisymmetric case is that it cannot properly account for the multidimensional effects associated with relatively small jet dimensions, velocity profiles, and mixing zones. In particular, the one dimensional models are incapable of accepting arbitrary experimental velocity boundary conditions at the nozzle/tube exits, e.g. a parabolic profile, which prevents direct comparisons with same of the experimental data.

Experimentally, it has been shown that the structure and extinction characteristics of opposed jet diffusion flames are significantly influenced by different inflow profiles [14-21]. In addition, early findings in the preceding chapter indicate that the different inflow boundary condi-

tions of non-reacting opposed jets result in uniquely two different impingement characteristics in the axial and radial strain rates, which are critical in characterizing the diffusion flame.

Two dimensionally, few attempts have been made to characterize the flame at different inflow boundary conditions [40, 43-47]. Moreover, these works are confined to highly diluted fuel, with relatively low strained flows, where two dimensional effects on the flame and flowfield are maximal, but flame extinction is not achieved.

This study begins with the axisymmetric opposed jet configuration, using plug inflow boundaries at relatively short separation distance (L/D=1). The study first characterizes the structure of a diffusion flame at lightly strained conditions. Then, details of a flame responding to plug inflow boundaries at the extinction limit are examined. As a part of the validation process, the plug flow flame simulations are directly compared with independent laser diagnostic flow composition experiments performed with high contraction-ratio nozzles that generate nearly uniform velocity fuel and oxidizer jets (Fig. 5.1). Subsequently, the counterflow diffusion flame responding to parabolic inflow conditions is presented in the next chapter.

The present chapter is organized in the following manner. First, diagnostic details related to application of the current numerical model are given in Sec. 5.1. This is followed by comparative discussion of numerical and experimental results presented in Sec. 5.2. Then, the characteristics of the opposed jet diffusion flames under lightly strained conditions are examined in Sec. 5.3. Finally, the details of flames at the extinction limit are addressed in Sec. 5.4.

5.1 Diagnostics and Application of the Numerical Model

From a numerical application viewpoint, there are three issues that define the limitation and validity of the numerical solutions. The first issue involves discretization of the domain, in

which the discretized governing equations are solved with appropriate boundary conditions. The second involves the resolution of key temperature and concentration gradients. Finally, the third involves various orders of artificial dissipations.

The accuracy of the problem solution depends on and can be greatly improved with well constructed and appropriately sized grids that suitably represent the domain. To investigate the grid independency of results, the pure hydrogen-air opposed jet diffusion flame is simulated using the plug inflow boundaries at a mean oxidizer input velocity of six meters per second. Figure 5.2 represents the centerline axial temperature and OH mole fraction distribution in response to different axial grid density, ranging from 12 to 18 spaces per millimeter. The oxidizer is on the right. In this study, greater emphasis is given in the axial direction, due to the higher gradient in thermochemical and flow properties. The results clearly show that the distributions converge as the grid density increases. No real change in the distributions of temperature and OH concentration are seen at and above the grid density of 15 spaces per millimeter. Therefore, this grid density was provisionally selected to simulate the entirety of counterflow diffusion flames in this study.

One of the inherent difficulties associated with the numerical simulation of a strained counterflow diffusion flame is that an independent and accurate investigation of grid independency in a solution is not possible at relatively high input velocity (e.g. higher than ten meters per second). This is due to the fact that the relatively small jet dimensions (order of millimeters) cause strong coupling effects between artificial dissipations and different grid densities at higher velocities. As a result, the simulated flame characteristics can vary with different dissipation coefficients and grid densities that altogether limit the accuracy and independency of the solution. In more typical applications, the grid independency in a solution is performed using invariant input conditions and dissipation coefficients.

In an effort to resolve the validity of the current grid density approach, high input oxidizer velocities are qualitatively investigated by examining the maximum temperature difference per grid space at the axial centerline as a function of oxidizer input velocities, using the Yetter et al. kinetic model. The maximum temperature difference is chosen for this investigation because most thermochemical and chemical kinetic properties are strongly dependent on temperature.

The results in Fig. 5.3 indicate the peak temperature difference occurs at an oxidizer input velocity of 12 meters per second (208K or 208K/(1/15mm)=3120K/mm). This peak temperature difference and resultant gradient decreases on either side due to changes in both centerline peak temperature and flame thickness. Also, the peak temperature difference is only about 12 percent higher than that where the first grid independency test was conducted (187K at 6 meters per second). Since the current study is focused on both lower strain rates (with oxidizer input velocity less than or equal to 6 meters per second) and higher strain rates (velocity greater than or equal to 22 meters per second), the maximum temperature gradients observed in these regions are 187K per grid space or less. Therefore, the sufficiency and adequacy of current grid density is considered established for this study.

The third numerical issue that hinders the accuracy and validity of solutions is the artificial dissipations associated with the spatially second order accurate central difference scheme. There are two types, namely, second and fourth order dissipations. The second order dissipation is often used to reduce the numerical overshooting/undershooting problems at a point of discontinuity. The fourth order dissipation is implemented to eliminate the numerical odd-even points decoupling problem. The dissipation terms are often seen as "extras" to the discretized governing equations, in which excessively large dissipations can compromise the integrity of governing equations (consistency failure) [60]. Accordingly, dissipations are chosen in a manner that their

addition to the set of discretized governing equations satisfies a minimum stability in solutions, yet their contribution to the system of equations must be smaller than overall truncation errors.

As stated earlier, the current computational model includes decoupled governing equations, namely flow and species sets. Therefore, each set of equations responding to the damping coefficients is examined separately.

For the flow set, the radial distribution of gage pressure and axial velocity at the tube exit are examined at various fourth order dissipations, as shown in Fig 5.4. Clearly, the results show the numerical oscillations of the flow properties. As higher damping coefficients are utilized, the gage pressure oscillations are dissipated, achieving minimum sufficiency with a fourth order damping coefficient of 0.8 (In the code, the actual coefficient is 0.8/24 = 0.034). No overshooting/ undershooting problem is seen here, and as a result, the second order damping is not needed in this set.

Next, the effects on species distributions of various damping coefficients are examined. The results shown in Fig. 5.5 indicate that H_2O mole fraction along the axial centerline exhibits an under-representation (negative value) just before a large drastic increase. This under-representation is physically unreal and may contribute errors to the overall characteristics of a flame. As a higher second order coefficient is utilized, the numerical undershooting damps, and achieves minimum sufficiency with a second order damping coefficient of 0.03 (or actual coefficient of 0.005). Because spatial oscillation is not observed in the species set of governing equations, fourth order dissipation is not implemented here. Overall, these sets of coefficients are uniformly used for the entirety of diffusion flame simulations.

5.2 Comparisons with Experimental Data

Because numerical study always contains (inherits) uncertainties associated with the discretization of governing equations, any validations of the numerical combustion model, in conjunction with tests of the accuracy and limitations of numerical solutions, should be explored prior to detailed analyses of flame characteristics over the full range of strained conditions.

Therefore, simulations were performed to compare the computed structure of flames with experimental measurements by Wehrmeyer et al. [18], who used a UV-Raman scattering technique to measure the distribution of major species concentrations along the axis of a counterflow diffusion flame. The input oxidizer was 21% O_2 and 79% N_2 in volume with a volumetric rate of 2.04 liters per minute, whereas the input fuel was 100% H_2 with a volumetric rate of 5.79 liters per minute. The pyrex nozzle tube diameter and jet separation distance were each 5 millimeters. The measurements of H_2O, H_2, OH, O_2, and N_2 were conducted with UV-Raman imaging system, providing time averaged linewise measurement of high precision (2%) and high spatial resolution (160 μm) for the scalar measurements. Laser Doppler Velocimetry (LDV) was used in separate experiments to measure the oxidizer side axial velocity gradient. For this comparison, the numerical temperature and species mole fraction distributions along the axis centerline are presented as a function of the atomic hydrogen mixture fraction, using the following expression:

$$\xi_H = \frac{Z_H}{Z_{H_{fuel}} + Z_{H_{oxidizer}}}$$

where Z_H is the mass fraction of elemental hydrogen, and is estimated using

$$Z_H = \frac{2X_{H_2} + 2X_{H_2O}}{2X_{H_2} + 18X_{H_2O} + 32X_{O_2} + 28X_{N_2}}$$

The results shown in Fig. 5.6 indicate that the calculated H_2O and temperature distributions, using both chemical kinetic models, agree well with the experimental measurements; the

deviations are well within the measurement uncertainties, especially for steam. Qualitatively, the Yetter et al. kinetic model predicts even closer resemblance in the temperature and steam distributions than the Jachimowski model.

However, the calculated OH distributions from both models display a significant difference (excess) over the measured profile in Fig. 5.6, although the Jachimowski model shows slight improvement in its prediction.

Previously, a similar excess deviation in the OH distribution was reported by Brown et al. [19], where a 100% hydrogen-air diffusion flame was compared with an one dimensional approximation at an oxidizer-side axial strain rate of 50 per second. Their calculation predicted a larger peak OH (mole fraction of 0.023) compared to their measurement of 0.014. Also, their corresponding half width of OH, over the atomic hydrogen mixture fraction scale, was smaller than their calculated half width. They postulated these deviations were mainly due to oversimplification in the system of governing equations (1-D); incompleteness in their model, which did not account for the thermal diffusion effect; and deficiency in their chemical kinetic model which did not include any third body efficiencies. The current OH comparisons in Fig. 5.6 suggest that the deviation in OH was not a result of limitation in the dimensionality, but possibly a result of inadequacy in the thermal diffusion and kinetic models.

To further investigate the behavior of OH profiles at various input strain conditions, simulations and data were compared at two additional strain rates, as shown in Fig. 5.7. The results for all three inputs indicate that the calculated OH profiles from the different kinetic models are nearly identical, except the Yetter et al. model predicted slightly higher peak values. However, the experimental profiles differ considerably with strain rate.

The measured *peak* OH at low strain rate shows good agreement with the predicted result in Fig. 5.7. Qualitatively, this agrees with an early finding by Brown et al.[19], where the measured and calculated peak OH were reported in fairly good agreement at near adiabatic equilibrium conditions with very low strain rate. However, the measured width of the OH profile is much narrower than the (nearly identical) computed profiles at the lightly strained condition.

As the flame becomes more strained in Fig. 5.7, the deviations between measured and calculated peak OH become greater, but the distributions in width of measured OH improve significantly. Presently, a simple explanation of this behavior is not evident. And, as a final note on Fig. 5.7, both kinetic models predict nearly identical centerline airside maximum axial strain rates (MLSR) at each condition, which however are 60 to 80 percent of those measured by LDV in these cases.

Finally, a third set of simulations was conducted to compare 2-D numerical results with similar experimental results [18] for temperature and species distributions in a physical space, using two different strain rate inputs and a diluted fuel stream. The flames were simulated for an identical configuration as in previous sets [18], and differ only in the fuel being 50% hydrogen diluted by nitrogen. Qualitatively, the results in Figs. 5.8-5.10 show that calculated profiles for H_2, O_2, H_2O, and T using Yetter kinetics closely resemble with the measurements. In particular, at the low strained condition, both calculated and measured profiles display near identical distributions, with only slightly higher water vapor data (Fig. 5.8). At the higher strain condition, the measurement displays a relatively thinner flame (Fig. 5.9). Relatively, the Yetter et al. model agrees more closely, i.e. it predicts a higher and narrower peak temperature and H_2O profile than the Jachimowski model. Thus, the Yetter et al. model provides a significantly closer resemblance to the UV Raman measurements at both input strain rates.

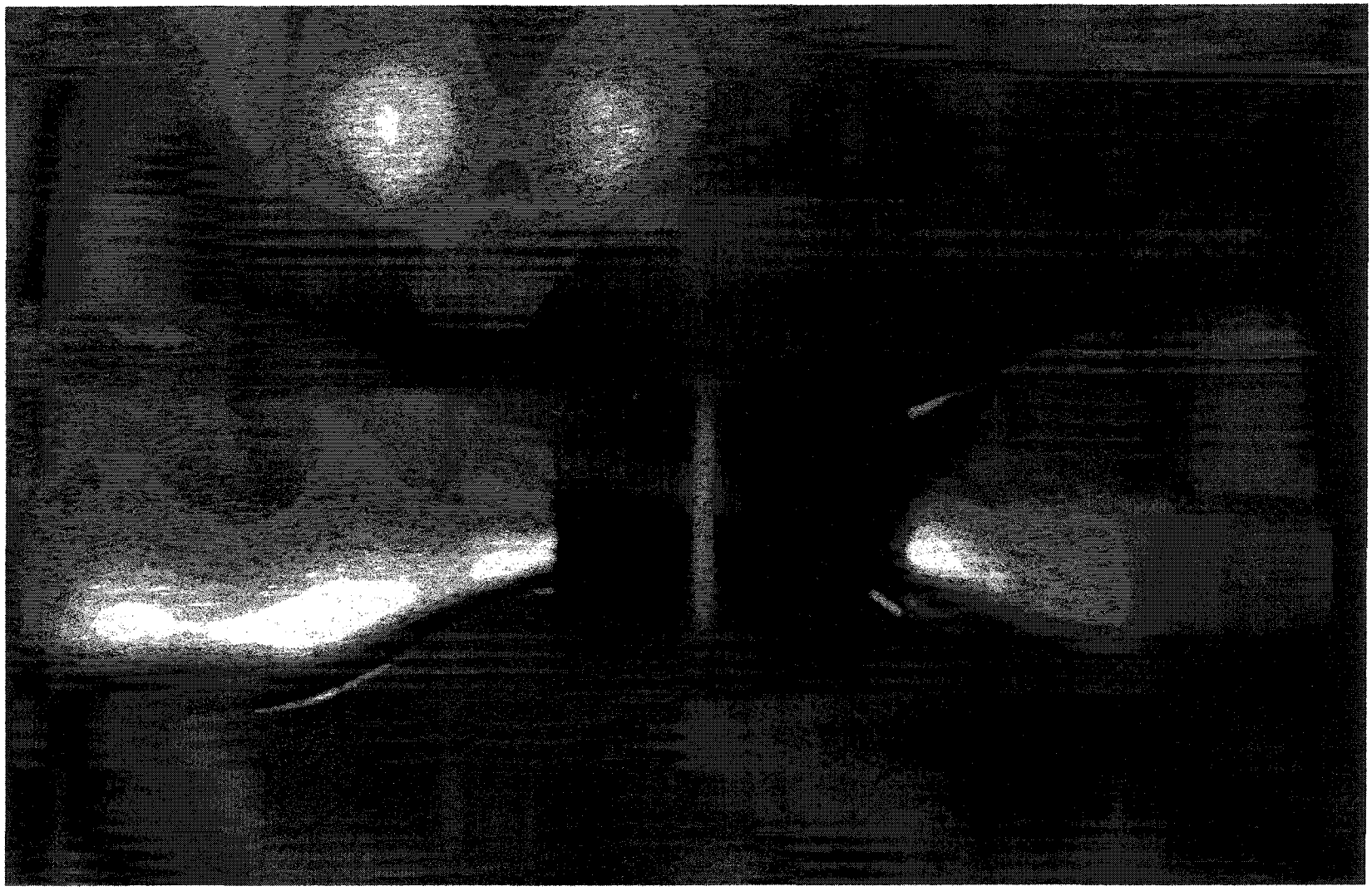

Fig 5.1 Photographic image of lightly fueled opposed jet diffusion flame using nozzle configuration [63].

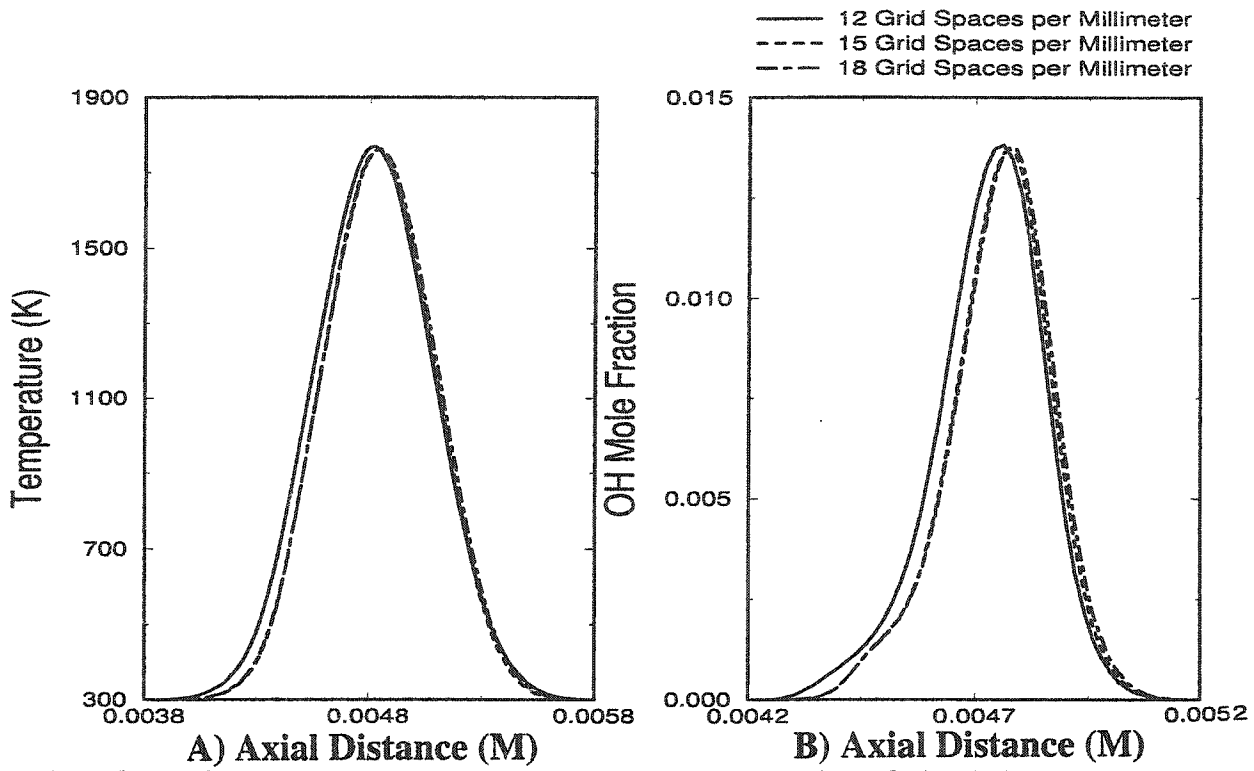

Fig 5.2 Centerline temperature and OH mole fraction distribution of plug inflow induced 100% hydrogen air flames, at an oxidizer input velocity of 6 M/Sec for different grid densities. Oxidizer is on right side.

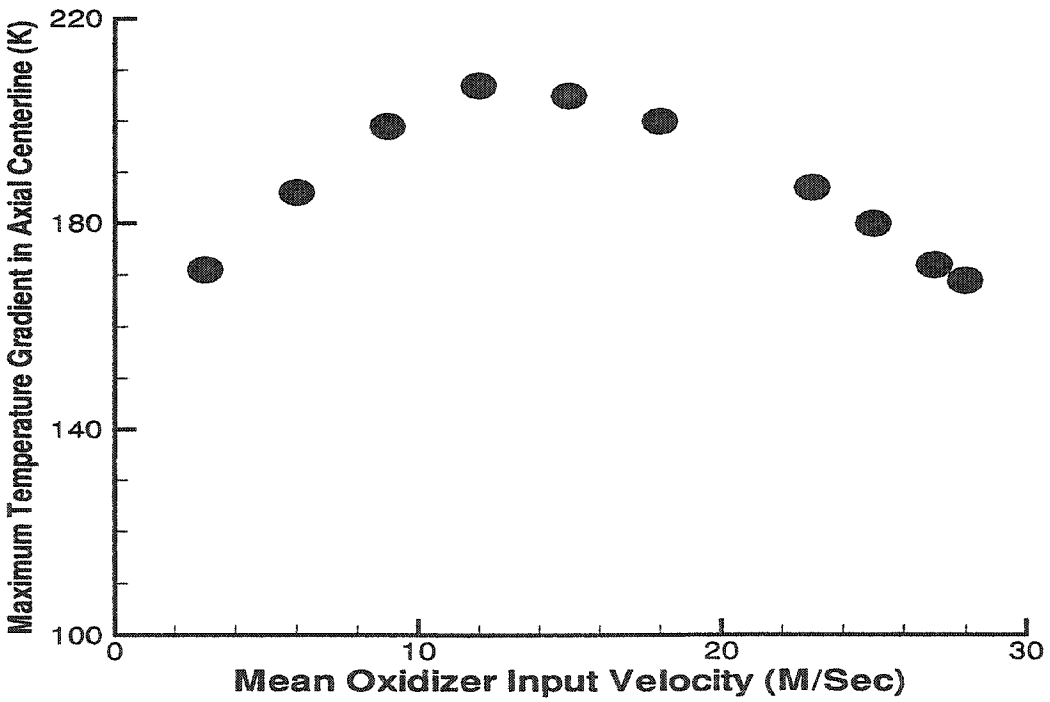

Fig 5.3 Maximum centerline temperature difference per grid space (15 grids per millimeter) for plug inflow induced 100% hydrogen-air flame at various oxidizer input velocities.

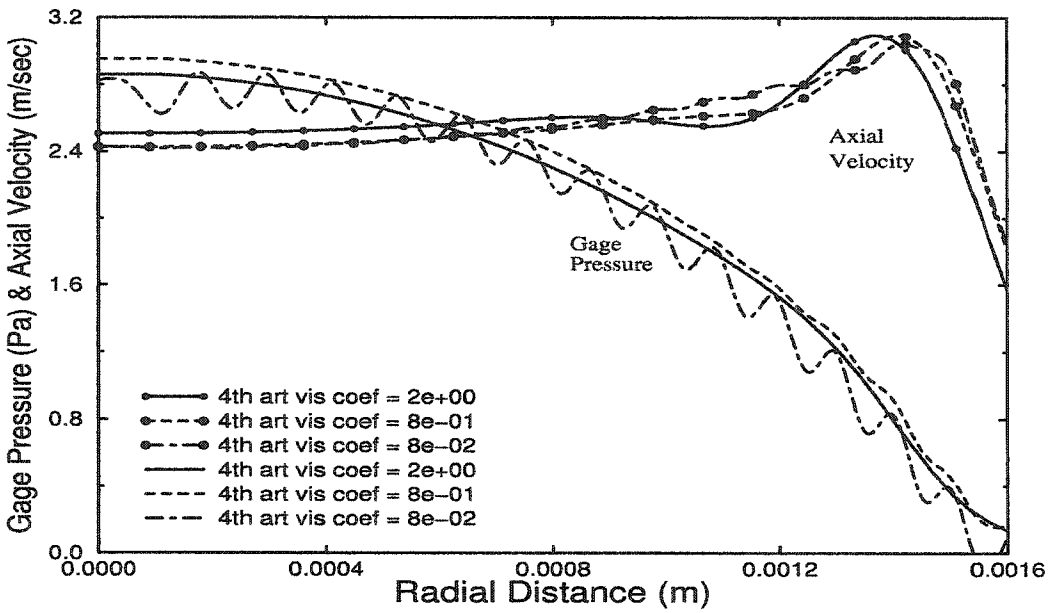

Fig 5.4 Effects of fourth order artificial dissipation on radial distributions of tube exit axial velocity and gage pressure at oxidizer plug inflow of 2.5 M/Sec (100% hydrogen-air flame).

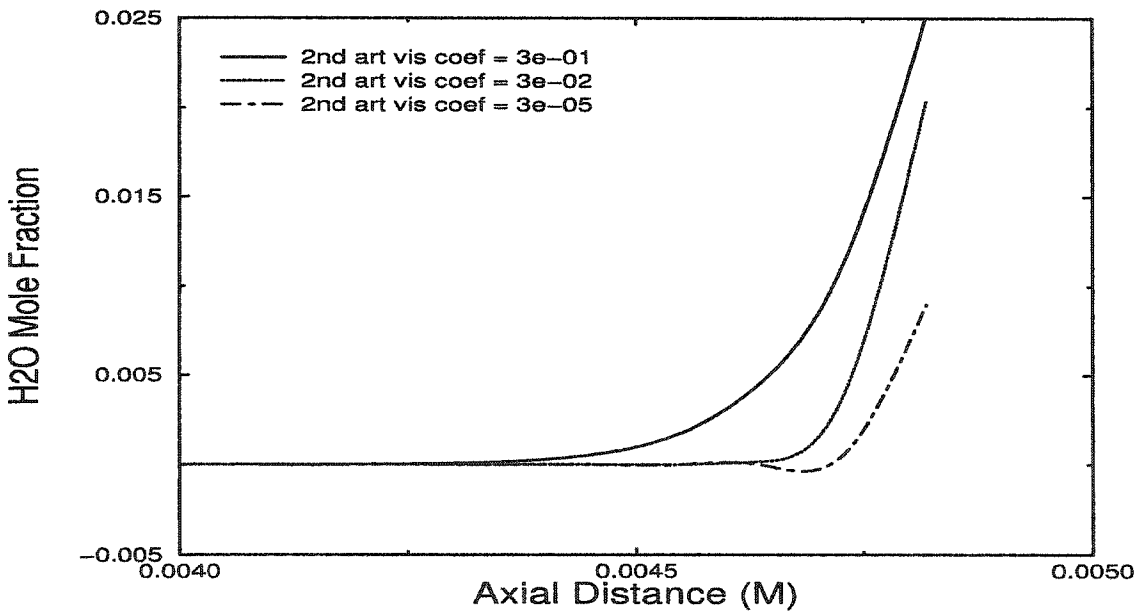

Fig 5.5 Effects of second order artificial dissipation on centerline H_2O mole fraction distribution at oxidizer plug inflow of 2.5 M/Sec on right side (100% hydrogen-air flame).

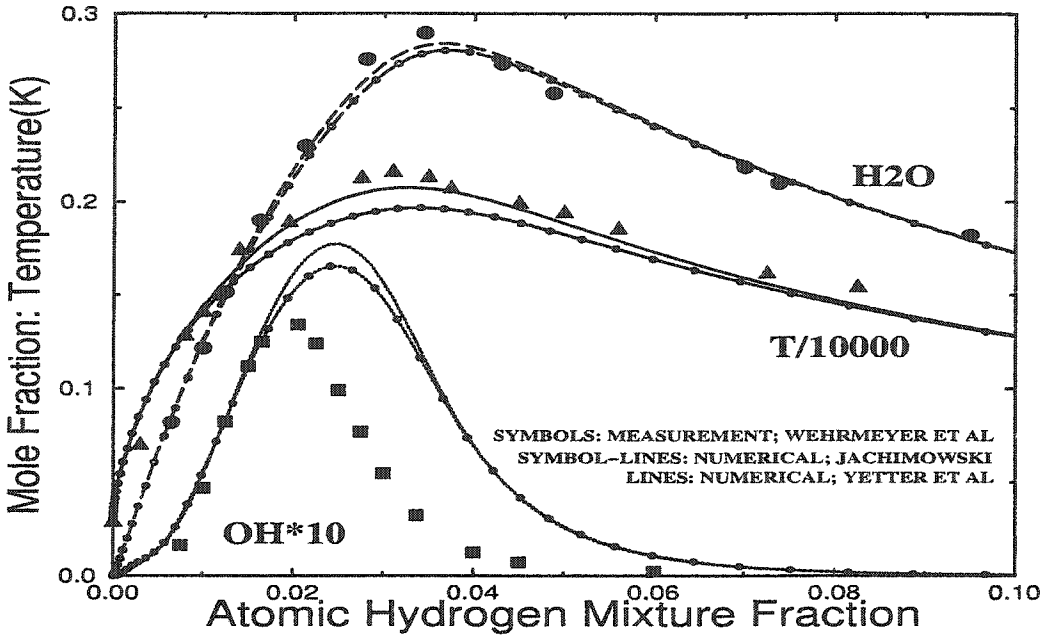

Fig. 5.6 Measured and calculated centerline species mole fraction and temperature profiles for 100% hydrogen-air plug inflow induced flame at V_o = 1.73 M/Sec and V_f = 4.91 M/Sec.

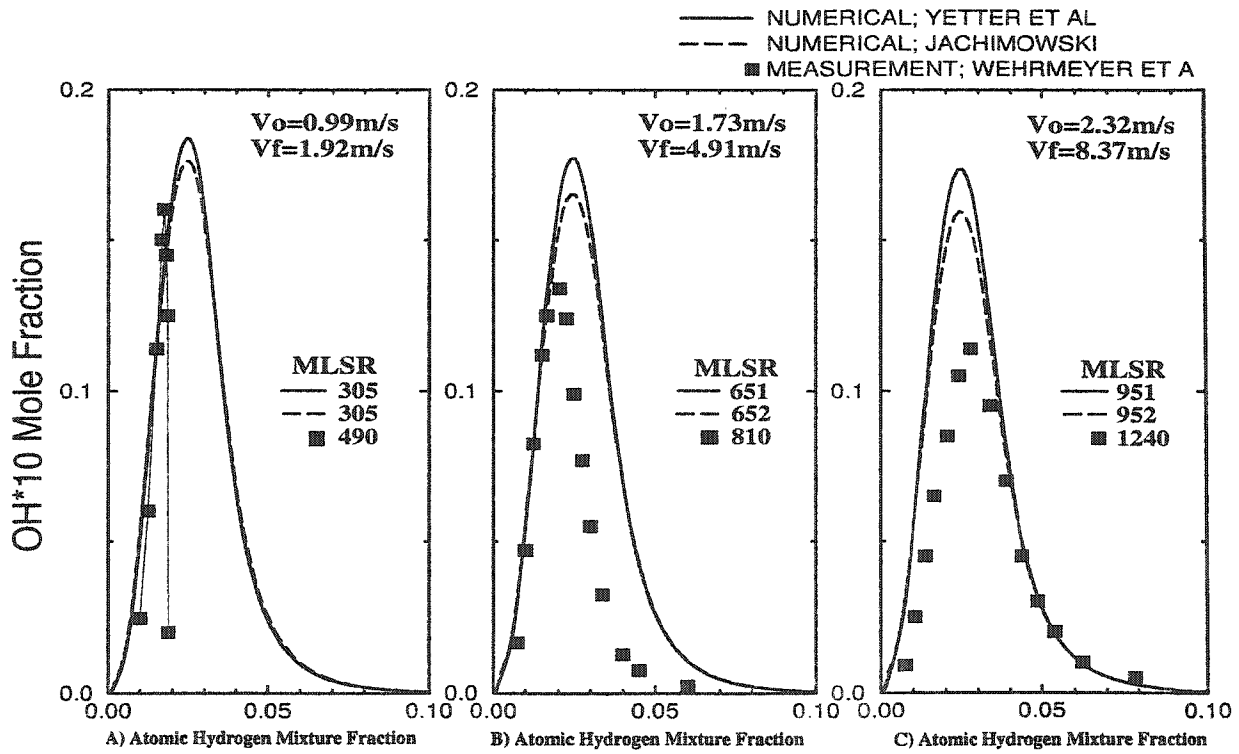

Fig. 5.7 Measured and calculated centerline OH mole fraction profiles for 100% hydrogen-air plug inflow induced flame at various input conditions.

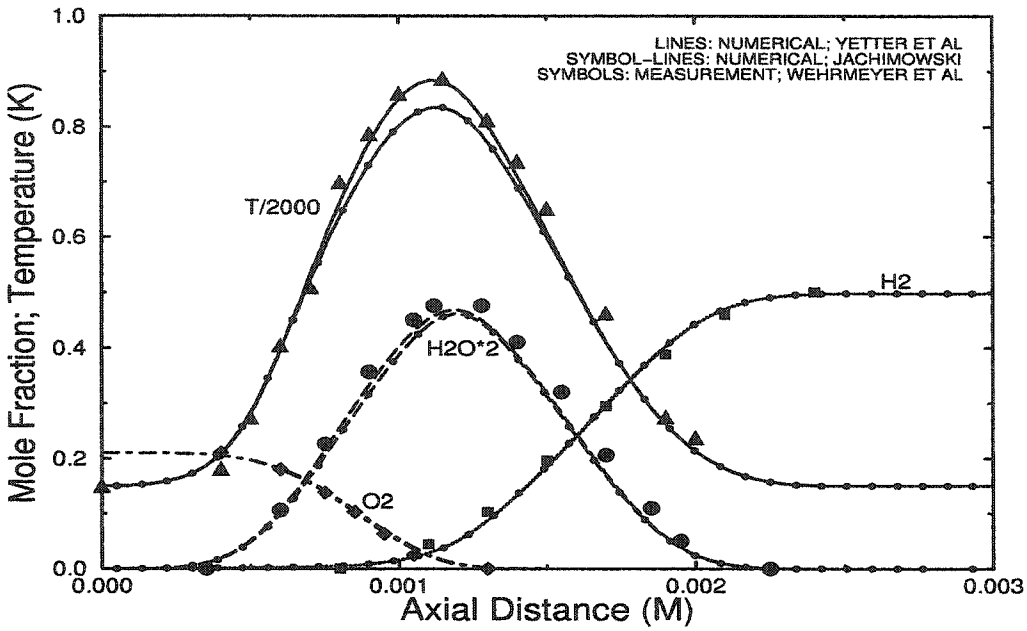

Fig. 5.8 Measured and calculated centerline species mole fraction and temperature profiles for 50% hydrogen-air plug inflow induced flame at V_o = 2.25 M/Sec and V_f = 3.15 M/Sec. Fuel is on right side.

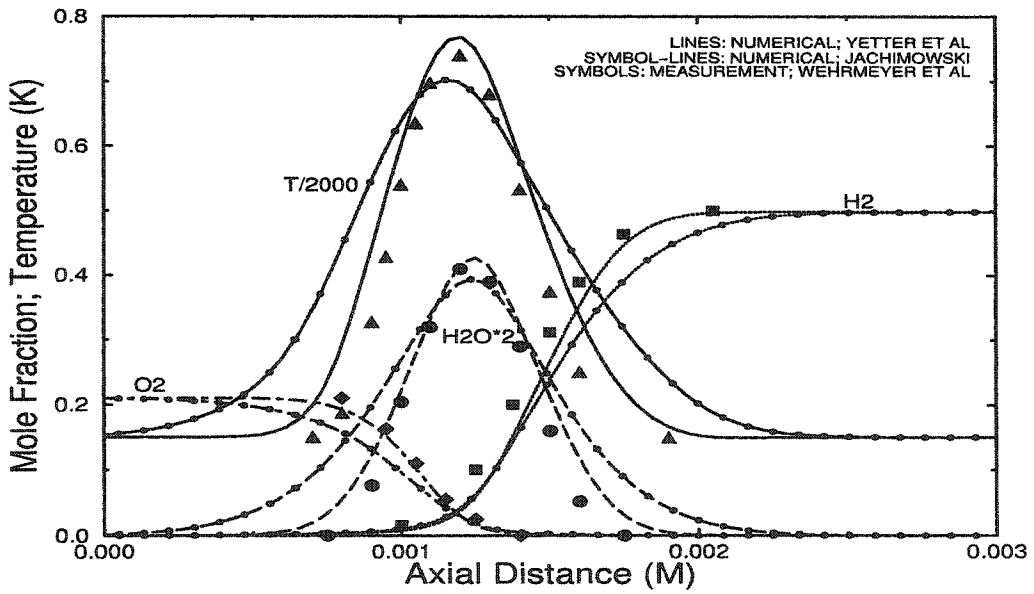

Fig. 5.9 Measured and calculated centerline species mole fraction and temperature profile for 50% hydrogen-air plug inflow induced flame at V_o = 8.33 M/Sec and V_f = 11.44 M/Sec.

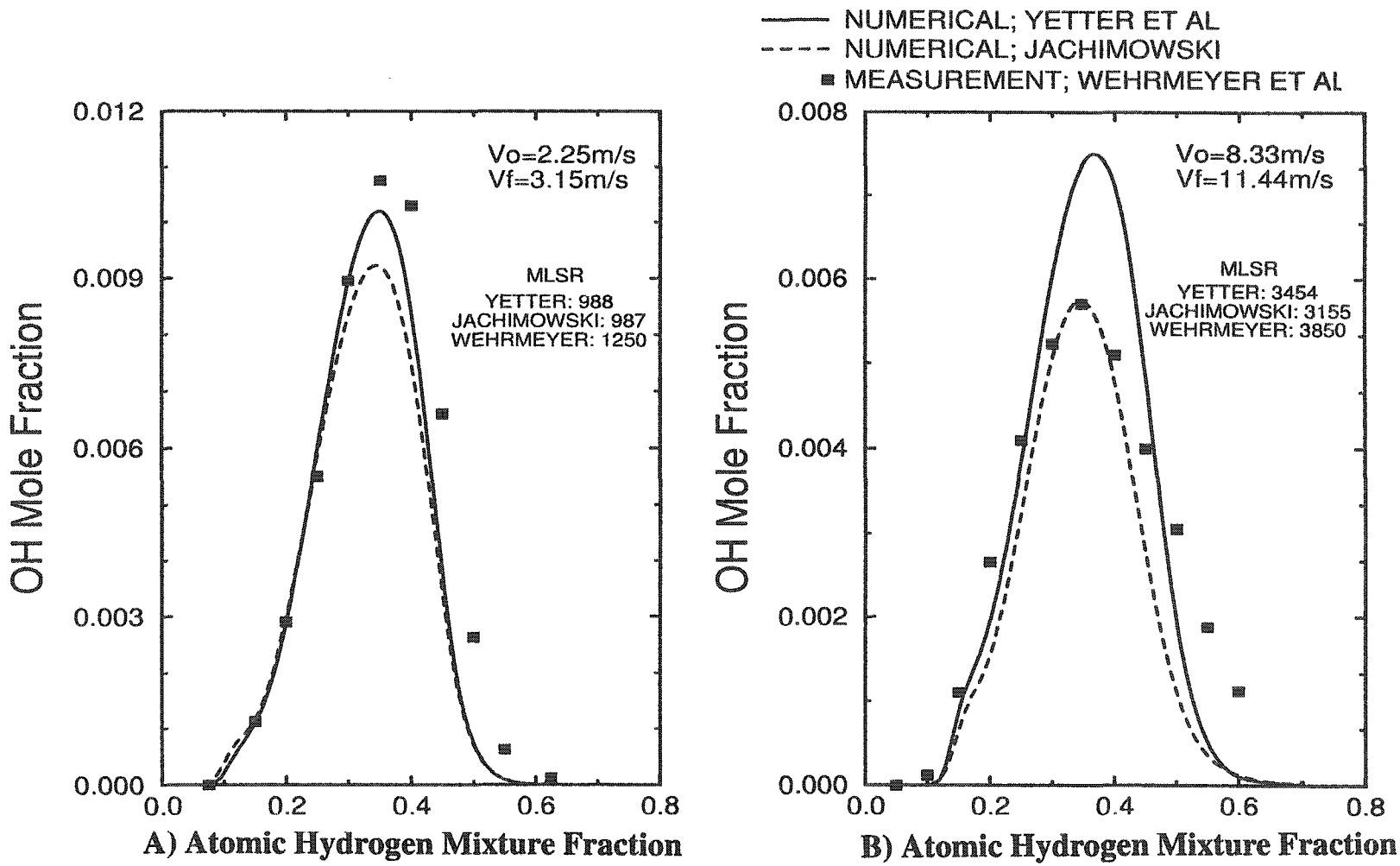

Fig. 5.10 Measured and calculated centerline OH mole fraction profiles for 50% hydrogen-air plug inflow induced flame at various input conditions.

The OH profiles for both measurement and calculations also show surprisingly good agreement (Fig. 5.10). No significant deviations in its peak or FWHM values are observed, as in previous sets for 100% hydrogen-air. Comparatively, the Yetter et al. model correlated slightly better, especially at the lightly strained condition. Finally, the LDV measured airside centerline maximum local strain rates (MLSR) are slightly but consistently higher than the calculated values, similar to that found in Fig. 5.7.

5.3 Diffusion Flames at Lightly Strained Conditions

5.3.1 Coupling Effects of Diffusion Flames

The input velocity profiles have a significant influence on the overall structure and extinction characteristics of diffusion flames. Adversely, the combustion process in a narrow confined zone has a profound influence on the aerodynamics of the flowfield, which ultimately influences the flame itself. Therefore, to examine their coupling effects, a simulation was performed to compare the flow impingement characteristics in pre- and post-ignition states. The flame was generated with 20% hydrogen fuel, in nitrogen, impinging dry air. The impingement flows were simulated using tubes with a diameter and separation distance of 0.01 meters. The fuel velocity that balance an air velocity of 1.6 meters per second is calculated based on the one dimensional momentum equation. The diffusion flame is simulated using the Clarke et al. kinetic model [48].

The study shows that the reacting flows have two distinctively important characteristics differing from nonreacting flows. The first distinction is the coexisting (overlapping) zone of fuel and oxidizer is much smaller for the post-ignition (Fig. 5.11) than the pre-ignition state. This indicates that most of the fuel and oxidizer are consumed in a very narrow zone through combustion, even though the chemical process occurs at a finite rate. The fuel starts dissociating at the pre-

ignition edge of the oxidizer on the fuel side, and similar behavior is observed with the oxidizer. This confirms previous works [15-21, 31-45] that the combustion process occurs in a narrow finite zone where the fuel and oxidizer coexist, and zone becomes infinitely thin in the case of the idealized Burke-Shumann diffusion flame.

The other distinctive characteristic is that because the combustion process is exothermic, the radial velocity gradient expands significantly. Its magnitude at the flow stagnation point is approximately 1.5 times that of the nonreacting flows (Fig. 5.11). However, as shown in Fig. 5.13, the main flow expansion occurs within the flame zone. This indicates that conductive heat transfer against a counterflow beyond the flame edges is not significant, rather a large portion of thermal energy is convected (swept away) into the downstream. A large downstream heat release adversely compresses the upstream flows, causing a rapid deceleration of the axial component of oxidizer in the pre-flame region. The axial velocity attains a relative minimum just before the oxidizer edge of the flame, representing the oxidizer mass flow rate (burning rate) to the flame. Then, the large heat release ultimately accelerates the axial velocity within the flame, uniquely defining the characteristics of the reacting flows.

At the tube exits, heat release affects the radial distribution of both the axial and radial velocities, as shown in Fig 5.12. Consequently, the axial velocity in the axial centerline region is further compressed, whereas both axial and radial velocities in the tube wall region accelerate. At the oxidizer flame edge, a peak pressure is observed due to adverse flow compression generated by the combustion process, balancing the upstream flows (Fig. 5.13). Within the flame, the centerline pressure decreases to a relative minimum at the flame core. This is mainly due to maximum heat release at the flame core, contributing to a greater flow expansion in the combusting zone. Further into the fuel side of the flame edge, the rise in pressure is observed as a result of opposed

jet stagnation. Overall, dual peak pressures are distinctive characteristics of the two dimensional opposed jet diffusion flame, and significantly different from the one dimensional results where the axial pressure gradient is assumed to be constant.

5.3.2 Chemistry Aspect of Diffusion Flames

In detailed numerical simulations of the hydrogen-air diffusion flame, the chemical species undergo a series of complex dissociations and recombinations during the reaction process. Therefore, to characterize the flame-species structure, a 100% hydrogen-air flame is explored first (case I). The flame is simulated with the Yetter et al. kinetic model at 1 meter per second oxidizer input velocity, and 1.92 meters per second fuel input velocity. The tube diameter and jet separation distance are 5 millimeters.

Figure 5.14 represents the species distributions against a linearized axial temperature distribution of the flame along the axial centerline. The results illustrate the progressive dissociation/ reaction of fuel and oxidizer from edges of the flame into the inner flame. Significant concentrations still persist even in the peak flame temperature region, indicating a finite rate combustion process with fuel and oxidizer "leakages" (crossover) in this region. The nitrogen steadily decreases from the oxidizer edge to the fuel edge of the flame. The fuel side consists mainly of dissociating fuel and steam product, with no H_2O_2 or HO_2, but a trace of O and OH in the vicinity of the peak temperature. In essence, the fuel side of the flame is primarily defined by the axial momentum requirement, and the availability and diffusivity of the oxidizer in this region.

On the contrary, the oxidizer side flame displays more complexity in the species compositions. The results show that the production of H_2O_2 and HO_2 is significant only near the oxidizer edge of the flame, where H atom has diffused. Their concentrations decrease rapidly as the peak

flame temperature is approached. Concurrently, the concentrations of O, OH, and H increase with the rise in flame temperature. The peak H and H_2O coincide with peak temperature, providing an alternate way to identify the flame. Overall, the production of H can be traced as far as the oxidizer edge of the flame, indicating the oxidizer side of the flame is primarily defined by the diffusivity of the fuel.

From the kinetic viewpoint, the diffusion flame displays a wide range of temperature and different types of reaction mechanisms that control the pool of radicals. Yetter et. al. [64] reported that the high temperature regime (1200K and up) is associated with a radical pool dominated by H, O, and OH radicals, while the low temperature regime (800K and down) is dominated by HO_2 and H_2O_2. Also, they [64] reported that the intermediate temperature regime serves as a transition zone in which the concentrations of H, O, OH, HO_2, and H_2O_2 intermediates are nearly the same order of magnitude. Moreover, this regime embodies the explosion limits which separate the slow reactions (overall chain propagating) from the fast reactions (chain branching). In the high temperature regime, flame propagation is dominant and promoted through $H+O_2$, $O+H_2$, and $OH+H_2$, where H, O, and OH are favored over HO_2 radicals.

Radical termination and hence flame suppression is accomplished through $H+O_2+M$ and $HO_2+H+M->H_2+O_2+M$. Specifically, the termination reaction, $H+O_2+M$, competes with $H+O_2->OH+O$ for the H radical; whereas, the termination, $HO_2+H+M->H_2+O_2+M$ competes with $HO_2+H->2OH$ for HO_2 and H [64]. Also, the termination $HO_2+OH->H_2O+O_2$, eliminates OH as well as HO_2. Otherwise HO_2 can be used in $HO_2+H->2OH$ to generate more OH. Overall, the reactions, $O+H_2O->2OH$, and $H+O_2->OH+O$ are favored and work as chain branching mechanisms over $H+O_2+M$ which causes chain termination [64].

In the intermediate temperature range, relative to the high temperature region, the most significant difference in the underlying kinetics is the importance of the recombination reaction $H+O_2+M->HO_2+M$. As a consequence, the competing reactions $HO_2+H+M->H_2+O_2+M$ and $HO_2+H->2OH$ play a role, but of secondary importance. Also, the generation of OH in this temperature zone is nearly independent of the oxygen concentration and depends only on the temperature. This is quite different from the reaction characteristics at higher temperatures where OH depends strongly on O_2 concentration [64].

At below 1000K, the OH concentration is retained (low) near the equilibrium concentration, due to the $H+O_2+M$ recombination being favored over the branching reaction, $H+O_2->OH+O$. Since most of the O atoms produced by $H+O_2$ go on to react with H_2O to produce 2H, the reaction $H+O_2+M$ can strongly affect the OH production rate [64, 65].

5.3.3 Parametric Effects of Diffusion Flames

One advantage of the opposed jet configuration is that it is relatively easy to establish a near one dimensional flame, which in some ways simplifies the structural analysis. Previously, one-dimensional approximations showed the flame is significantly influenced by different transport properties, chemical kinetics, and inflow temperatures [7,9,11,17,28-40]. However, no known one-dimensional results are reported that either validate or apply to typical experimental tube sizes at finite separation distances used in [17], or to practical (e.g. parabolic) jet input flow profiles other than plug flow. Experimentally, the results in [17] showed that the flame extinction limit (in terms of parabolic-inflow-induced applied stress rate) is insensitive to separate distance as long as the condition of a free floating flame is satisfied. In the past, several diagnostic studies have been performed under lightly strained conditions, and compared with one dimensional

numerical data [19, 32, 34, 35]. Reference 17 contains analyses of diagnostic data over a wide range of strain rates. Nonetheless, no works provide a systematic detailed study of 2-D flame structure at lightly or highly strained conditions for different parametric input conditions such as velocity profile, variation in oxidizer composition, tube separation distance, and/or aerodynamic momentum of flows.

Therefore, the next part of this study qualitatively investigates the parametric effects on flame characteristics at relatively low input velocity conditions (Table 5.1). The information developed can be used as a reference to, and in validation of, various measurement techniques.

The first simulation (case II) was conducted to study the flame characteristics at different oxidizer input velocities, prescribed as 3, 4, and 5 meters per second. The fuel velocities are fully balanced using a one dimensional momentum equation, and the separation distance is twice the tube diameter.

The resultant temperature isocontour and velocity vector plots for case II, presented in Fig. 5.15, display a thin and slender flame on the oxidizer (left) side relative to the stagnation plane. The flame is controlled largely by the effectiveness of the mixing process, and the chemical reaction rates are significant only in a thin region where the mixing is significant. Further down-stream, the flame curves to the oxidizer side causing an asymmetry, due to the high diffusivity and viscosity in hydrogen, the abundance of excess fuel, and the density difference of the two jets. The maximum temperature appears at a diameter distance of one jet downstream from the axis centerline, indicating that the region still has an abundance of unburned oxygen and fuel.

Structurally, the formations of major species distributions in case II (Fig. 5.16) generally coincide with isocontours of temperature distribution in Fig. 5.15. The H and H_2O have their peaks at the axis of symmetry on the oxidizer side of the flow stagnation point (from Fig. 5.17).

Their peaks are slightly off from the temperature peak (from Fig. 5.18). However, the O and OH attain peaks not at the axial centerline, but at one diameter distance from the axial centerline in the downstream. In essence, the flame has highly two-dimensional characteristics.

As the input velocity increases in case II, the peak of the temperature isocontour in Fig. 5.18 decreases, resulting in a thinner flame closer to the stagnation plane. At the axial centerline, the higher input velocity decreases the peak H_2O and OH mole fractional distributions (Fig. 5.17), and increases O and H, indicating the chemical process within the flame is more severely limited by the aerodynamic strains. In general, a thinner flame, with a closer displacement of the species mole fractional distributions toward the stagnation point, is a typical characteristic induced by high input flows in opposed jet diffusion flames (Figs. 5.16-5.18).

The second simulation (Case III) differs from Case II by the tube separation distance, prescribed as three times the tube diameter. The fuel velocities are fully (Case III) and partially (80% for Case IV) balanced using the one dimensional momentum equation. Figure 5.19 represents the temperature and species mole fraction distributions at the axis centerline as a function of the atomic hydrogen mixture fraction for cases II, III, and IV. For the fully balanced flows (Case III), a larger separation distance reduces the centerline oxidizer and fuel flow rates to the flame, due to relatively larger flow divergence, resulting in a smaller centerline peak H_2O mole fractional distribution. Although the smaller oxidizer flow rate to the flame produces a smaller centerline air-side maximum axial strain rate, it causes a larger peak OH mole fractional distribution at the axial centerline. Thus it appears that the larger separation distance (Case III) results in a higher axial centerline peak flame temperature due to smaller convective heat loss to the flowfield. Therefore, a higher peak O is seen at the centerline (Figs. 5.21 and 5.22). Overall, the larger separation distance reduces the convective transport of oxidizer against the convective/diffusive transport of

fuel to the combustion zone, resulting in a thicker flame. Consequently, the peak H and H_2O occur closer to the stagnation point, whereas the peak O, OH and temperature are positioned further into the oxidizer side.

The partially balanced flows (Case IV) are characterized in Fig. 5.19 by smaller centerline peak OH and flame temperature distributions than the balanced flame with the same separation distance (Case III), due to relatively smaller fuel flow rate to the flame zone. Nonetheless, the partially balanced flame results in higher centerline peak H_2O and lower peak O. This is probably due to a relatively larger fuel residence time (smaller centerline fuelside maximum axial strain rate), where the effect of fuelside aerodynamic strain on combustion is less restrictive than for the flame with fully balanced flow (Figs. 5.19-5.22). The partially balanced flows unanimously increase the centerline displacement distances from the stagnation point for all major species and temperature, shifting a flame closer to the oxidizer side. Comparatively, the momentum variation exerts much greater influence on flame characteristics than the separation distance variation does.

Finally, a set of third simulations is performed, which differ from Case II by the oxidizer composition. The major species mole fraction distributions along the axial centerline, relative to the stagnation point, are shown in Fig. 5.23. The oxygen-lean oxidizer flame (Case VI) is thinner with smaller peak species mole fractions (and temperature) than those of Case II, due to smaller oxygen flow rate to the flame zone. Alternatively, the oxygen-rich oxidizer flame (Case VII) is thicker with higher peak species (and temperature).

As the input velocity increases, the oxygen-lean flows cause the flames to deviate considerably from the Case II flames, with respect to flame thickness, axial centerline peak major species, and displacement distance of O and OH relative to the stagnation point. Yet, the differences in strain rate and displacement distances of H and H_2O are quite small (Figs. 5.24 and 5.25).

Alternatively, the higher input velocity causes oxygen-rich induced flames to converge closer to that of Case II with respect to centerline airside maximum strain rate, peak temperature, and peak radical species. Overall, the input oxygen variation affects flame characteristics, but its effects are relatively smaller than for the flame with a momentum variation.

Lastly, the flame responding to water vitiated oxidizer (Case V) is investigated. The results shown in Fig. 5.23 indicate that the vitiated oxidizer enhances the combustion process within a flame, through improvement in the collisional efficiency of H_2O as a third body participant. As a result, the flame has a higher centerline peak temperature and a smaller centerline peak H and O than that of Case II. However, the flame has higher centerline peak OH due to the dissociation of (higher concentration) H_2O than that of Case II. Overall, the water vitiated oxidizer exerts a significant influence on the flame characteristics in terms of heat release and steam production.

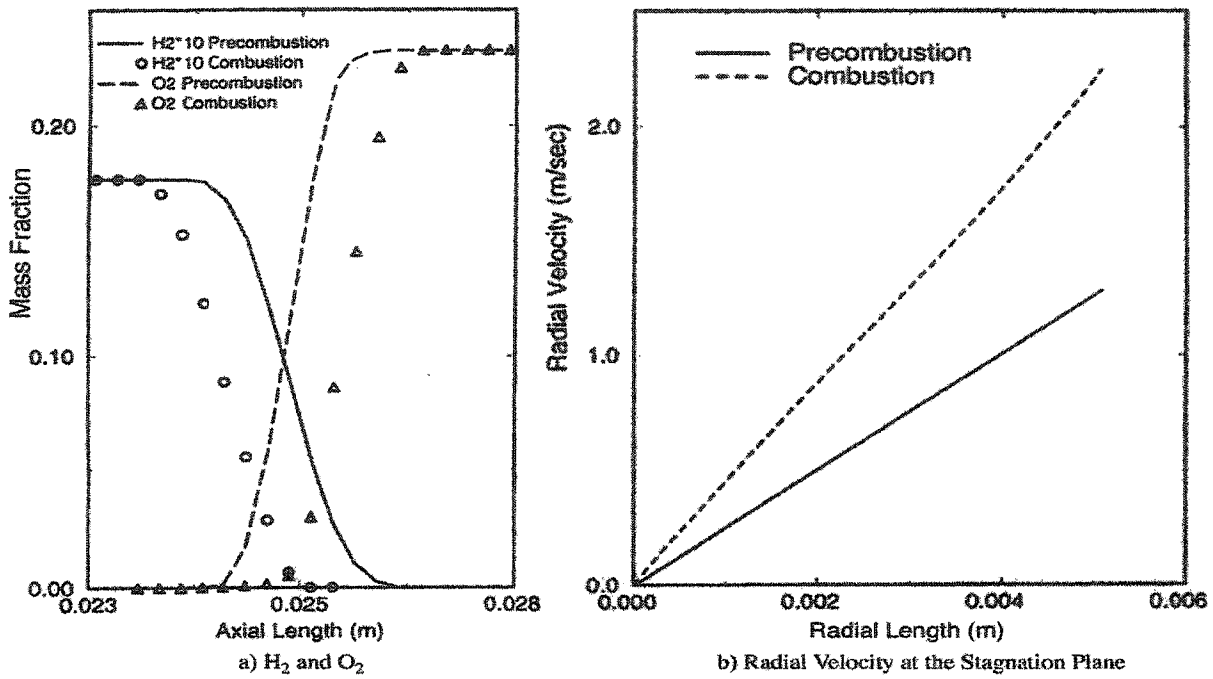

Fig. 5.11 Comparative difference between precombustion and combustion (plug inflow induced) flows using 20% (mole) hydrogen-air system at oxidizer input velocity of 1.6 meters per second. Left plot represents centerline fuel and oxidizer distributions. Right plot represents radial velocity at stagnation plane.

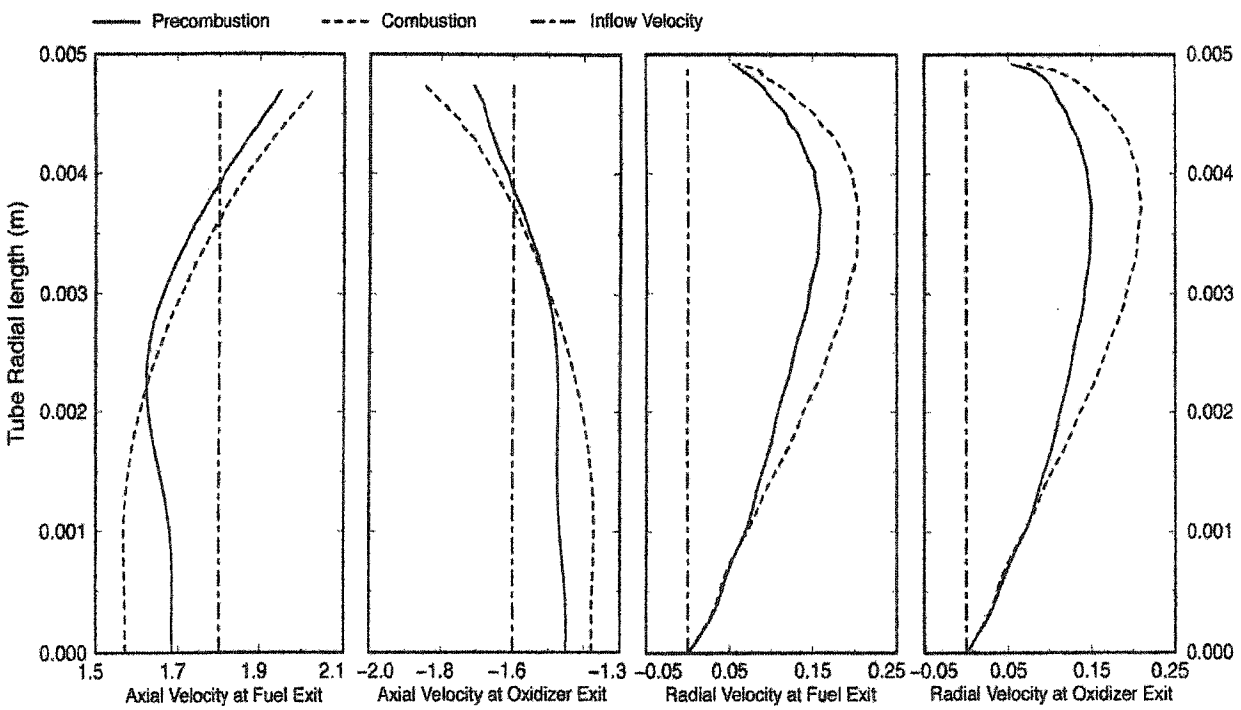

Fig. 5.12 Comparative difference in plug and parabolic inflow induced exit velocity profiles at precombustion and combustion states using 20% hydrogen-air system at oxidizer input velocity of 1.6 meters per second.

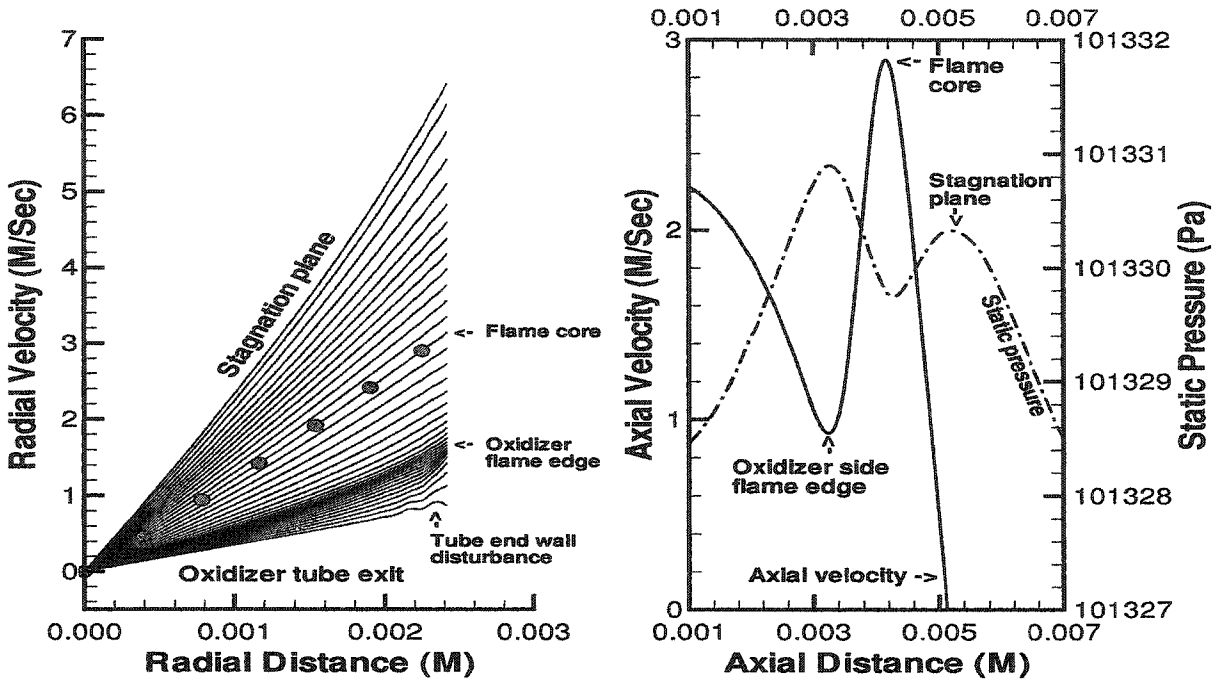

Fig. 5.13 Characteristics of plug inflow induced 100% hydrogen-air opposed jet diffusion flame at oxidizer input velocity of 2.32 meters per second. Left plot represents radial velocity profiles in oxidizer side. Right plot represents centerline axial velocity and static pressure, with oxidizer o left side.

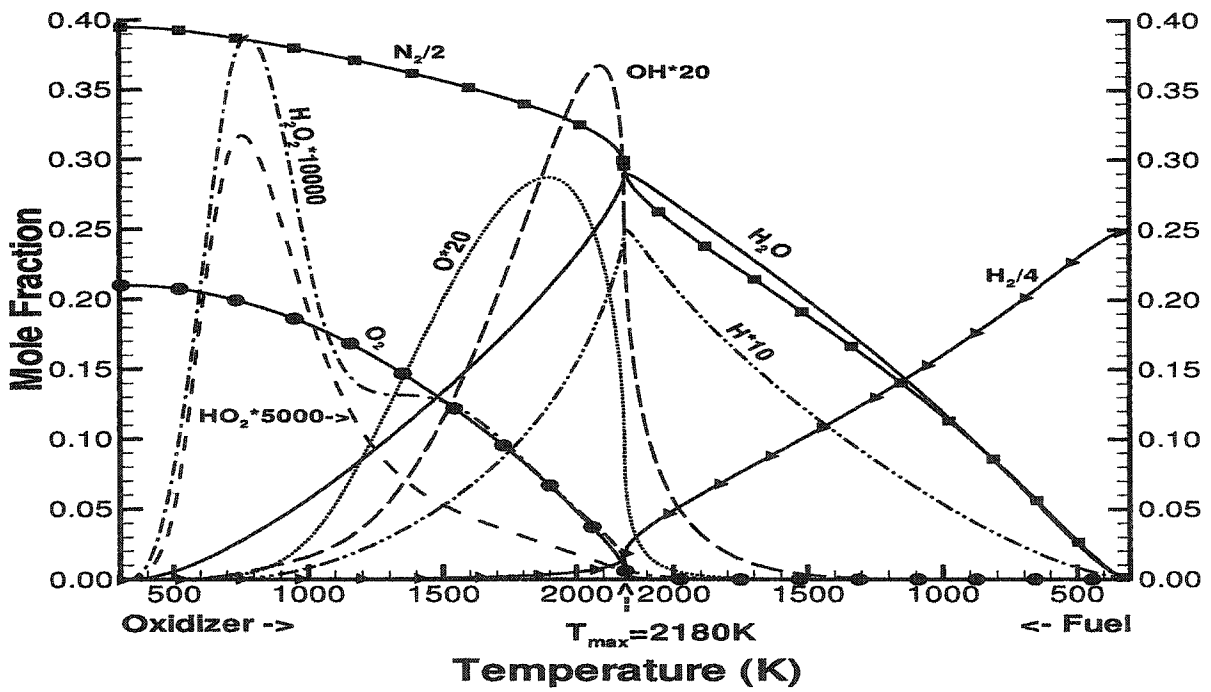

Fig 5.14 Centerline species mole fractional distributions within a plug inflow induced diffusion flame, at oxidizer input velocity of 1 meters per second on the left side.

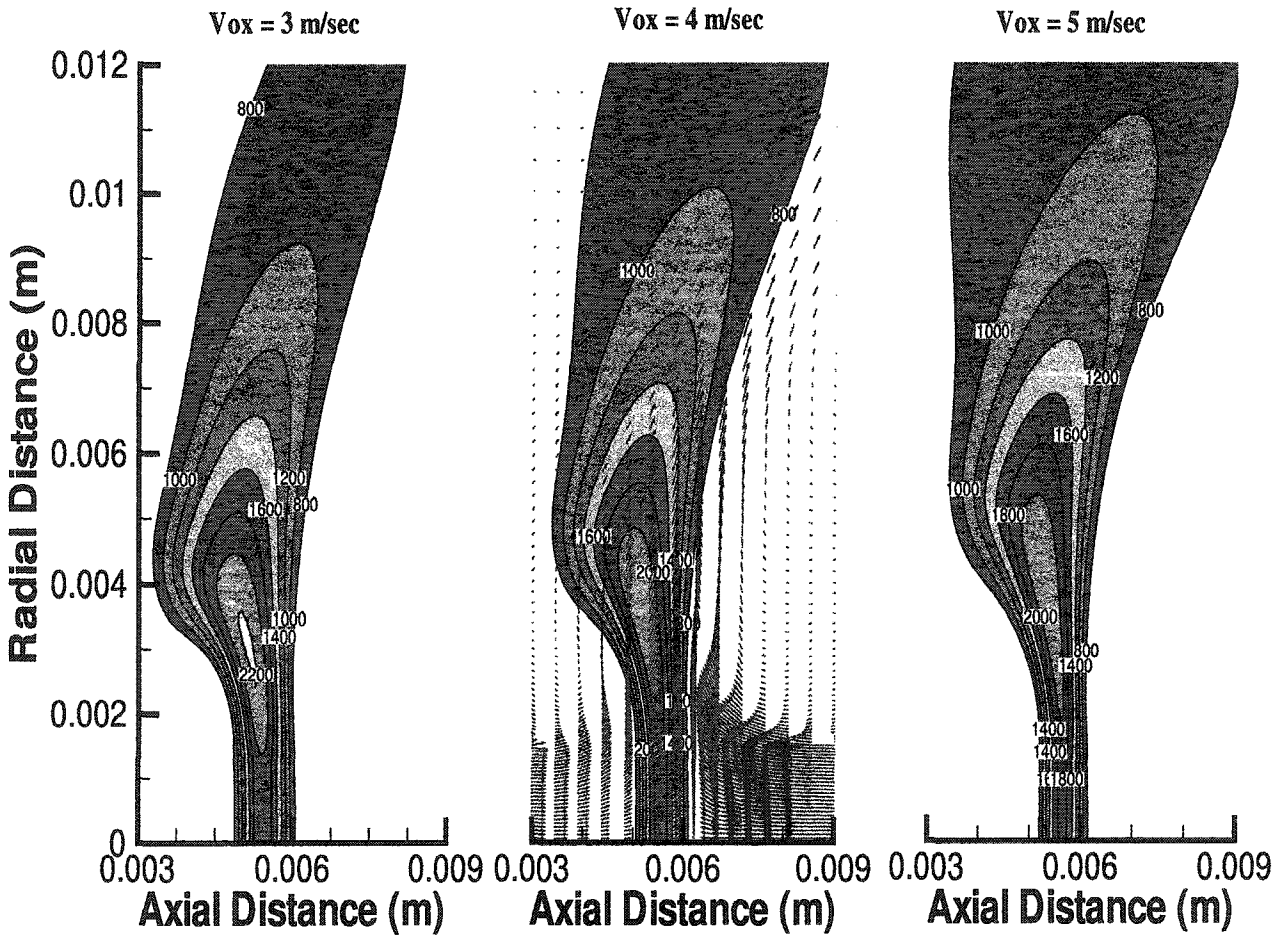

Fig. 5.15 Case II temperature isocontours and velocity vectors of plug inflow induced 100% hydrogen-air diffusion flames at lightly strained condition. Oxidizer is on left side.

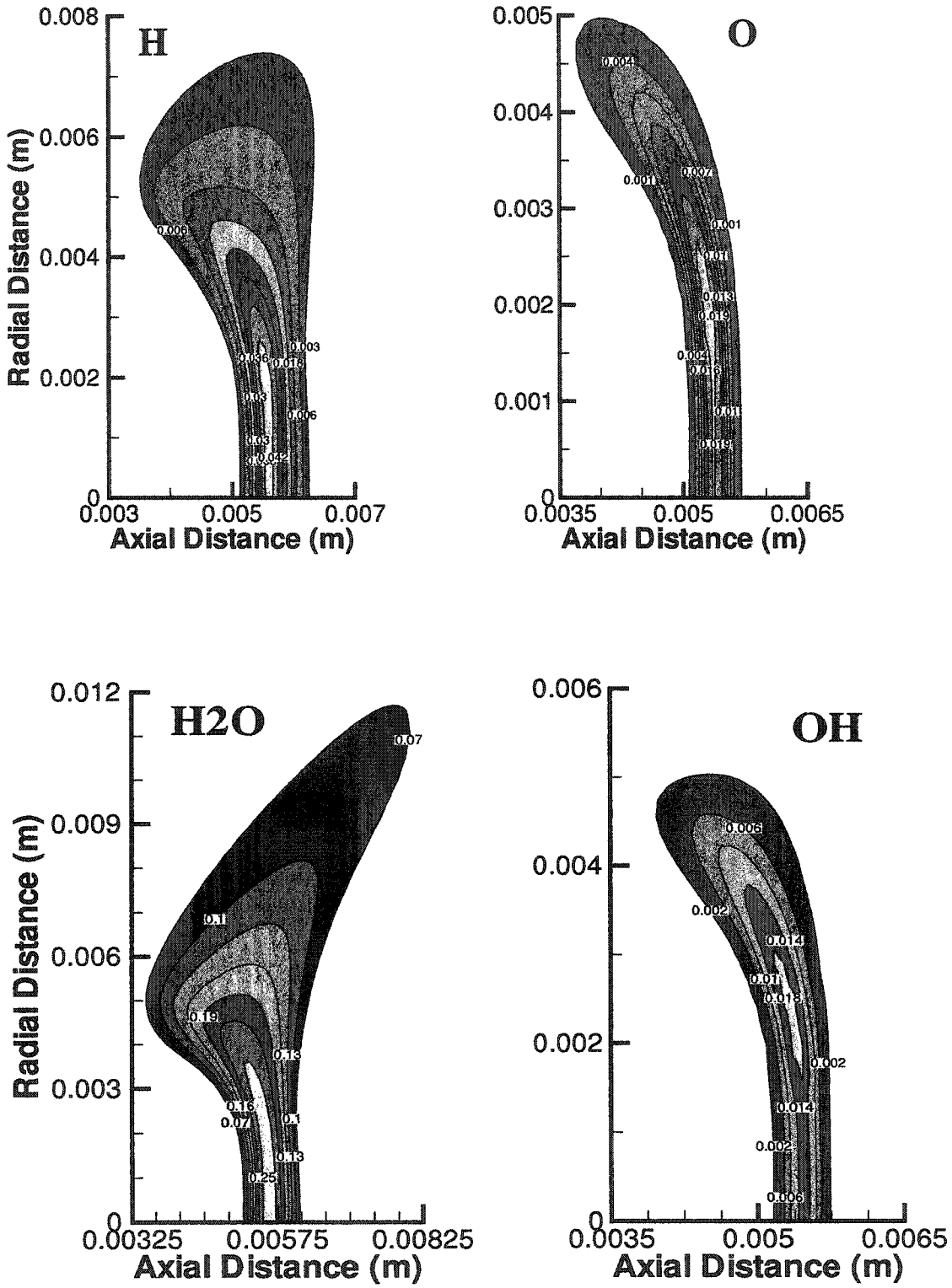

Fig 5.16 Case II species mole fractional isocontours of plug inflow induced 100% hydrogen-air diffusion flame at oxidizer velocity of 3 meters per second. Oxidizer is on left side.

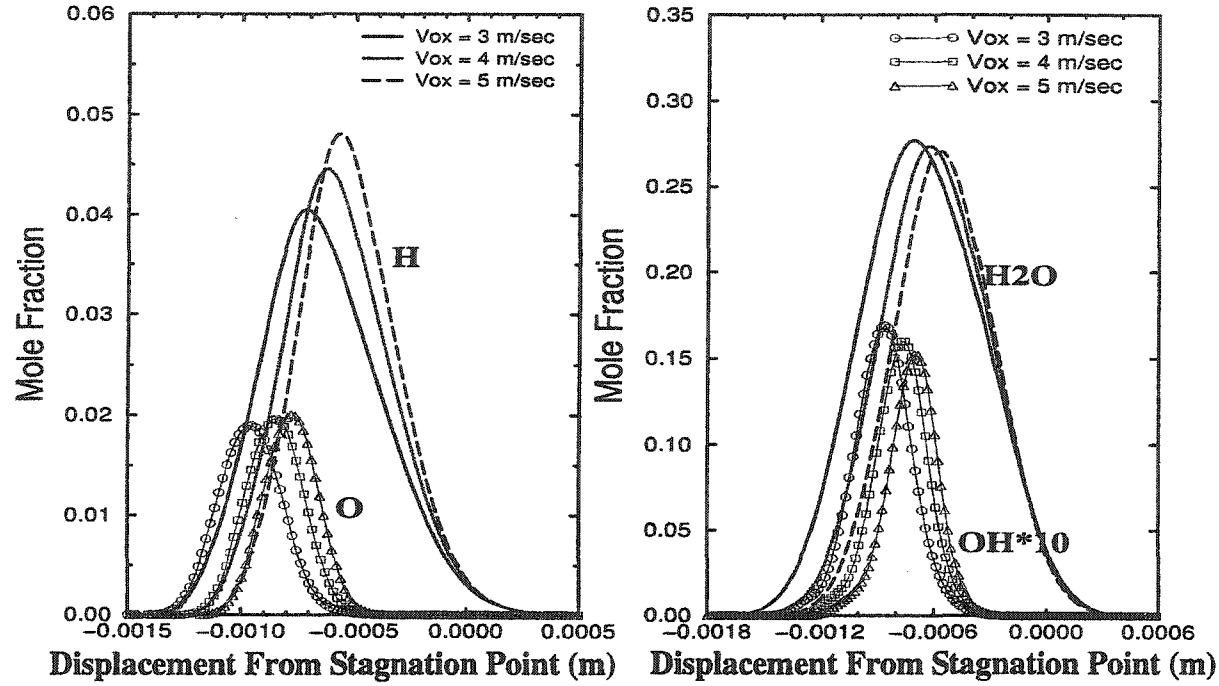

Fig. 5. 17Centerline mole fractional species distributions of plug inflow induced 100% hydrogen-air diffusion flames (Case II). Oxidizer is on left side.

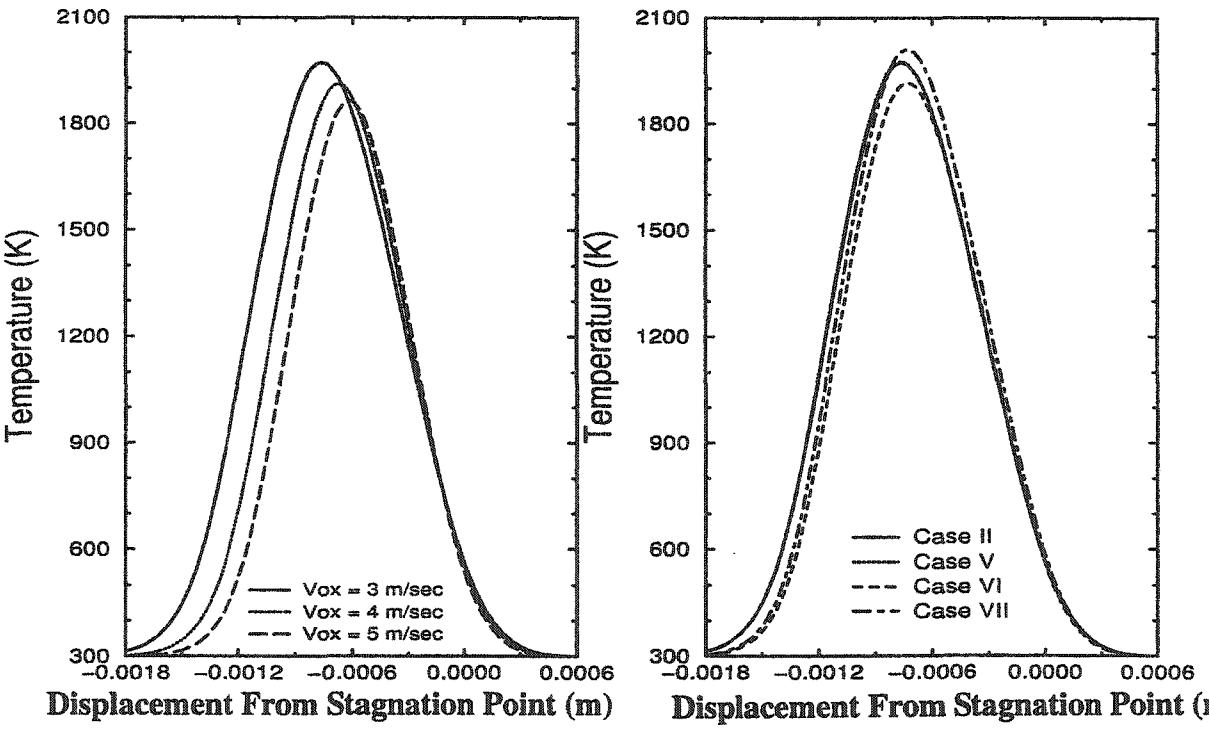

Fig. 5.18 Centerline temperature distributions of plug inflow induced 100% hydrogen-air diffusion flames. Left plot is for case II. Right plot represents temperature distributions at oxidizer input velocity of 3 meters per second for Cases II, V, VI, and VII. Oxidizer is on left side.

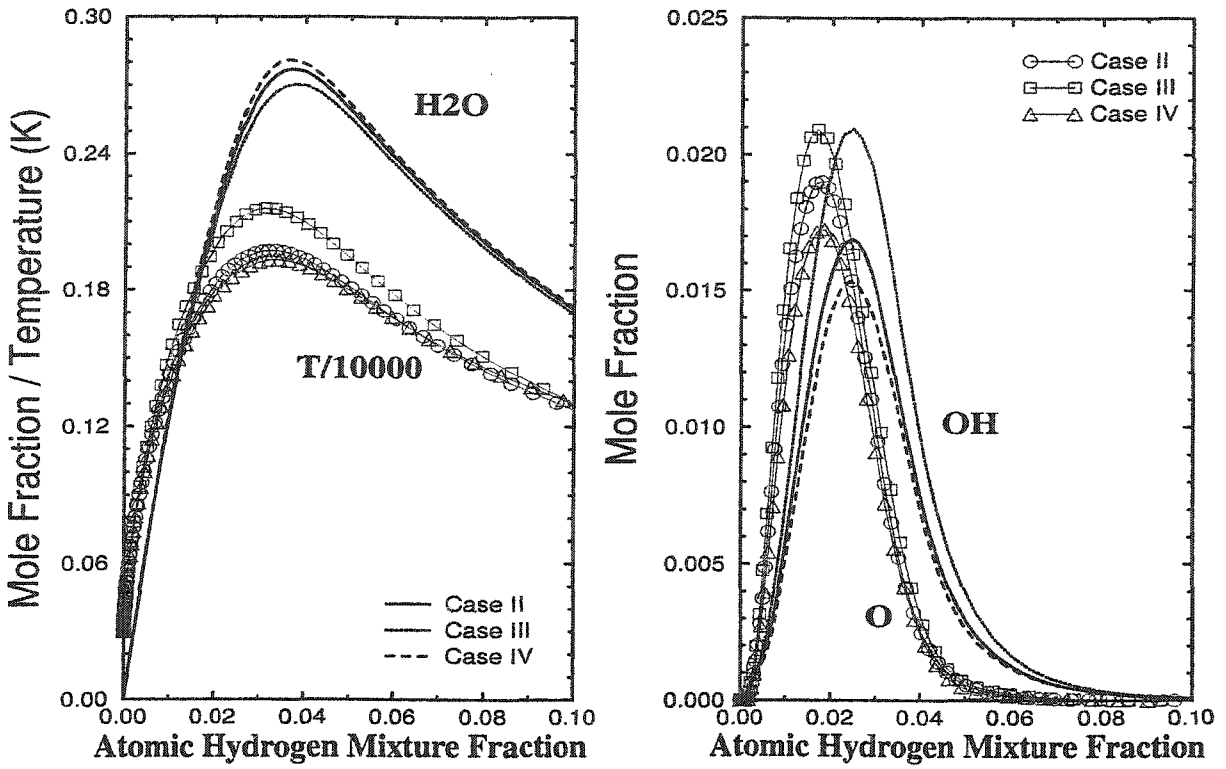

Fig. 5.19 Centerline temperature and mole fractional species distributions of plug inflow induced 100% hydrogen-air diffusion flames at different degrees of flow momentum for Cases II, III, and IV (oxidizer input velocity of 3 meters per second).

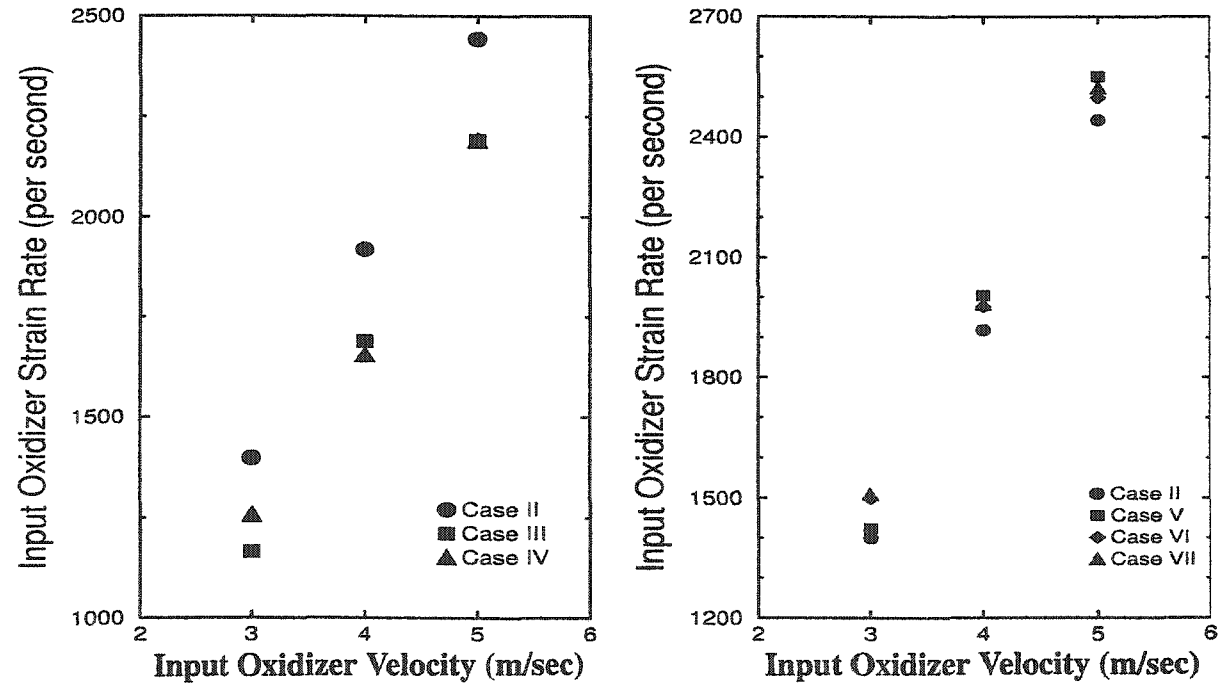

Fig. 5.20 Oxidizer side centerline maximum axial strain rates of plug inflow induced hydrogen-air counterflow diffusion flames at lightly strained conditions.

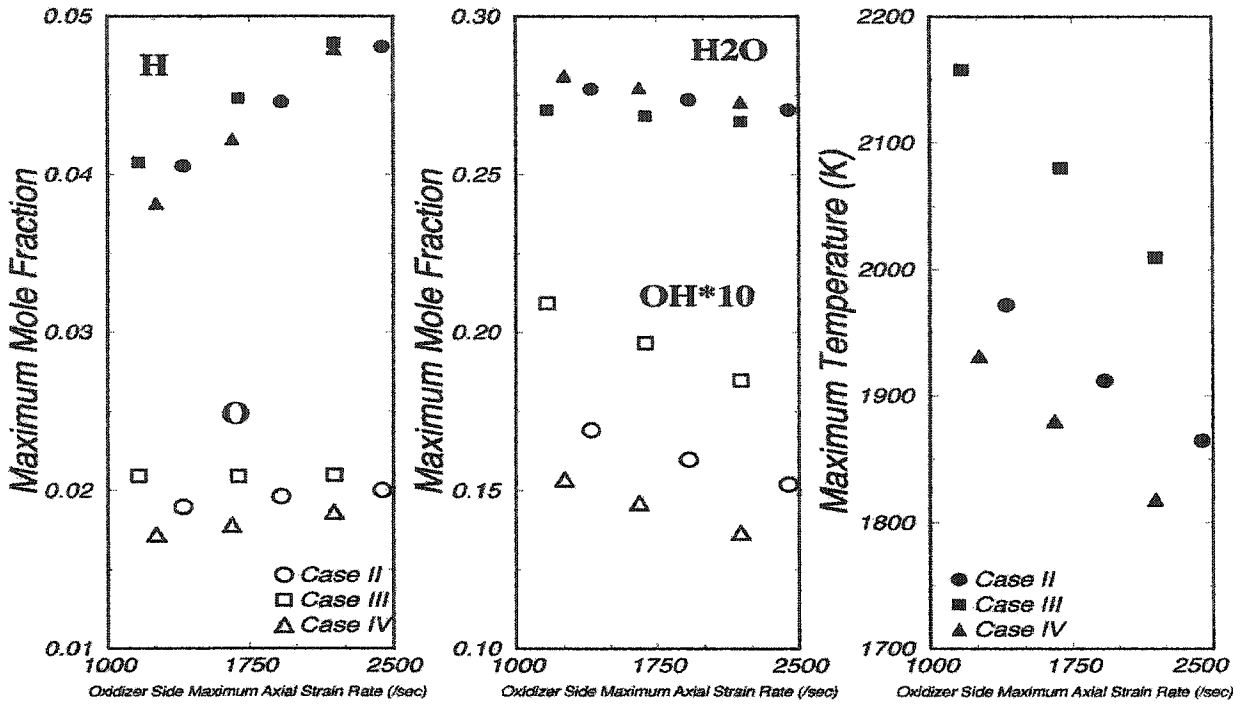

Fig. 5.21 Centerline peak temperature and mole fractional species distributions plotted against oxidizer side centerline maximum axial strain rates for plug inflow induced 100% hydrogen-air diffusion flames (Cases II, III, and IV).

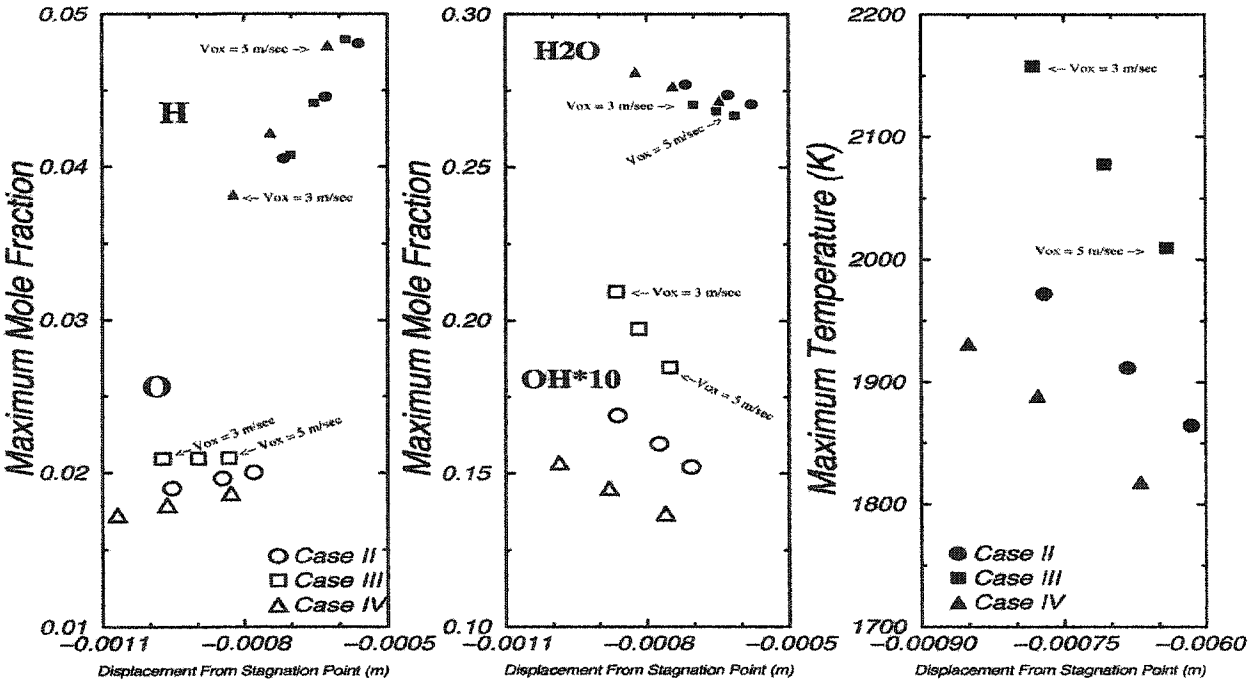

Fig. 5.22 Centerline peak temperature and mole fractional species distributions plotted against displacement from stagnation point for plug inflow induced 100% hydrogen-air diffusion flames (Cases II, III, and IV).

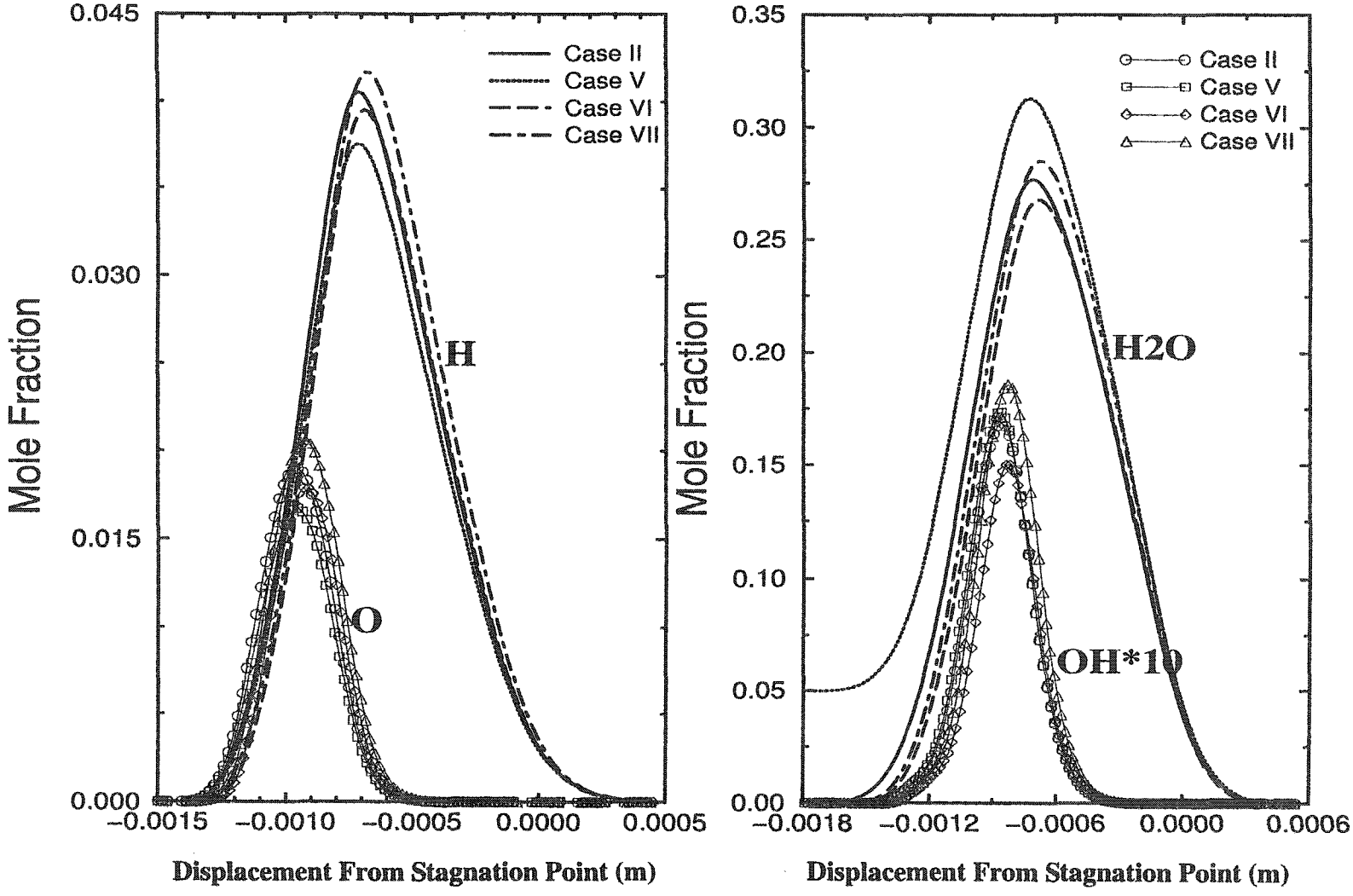

Fig. 5.23 Centerline mole fractional species distributions of plug inflow induced 100% hydrogen-air diffusion flames (Cases II, V, VI, and VII).

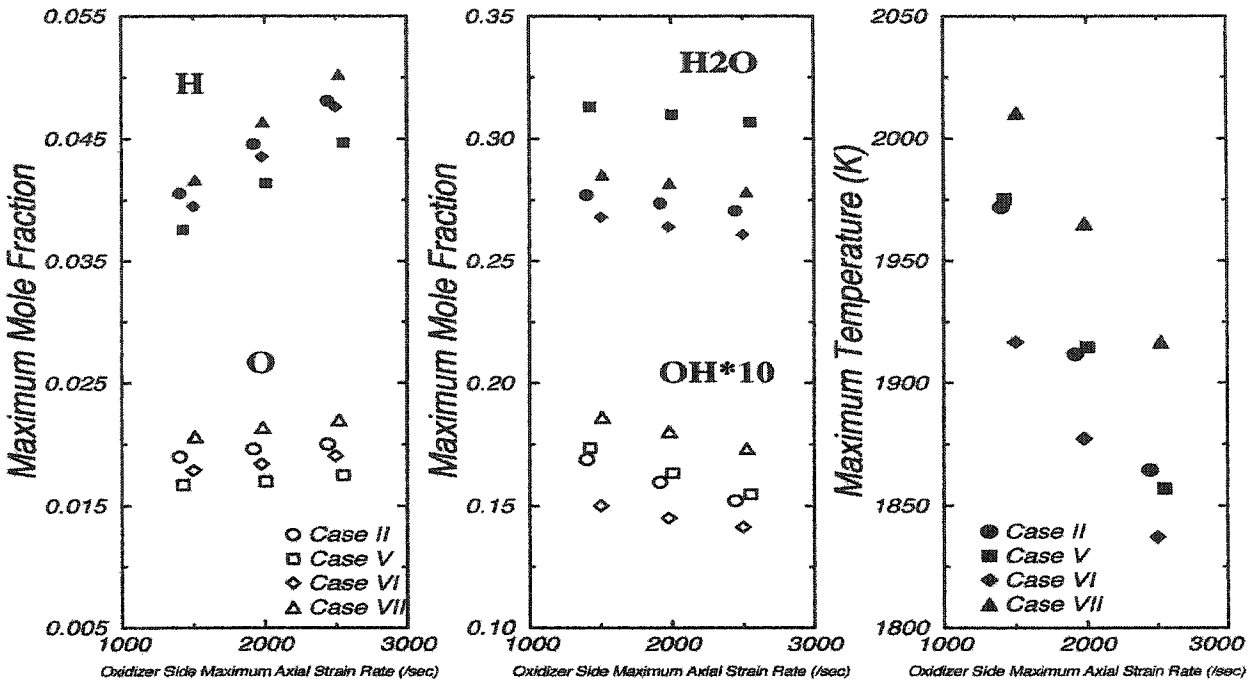

Fig. 5.24 Centerline peak temperature and mole fractional species distributions plotted against oxidizer side centerline maximum axial strain rates for plug inflow induced 100% hydrogen-air diffusion flames (Cases II, V, VI, and VII).

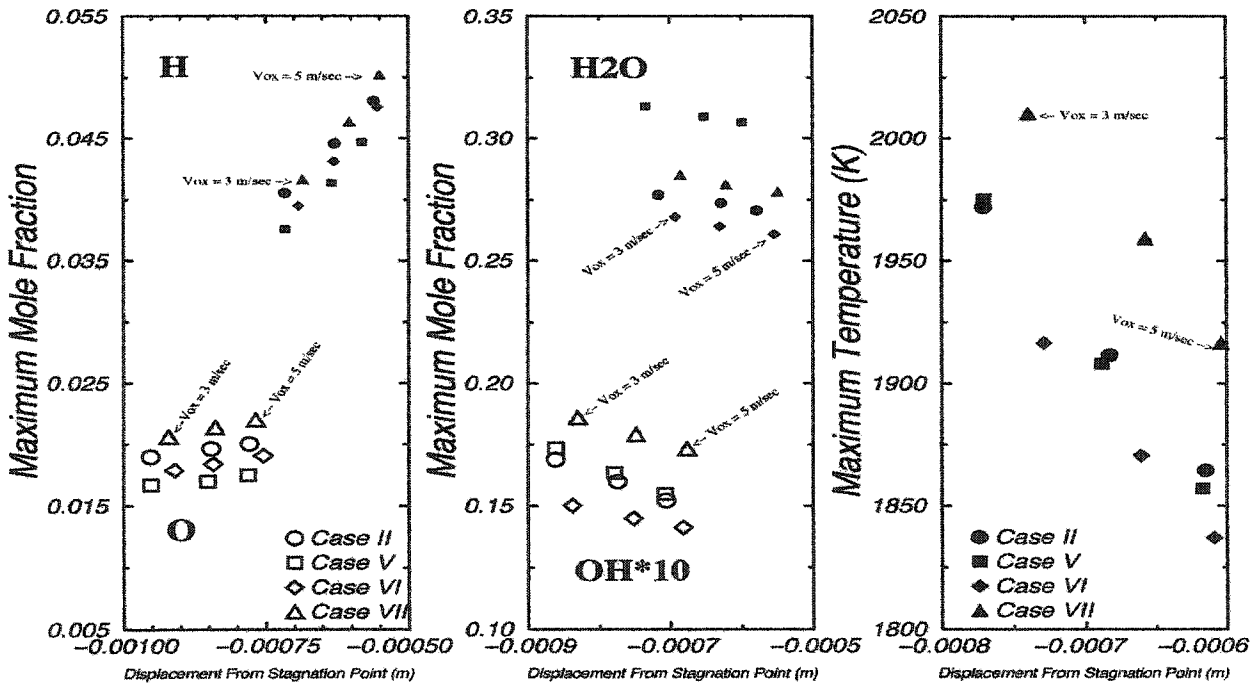

Fig. 5.25 Centerline peak temperature and mole fractional species distributions plotted against displacement from stagnation point for plug inflow induced 100% hydrogen-air diffusion flames (Cases II, V, VI, and VII).

5.4 Diffusion Flames at Extinction Limit

Hydrogen has a very high diffusion rate and a low flammability limit. As a consequence, the extinction of a pure hydrogen-air laminar counterflow diffusion flame can only be achieved with extremely high strain rate using small diameter tube/nozzles. Because of possibly significant multidimensional effects associating with small opposed jet dimensions [44, 45], the two dimensional numerical technique is used here to investigate the details of flame extinction. For the analysis, the flame is simulated with a 3 millimeter tube diameter at a separation distance of 6 millimeters. The oxidizer is air consisting of 21% O_2 and 79% N_2 in volume, and the fuel is H_2. In numerical simulations, the oxidizer velocity is started from low and incrementally increased to achieve flame extinction. Especially at or near the extinction limit, the input oxidizer velocity is increased incrementally with 0.1 meters per second. The fuel velocity is calculated, based on the one-dimensional approximation of the momentum equation. For maintaining flame stability, nitrogen coflow gas is utilized with a uniform input velocity of 0.1 meters per second.

The first part of the investigation characterizes the various strain rates near the extinction limit, using both the Yetter et al. and Jachimowski models for plug flow inputs. The results shown in Figs. 5.27 and 5.28 indicate that the centerline airside Maximum Local axial Strain Rate (MLSR), and the centerline radial strain rates at the flame core and stagnation point, vary linearly with oxidizer input velocity. This indicates that the radial stretching of a flame is linearly related with the aerodynamics of flow. More importantly, the strain of the flame can be estimated globally using the applied stress rate, U/D, as proposed by Pellett et al. [17].

Each of calculated strain rates for the different chemistry models collapse onto a single line in Fig. 5.27. Thus, the airside maximum axial strain rates are non-dimensionalized and represented by a constant correlating factor of 1.69, through dividing the rate by a global applied stress

rate (ASR), U_{ox}/D. Similarly, correlating factors for the centerline radial strain rates at the flame core and stagnation point are 1.55 and 2.96, respectively. In particular, the radial factor at the stagnation point is 2.57 times greater than that found for nonreacting flows (1.15) in section 4-1, page 55. This indicates that the heat release due to chemical reactions is dominant in radial stretching at the stagnation point in the presence of flame, although flame extinction is actually achieved through aerodynamic strain in the flame core region. Comparatively, the airside maximum axial strain rate is 1.1 times larger than the radial strain rate at the flame core, departing significantly from the typical value associated with the one-dimensional approximation (potential flow assumption) that the maximum axial rate is twice that of the radial rate. Moreover, the radial strain rate in the flame core is 1.91 times larger at the stagnation point than the maximum axial strain rate, illustrating an exceptional expansion of flow at the stagnation point.

The second part of the investigation analyzes the overall behavior of species and temperature distributions at the extinction limit, using plug flow inputs. At the axial centerline, the progressive straining of a flame causes the peak temperature and all reactive and product species concentrations to decrease nonlinearly, in increasingly steep arcs as the input velocity increases (Figs. 5.29-5.31). In particular, in the vicinity of the extinction limit, drastic decreases are seen, indicating the rate of combustion is severely influenced by aerodynamic strain. Comparatively, the peak mole fractional of O, OH, and H decrease to levels that are approximately equivalent at the extinction limit, showing distinctively different characteristics than species at the lightly strain condition. The extinction is dominated and governed mainly by atomic hydrogen through $H + O_2 <-> OH + O$, where this chain branching and endothermic reaction slows (bottle necks) the oxidation causing severe deficiencies in radical species like OH and O [40].

The Jachimowski kinetic model predicts flame extinction at the centerline peak temperature of 1306K, whereas the Yetter et al. model predicts a slightly higher extinction temperature at 1337K, for plug flow inputs. Overall, these temperature predictions are close to an authoritative one dimensional result [9] where the extinction temperature is 1332K. Qualitatively, the Jachimowksi model also shows "earlier" reductions in all peak species, achieving flame extinction at a smaller axial strain rate than the Yetter et al. model. These flame extinctions occur at a MLSR of 13808 per second for the Jachimowski model, which is 12.7% lower than the MLSR of 15808 per second for the Yetter et al. model. Both of these rates are comparatively smaller than two independently calculated one-dimensional results [9, 32] for MLSR, which average about 16200 per second.

Nonetheless, the largest difference between two dimensional plug inflows and one dimensional potential flow simulations of flame extinction appears in the centerline radial strain rate. The one dimensional approximation (theory) in [9, 32, 35] predicted the centerline radial strain rate at the flame extinction to be about 8100 per second, significantly different from the two dimensional results. The Yetter et al. kinetic model yields two dimensional *centerline* radial strain rates of 27692 per second at the stagnation point and 14431 per second at the flame core. Whereas, the Jachimowski model yields *centerline* radial strain rates at the stagnation point and flame core of 24037 and 13198 per seconds, respectively (Tables 5.2 and 5.3).

The uniqueness of a flame core structure observed with plug inflow boundaries is threefold. First, a temperature maximum exists on the centerline. Second, a minimum temperature point is located approximately one radius downstream along the radial flame core from the axial centerline (Figs. 5.26 and 5.32). Third, a higher maximum temperature occurs beyond three radii. The minimum radial flame core temperature is caused by a higher local axial impingement of oxi-

dizer and fuel flows, with higher strain rates. The observation is made that the local extinction of a flame initiates and propagates from the minimum point. However, the local maximum temperature on the axial centerline dominates the overall flame extinction. At the minimum point, the peak axial species decrease more rapidly than at the centerline, as the input velocity approaches the extinction limit. Upon the extinction of central flame, the maximum airside axial strain rates are 19230 and 16733 per second, near unit radius, for the Yetter et al. and Jachimowski models, respectively, where the axial strain rates are approximately 21% larger than at the centerline (Tables 5.6 and 5.7). Overall, the rate difference over different chemistry models at the minimum temperature point is relatively small at about 15%, compared to 16% in the rate difference at the axial centerline.

The temperature difference between the flame core on the axial centerline and the minimum point near unit radius reflects a robust flame dominated by centerline behavior. The temperature difference is small when the flame is modestly strained. However, the difference increases considerably as the flame approaches the extinction limit, which indicates the flame's strength continues to stem from the centerline. The minimum temperatures at the inflicting point (near unit radius) are 1262K and 1241K for the Yetter et al. and Jachimowski models, respectively (Figs. 5.33 and 5.34). The flame core temperature differences between the centerline and inflicting points reach 75K and 65K for the Yetter et al. and Jachimowski models, respectively. Note the temperature difference between the two chemistry models at the minimum point is 21K, compared to 31K at the axial centerline. Considering the two chemistry models display different flame structures for plug inflows at lightly and modestly strained conditions (see Sec. 5.2), these models predict fairly close flame extinction temperatures on axis in the flame core, i.e., 1337K (Yetter et al.) versus 1306K (Jachimowski).

Finally, the third part of the simulations is studies the effects of artificial numerical dissipation on overall extinction characteristics of a diffusion flame. For this study, two distinctive approaches in implementing artificial dissipations in a numerical model are considered. In the preferential artificial dissipation approach, a fourth order term is applied only to the "flow set" of governing equations, whereas a second order term is applied exclusively to the "species set". Comparably, in using non-preferential artificial dissipation, both second and fourth order terms are applied to both the flow and species sets of the governing equations, representing a more probable condition often seen in the numerical problems with a fully coupled set of the governing equations.

For the low strain rate flame, both preferential and non-preferential artificial dissipations show no visible differentiation in velocity and species distributions, indicating their overall effects on the characteristics of a diffusion flame are negligible (Fig. 5.35). However, near flame extinction, non-preferential artificial dissipation decreases the peak temperature and all major species more rapidly with oxidizer input velocity (and MLSR), resulting in an earlier extinction of the flame (Figs. 5.28-5.31, 5.36).

With the Jachimowski model, the non-preferential dissipation flame experiences extinction at a MLSR and temperature of 10527 per second and 1268K, respectively (Tables 5.8 and 5.9). Whereas, with the Yetter et al. model, extinction occurred at a MLSR and temperature of 11637 per second and 1340K. Relatively, the Jachimowski model predicts smaller peaks in OH, H_2O, and O at extinction than the Yetter et al. model. Comparatively, the non-preferentially dissipated flame results in the smallest axial peak H and H_2O at the extinction. Whereas, the preferentially dissipated flame predicts the smallest axial peak O and OH at the extinction. Similar to the Fig. 5.27 results, the centerline airside maximum axial strain rates (MLSR) of non-preferentially

dissipated flames are approximately independent of the chemistry models Fig. 5.28, although their nondimensional correlating factor is smaller (1.57) than that for the preferentially dissipated flames (1.70).

As stated in section 5.1, the dissipation terms are often seen as "extras" to the discretized governing equations. Accordingly, dissipations are chosen in a manner that their addition to the set of discretized governing equations satisfies a minimum stability in solutions, yet their contribution to the system of equations must be smaller than overall truncation errors. In this reason, the method of preferential artificial dissipation is strongly preferred and chosen for obtaining the results.

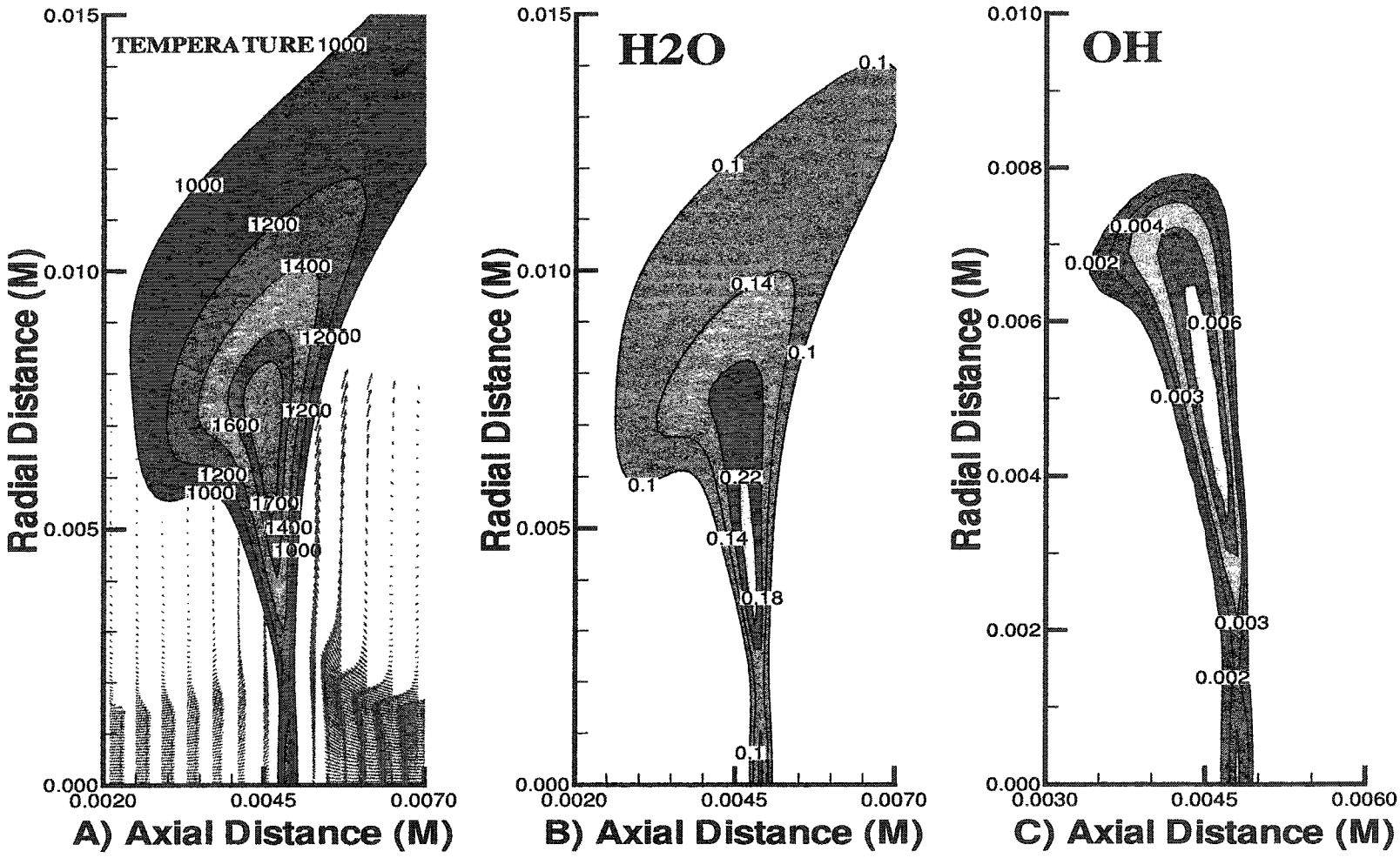

Fig. 5.26 Temperature and species mole fractional isocontours and velocity vector of plug inflow induced 100% hydrogen-air diffusion flame near extinction (with Yetter et al. model). Nozzle radius is 1.5 millimeter.

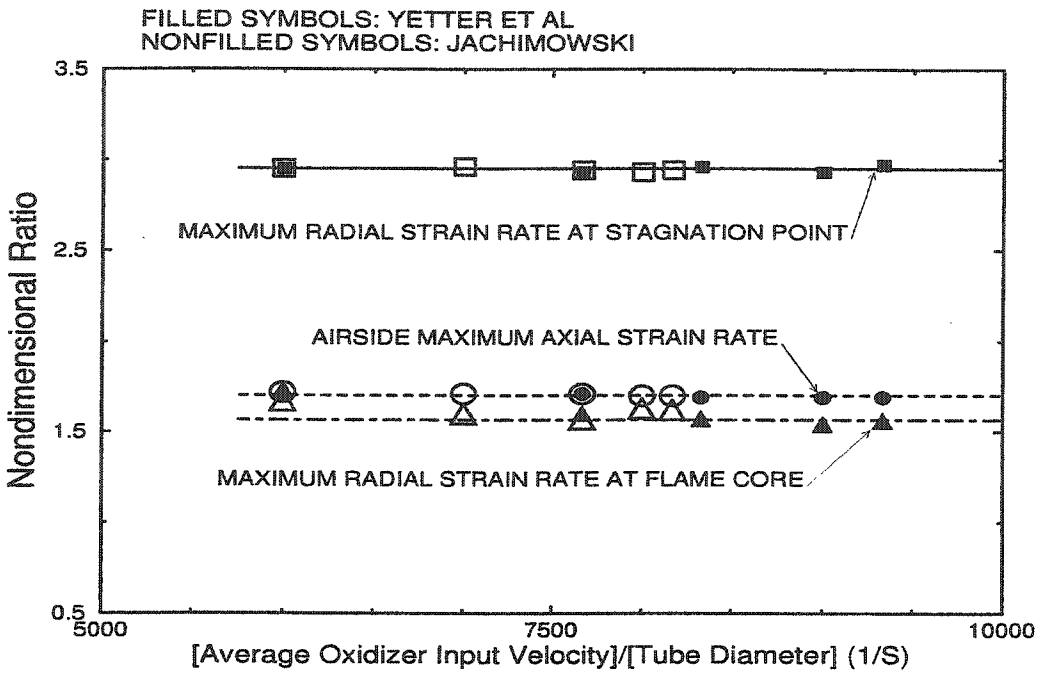

Fig. 5.27 Correlated distributions of various **centerline strain rates** for **plug inflow** induced 100% hydrogen-air counterflow diffusion flames before extinction (nondimensional ratio normalized using global applied stress rate used as abscissa).

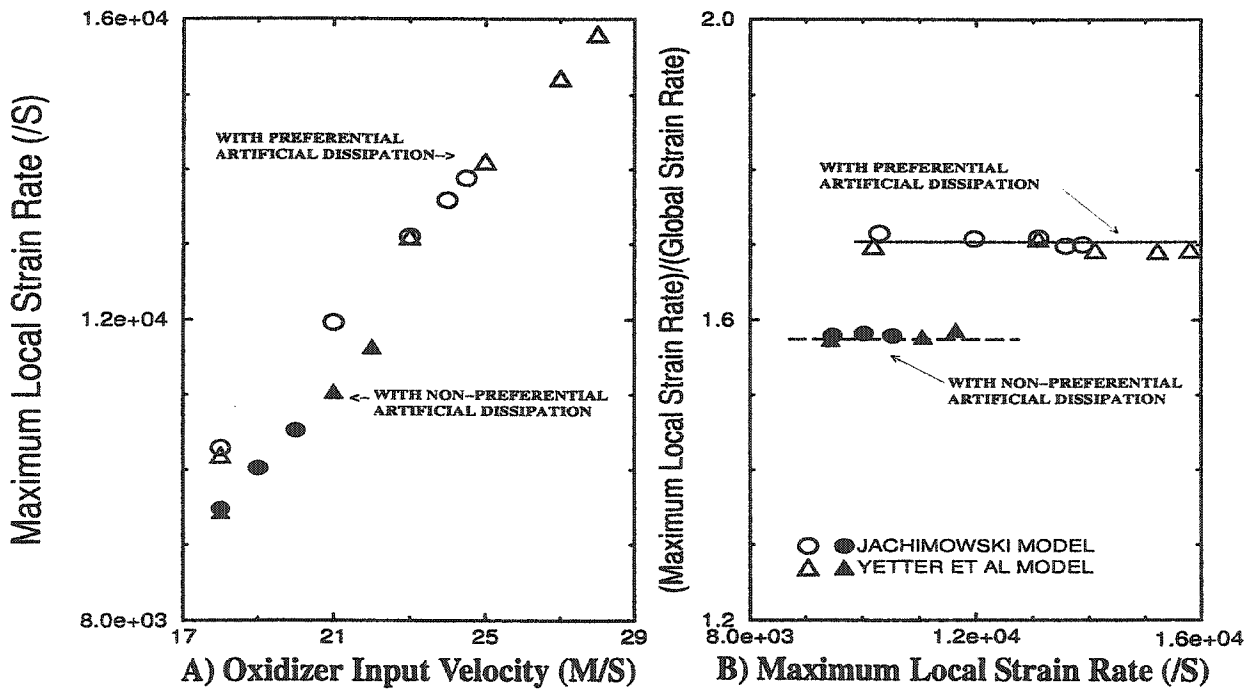

Fig. 5.28 Distributions of oxidizer side maximum axial strain rates (MLSR) for **plug inflow** induced 100% hydrogen-air counterflow diffusion flames at different chemistry models (left) and dissipative coefficients (right).

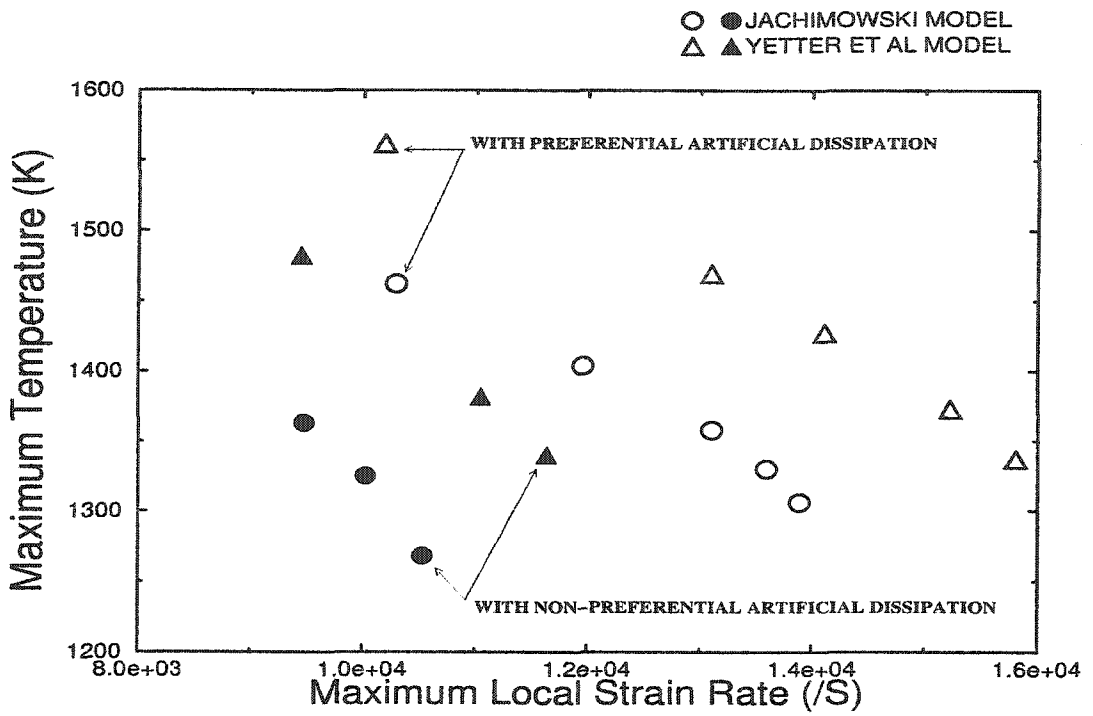

Fig. 5.29 **Centerline temperature** distributions of **plug inflow** induced 100% hydrogen-air diffusion flames for different chemistry models and dissipative coefficients before extinction.

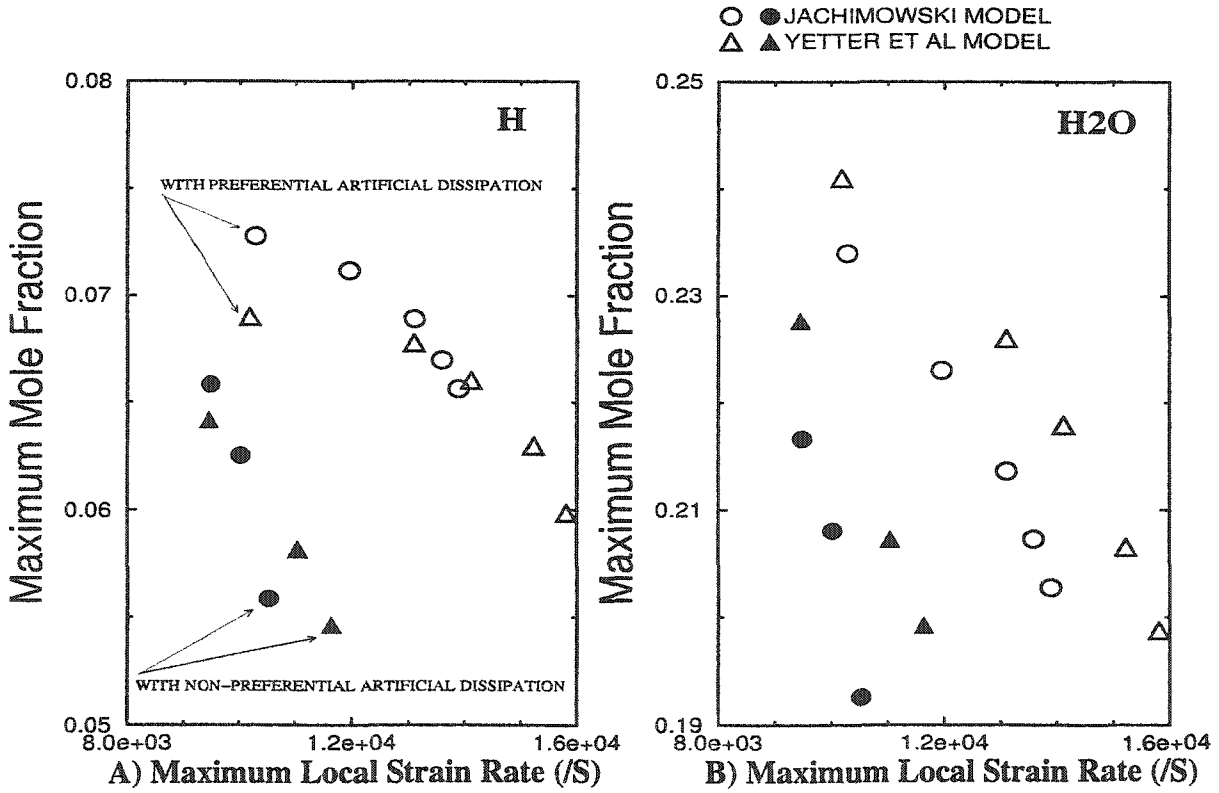

Fig. 5.30 **Centerline peak species** distributions of **plug inflow** induced 100% hydrogen-air diffusion flames for different chemistry models before extinction.

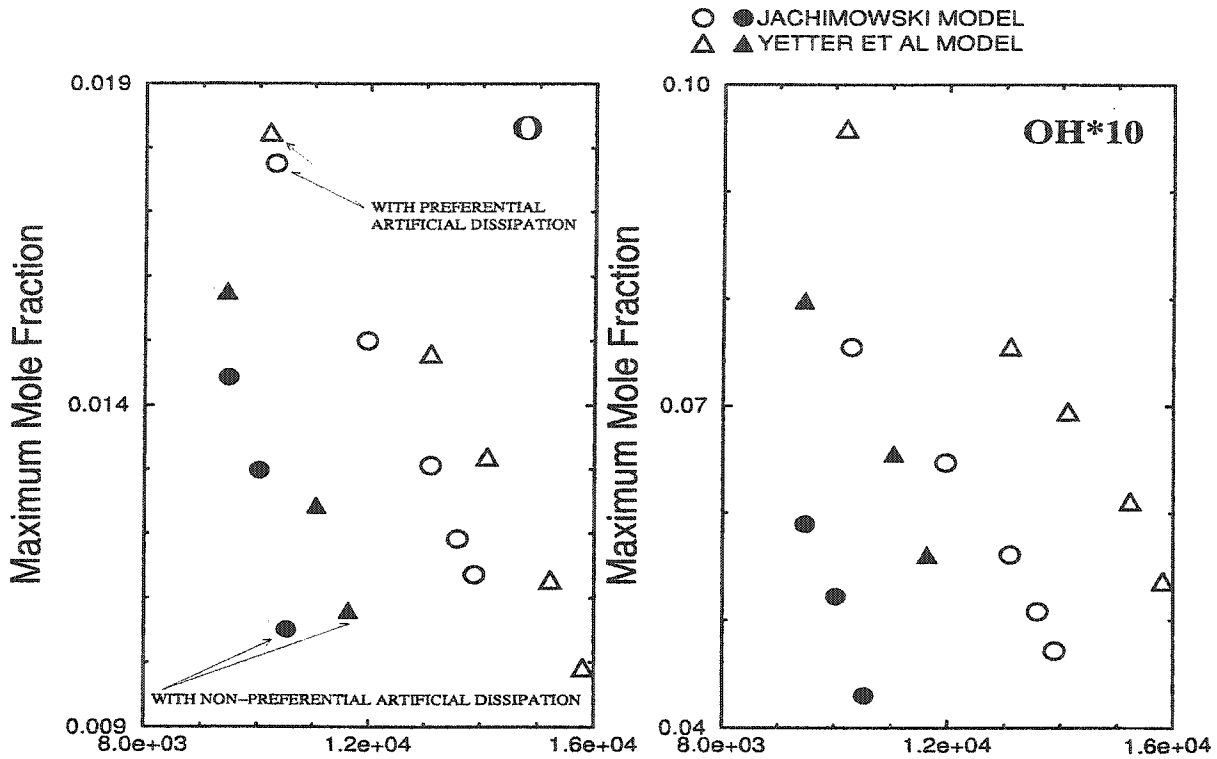

Fig. 5.31 **Centerline peak species** distributions of **plug inflow** induced 100% hydrogen-air diffusion flames for different dissipative coefficients before extinction.

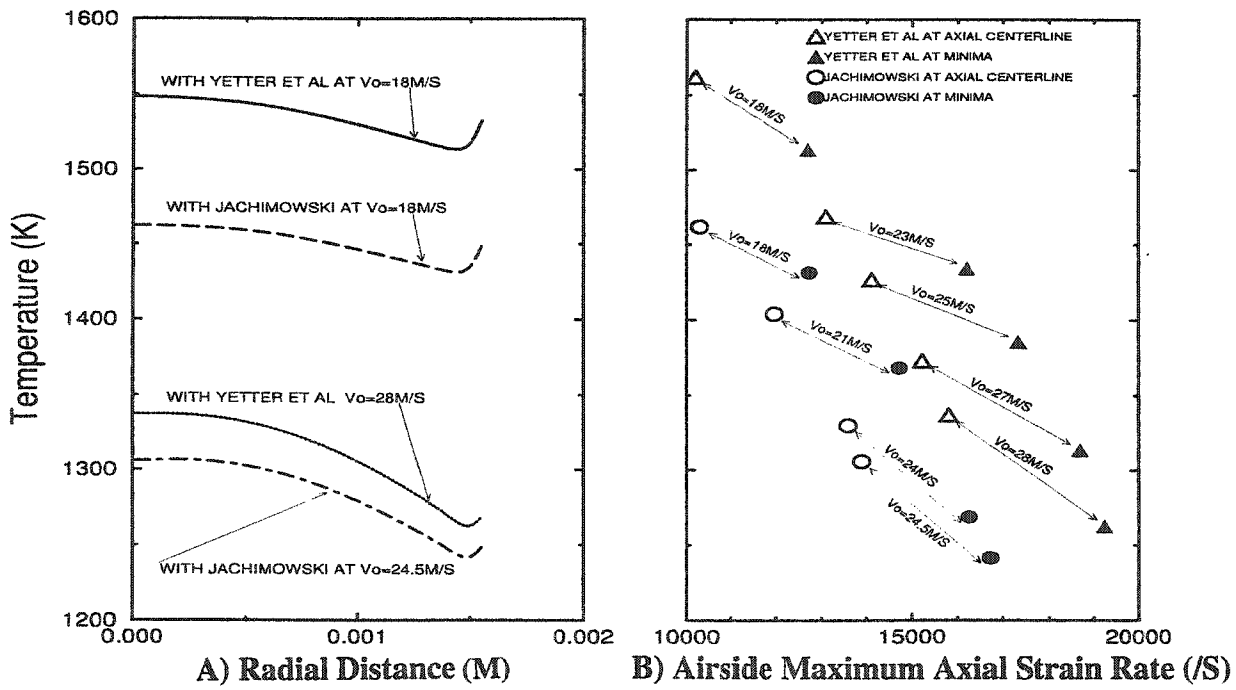

Fig. 5.32 **Flame core radial temperature** distributions (left); and **centerline and Minima flame core** temperature differences (right), of **plug inflow** induced 100% hydrogen-air diffusion flames for different chemistry models before extinction.

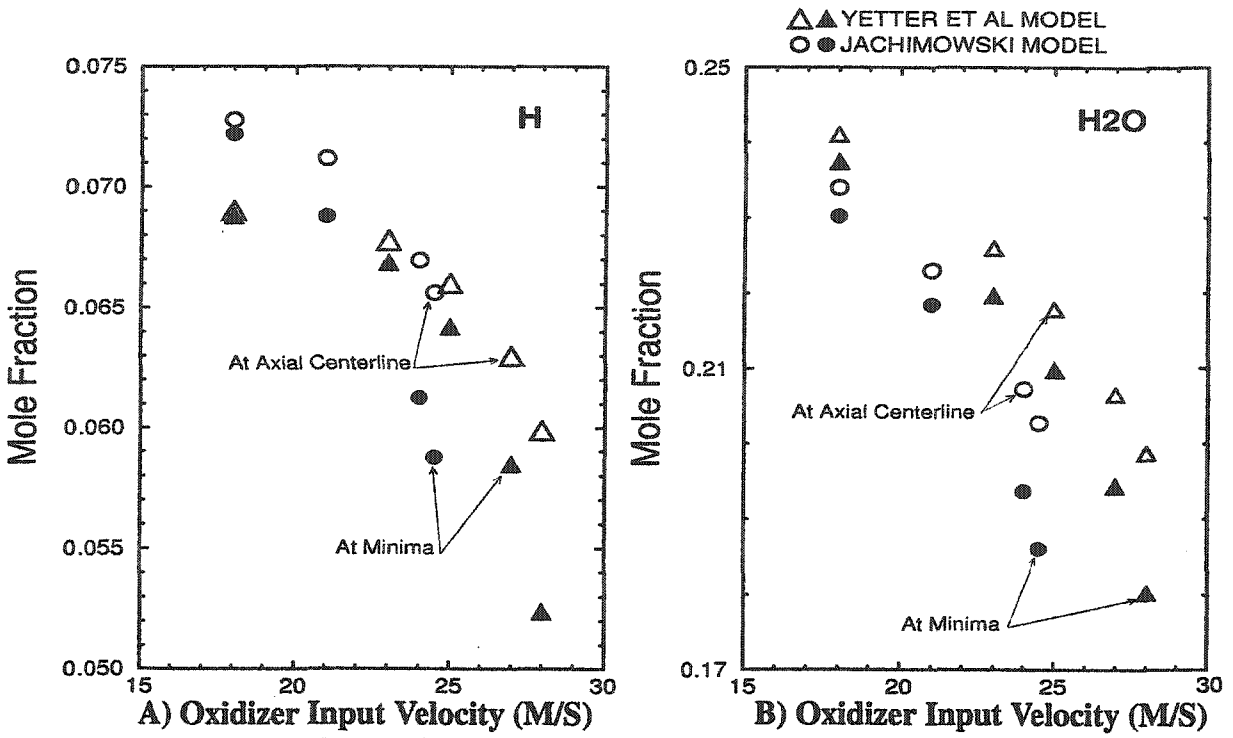

Fig. 5.33 Peak H and H_2O distributions of **plug inflow** induced 100% hydrogen-air diffusion flames for radially different flame core locations before extinction.

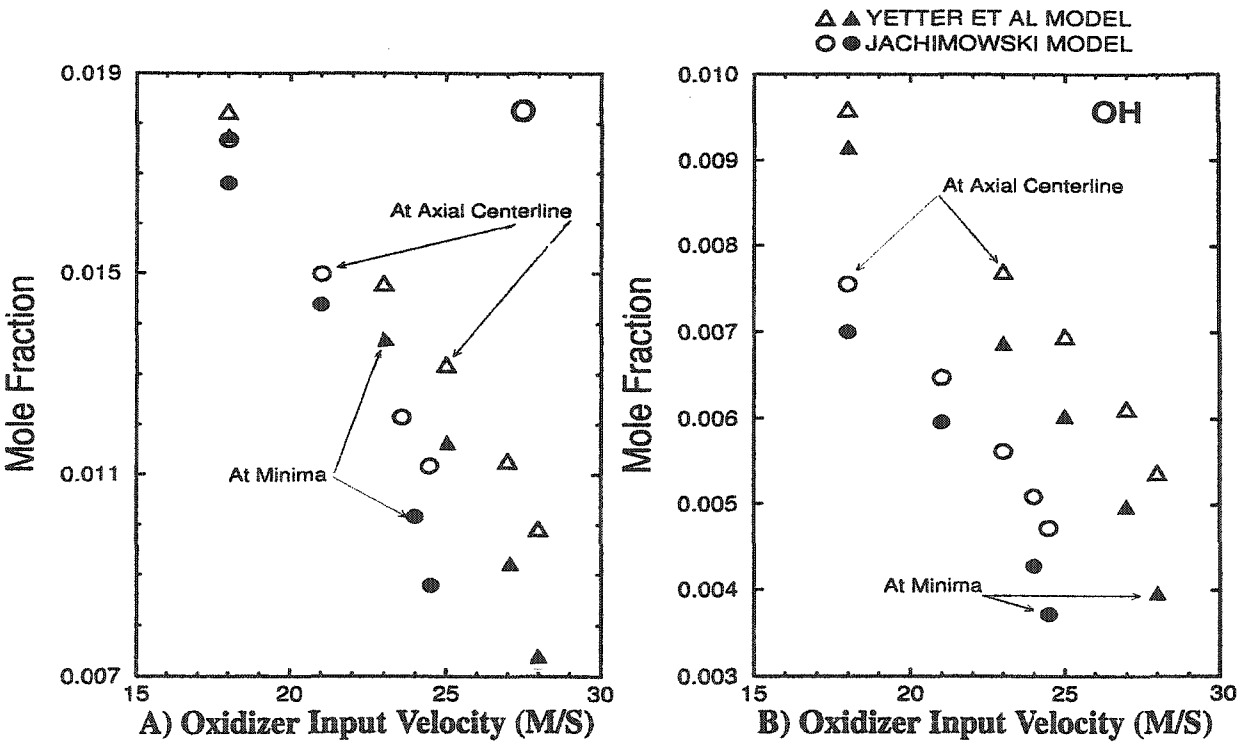

Fig. 5.34 Peak O and OH distributions of **plug inflow** induced 100% hydrogen-air diffusion flames for radially different flame core locations before extinction.

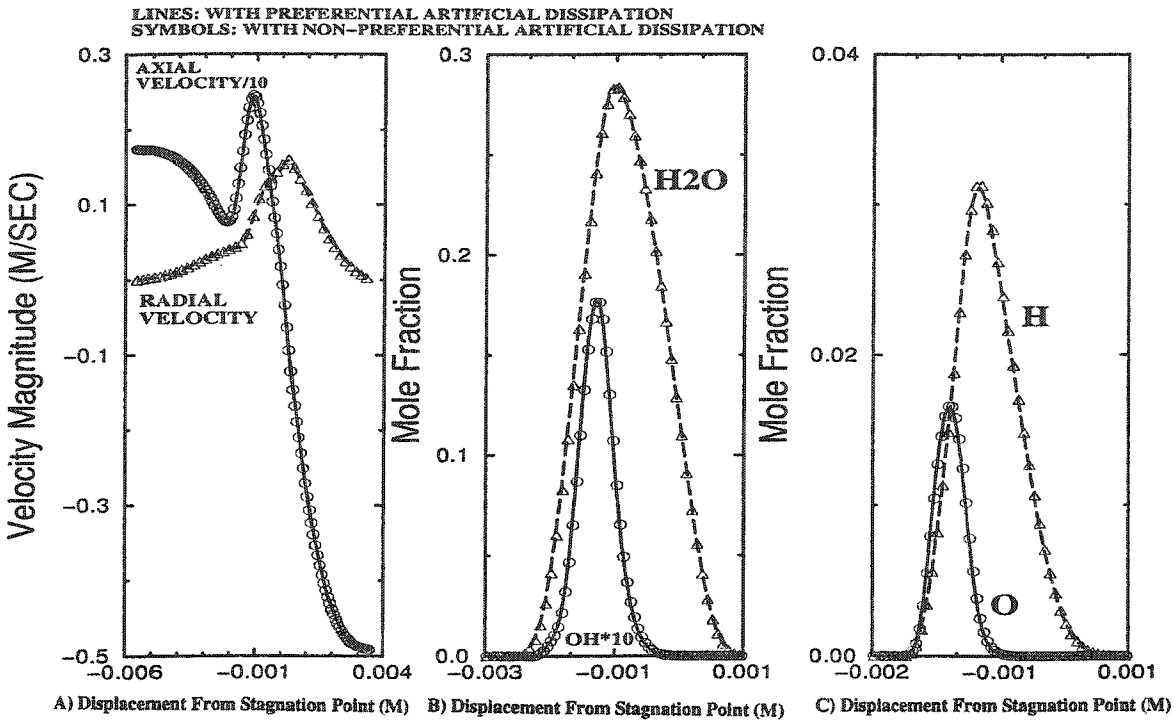

Fig. 5.35 Characteristics of **plug inflow** induced 100% hydrogen-air diffusion flames under influence of artificial dissipations at **lightly** strained condition (oxidizer input velocity of 1.8 meters per second).

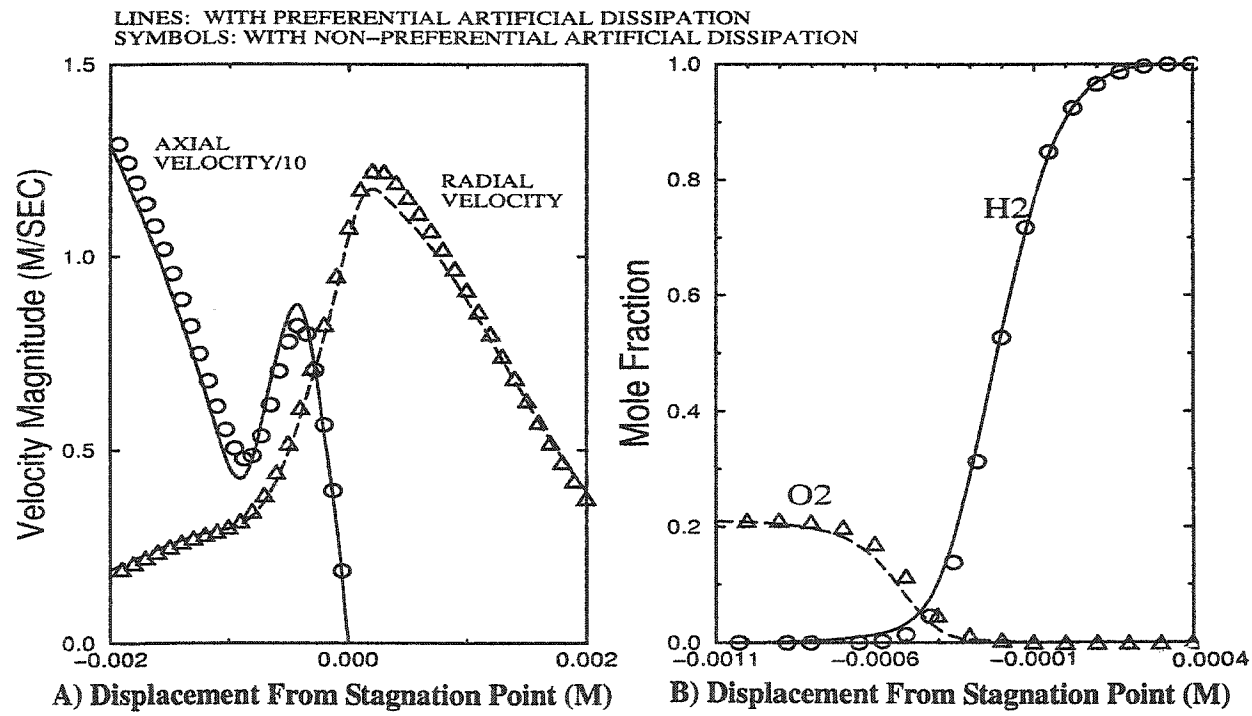

Fig. 5.36 Characteristics of **plug inflow** induced 100% hydrogen-air diffusion flames under influence of artificial dissipations at **highly** strained condition (oxidizer input velocity of 18 meters per second)

Table 5.1 Parametric specifications of lightly strained 100% hydrogen-air opposed jet diffusion flames.

Case #	Tube Diameter (meters)	Separation Distance (meters)	Oxidizer Mole Fraction			Fuel Mole Fraction	Oxidizer Input Velocities (meters per second)	Fraction of Fuel Velocities Balanced with Oxidizer Velocities (Using 1-D Momentum Equation)
			O_2	H_2O	N_2	H_2		
1	0.005	0.005	21	0	79	100	1	0.48
2	0.003	0.006	21	0	79	100	3,4,5	1.00
3	0.003	0.009	21	0	79	100	3,4,5	1.00
4	0.003	0.009	21	0	79	100	3,4,5	0.80
5	0.003	0.006	21	5	74	100	3,4,5	1.00
6	0.003	0.006	20	0	80	100	3,4,5	1.00
7	0.003	0.006	22	0	78	100	3,4,5	1.00

* All flows are simulated using plug inflow type.

Table 5.2 Various axial centerline strain rates near extinction limit (*) for 100% hydrogen-air opposed jet diffusion flames using Jachimowski kinetic model and plug inflows.

V_{ox}	V_{ox}/D	Airside Maximum Axial Strain rate	Flame Core Radial Strain rate	Stagnation Point Radial Strain Rate
18.0	6000	10291	10017	17710
21.0	7000	11959	11178	20706
23.0	7667	13106	12005	22544
24.0	8000	13590	13047	23464
24.5*	8167	13888	13198	24037

Table 5.3 Various axial centerline strain rates near extinction limit (*) for 100% hydrogen-air opposed jet diffusion flames using Yetter et al. kinetic model and plug inflows.

V_{ox}	V_{ox}/D	Airside Maximum Axial Strain Rate	Flame core Radial Strain Rate	Stagnation point Radial Strain Rate
18.0	6000	10189	10385	17691
23.0	7667	13100	12250	22470
25.0	8333	14111	13101	24679
27.0	9000	15227	13877	26370
28.0*	9333	15808	14531	27692

Table 5.4 Axial centerline peak temperatures and species mole fractions near extinction limit (*) for 100% hydrogen-air opposed jet diffusion flames using Jachimowski kinetic model and plug inflows.

V_{ox}	MLSR (1/S)	T (K)	H	H_2O	O	OH
18.0	10291	1462	0.07279	0.2335	0.01762	0.007534
21.0	11959	1404	0.07118	0.2230	0.01508	0.006471
23.0	13106	1362	0.06910	0.2142	0.01319	0.005660
24.0	13590	1325	0.06677	0.2063	0.01172	0.005076
24.5*	13888	1306	0.06563	0.2028	0.01136	0.004715

Table 5.5 Axial centerline peak temperatures and species mole fractions near extinction limit (*) for 100% hydrogen-air opposed jet diffusion flames using Yetter et al. kinetic model and plug inflows.

V_{ox}	MLSR (1/S)	T (K)	H	H_2O	O	OH
18.0	10189	1562	0.06905	0.2410	0.01824	0.009590
23.0	13100	1469	0.06778	0.2260	0.01482	0.007695
25.0	14111	1427	0.06602	0.2179	0.01319	0.006950
27.0	15227	1379	0.06303	0.2066	0.01128	0.006110
28.0*	15808	1337	0.05988	0.1987	0.00992	0.005365

Table 5.6 Minimum point (in radial direction) peak temperatures and species mole fractions near extinction limit (*) for 100% hydrogen-air opposed jet diffusion flames using Jachimowski kinetic model and plug inflows.

V_{ox}	MLSR (1/S)	T (K)	H	H_2O	O	OH
18.0	12730	1431	0.07220	0.2302	0.01681	0.007000
21.0	14721	1368	0.06879	0.2185	0.01438	0.005956
24.0	16256	1269	0.06125	0.1937	0.01016	0.004270
24.5*	16733	1241	0.05877	0.1861	0.00879	0.003710

Table 5.7 Minimum point (in radial direction) peak temperatures and species mole fractions near extinction limit (*) for 100% hydrogen-air opposed jet diffusion flames using Yetter et al. kinetic model and plug inflows.

V_{ox}	MLSR (1/S)	T (K)	H	H_2O	O	OH
18.0	12701	1514	0.06879	0.2374	0.01767	0.009149
23.0	16200	1434	0.06684	0.2196	0.01340	0.006867
25.0	17330	1385	0.06419	0.2098	0.01149	0.006024
27.0	18685	1313	0.05846	0.1944	0.00920	0.004974
28.0*	19230	1262	0.05237	0.1802	0.00730	0.003960

Table 5.8 Axial centerline peak temperatures and species mole fractions near extinction limit (*) for nonpreferentially dissipated (numerical) 100% hydrogen-air opposed jet diffusion flames using Jachimowski kinetic model and plug inflows.

V_{ox}	MLSR (1/S)	T (K)	H	H_2O	O	OH
18.0	9478	1363	0.06583	0.2166	0.01443	0.005897
19.0	10021	1325	0.06254	0.2081	0.01299	0.005221
20.0*	10527	1268	0.05587	0.1926	0.01051	0.004298

Table 5.9 Axial centerline peak temperatures and species mole fractions near extinction limit (*) for nonpreferentially dissipated (numerical) 100% hydrogen-air opposed jet diffusion flames using Yetter et al. kinetic model and plug inflows.

V_{ox}	MLSR (1/S)	T (K)	H	H_2O	O	OH
18.0	9446	1482	0.06419	0.2277	0.01577	0.007983
21.0	11046	1382	0.05816	0.2073	0.01244	0.006556
22.0*	11637	1340	0.05462	0.1992	0.01081	0.005610

CHAPTER VI

OPPOSED JET DIFFUSION FLAMES WITH PARABOLIC INFLOW BOUNDARIES

The opposed jet diffusion flames responding to different inflow boundaries display distinctive flame structure and extinction characteristics. Experiments performed in laboratory environments are often associated with two extremes of the flow boundaries, namely plug and parabolic inflows. The plug inflow flames are created in experiments using high contraction ratio nozzles that generate nearly uniform-velocity fuel and oxidizer jets establishing a flame [17]. Numerically, the nozzle inflow flames can be approximately simulated for large closely-spaced nozzle by using one dimensional techniques, although these techniques are incapable of either imposing the precise velocity profile at the inflow boundaries [17, 28, 29] or generating a 100% hydrogen-air flame [17, 30-32]. Alternately, a direct two-dimensional technique is utilized here to simulate laboratory flames, in which the details of 100% hydrogen-air flame structure and extinction characteristics using plug inflow boundaries were examined in the preceding chapter.

Parabolic inflow flames are formed in the laboratory using constant diameter tubes that generate fully developed flows, with maximum axial velocity ($2U_{mean}$) at the axial centerline (Fig. 6.1). Experimentally, extensive research has been performed to globally characterize flame extinction using the hydrogen-air system [17]. However, at least with the highly strained and concentrated hydrogen-air system, the one-dimensional techniques have failed to produce results that adequately characterize the flames [17].

As a part of continuing efforts to investigate the effects of flow boundaries on critical flame characteristics, the details of parabolic inflow induced flames are presently investigated

using two-dimensional numerical technique. This study begins with the axisymmetric opposed jet configuration at a moderate separation distance of two tube diameters, which has been shown to be well within the region of "ideal" behavior [17]. The study is focused to provide, first, a comparative discussion between the parabolic and plug inflow induced flames at lightly strained conditions; this is presented in Sec. 6.1. Then, the details of a flame responding to parabolic inflow boundaries near, and also at the extinction limit are examined in Sec. 6.2. Finally, postextinction torus-shaped flames, along with detailed flame reattachment characteristics, are addressed in Sec. 6.3.

6.1 Diffusion Flames at Lightly Strained Condition

Recent experimental studies have reported that parabolic inflow flames have significantly different global characteristics than plug inflow flames. In particular, the parabolic inflow flames require much smaller global applied stress rate to reach flame extinction than the plug inflow flames [17]. Therefore, the comparative difference in the structure of lightly strained flames at two extremes of inflow boundaries needs to be examined. In essence, knowledge gained in this study might be used as building blocks in characterizing parabolic inflow flames at the extinction limit.

In this study, flames are simulated using 3 millimeter diameter tubes with a separation distance of 6 millimeters. The airside oxidizer consists of 21% O_2 and 79% N_2 in volume, whereas the fuel is pure hydrogen gas. Also, nitrogen coflow gas is utilized for flame stability at an average axial magnitude of 0.1 m/sec. For the comparison, the parabolic inflow flame is simulated at an oxidizer axial centerline velocity of 6 m/sec, and the plug inflow flames are created at a mean oxidizer velocity of both 3 and 6 m/sec. In all cases, the fuel velocities are calculated using the

one dimensional approximation of the momentum equation. Also, the adiabatic and no slip conditions are applied to the tube walls. The parabolic profiles at both inflow boundaries are approximated using the following expression,

$$U(r) = 2U_{mean}[1-r/R]^{0.561553}$$

where R is the tube radius.

Typical plots of centerline axial velocity, temperature and major species distributions induced by plug and parabolic inflow boundaries are shown in Figs 6.2 and 6.3. The flames are simulated using an oxidizer axial centerline velocity of 6 m/sec for the parabolic case, and 3 and 6 m/sec for the plug inflow cases. The tube diameter averaged parabolic inflow for a 6 m/sec centerline velocity would be identical to that for the 3 m/sec plug inflow case.

Overall, the parabolic case has a smaller FWHM flame thickness that is closer to the stagnation point than for both plug flow flames. Also, the parabolic inflows induce comparatively greater flame stretching than the plug inflows. For instance, at an average oxidizer inflow *axial* velocity of 6 m/sec, the parabolic flame results in a maximum local airside axial strain rate (MLSR) of 3848 per second, whereas, the plug flame results in a strain rate of 1427 per second. Thus, the parabolic flame has 2.69 times larger MLSR than the plug flow flame even though the average oxidizer input velocity is identical to that for plug inflow. Note, furthermore, that this strain rate ratio (2.69) still remains almost exactly identical to the 2.53 ratio for nonreacting flows at the stagnation point (shown in Chap. 4). Thus the greater axial stretching appears consistent with a significantly greater radial divergence of flow for parabolic than for plug inflows (which can be assessed), because the parabolic flame exhibits smaller peaks in temperature, H_2O, and OH; and a larger peak in H.

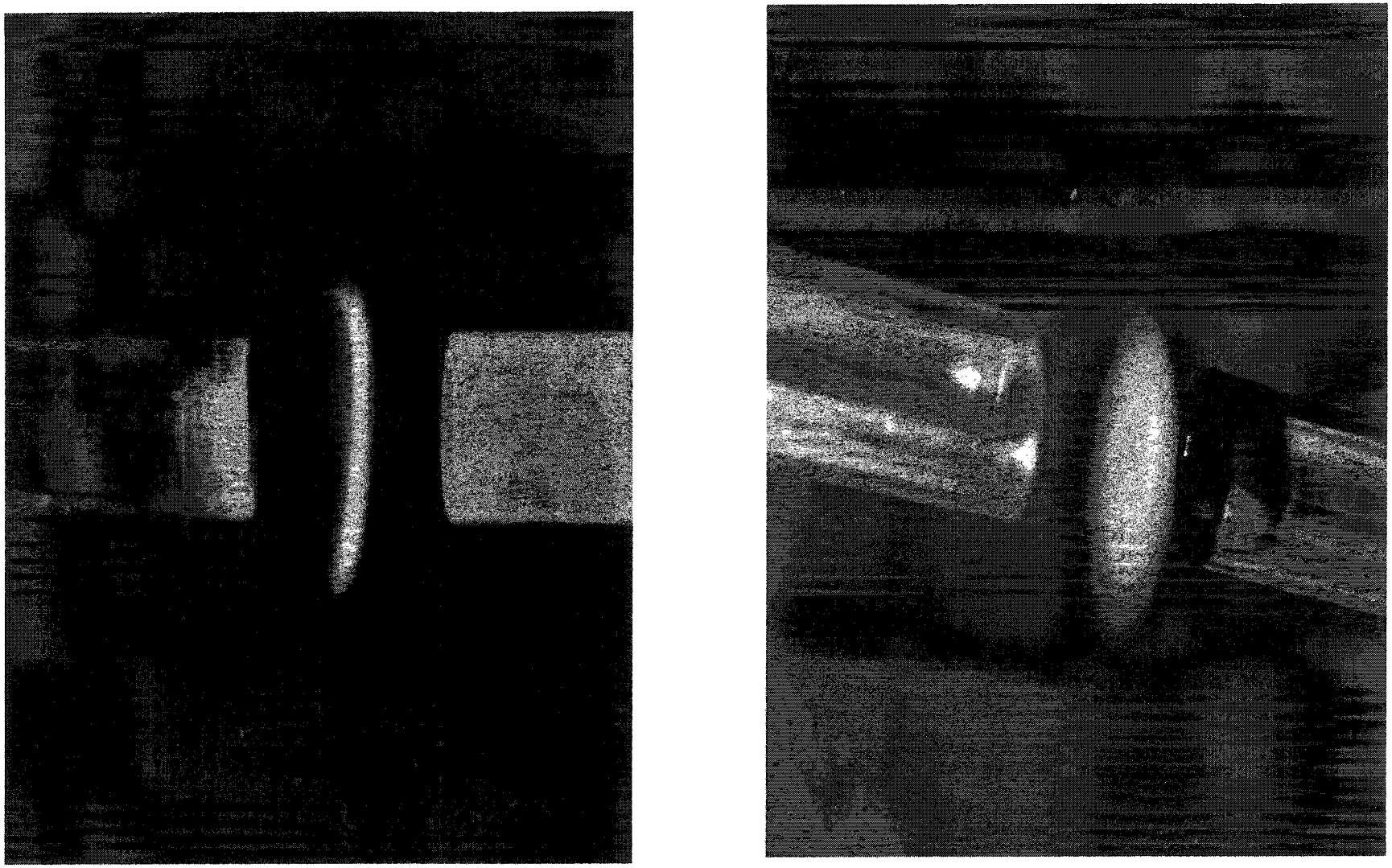

Fig. 6.1 Photographic images of opposed jet diffusion flame using constant diameter tubes [63].

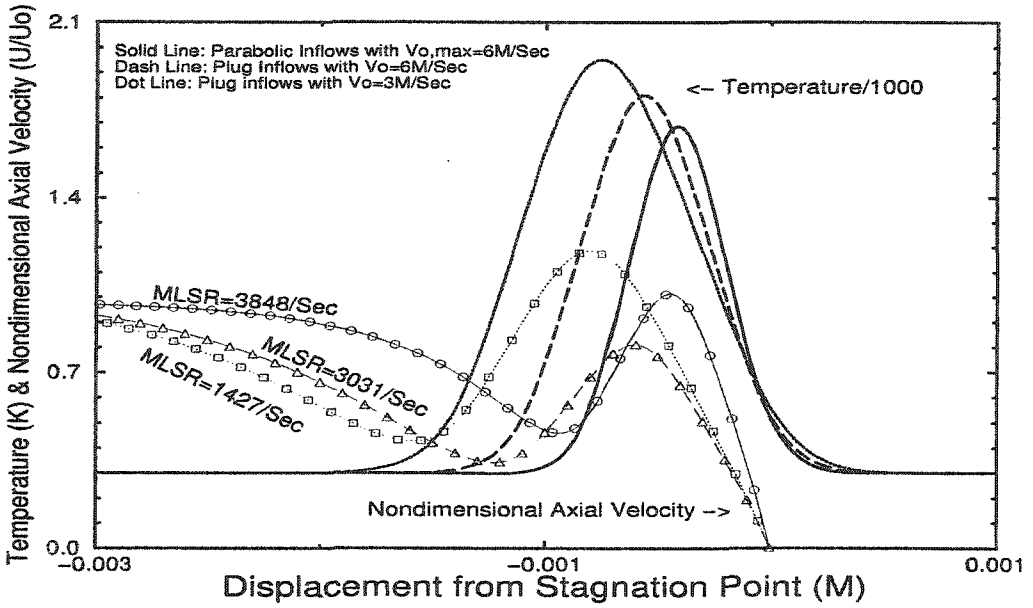

Fig. 6.2 Centerline temperature and axial velocity differences between plug and parabolic inflow induced 100% hydrogen-air counterflow diffusion flames at relatively low oxidizer input velocities.

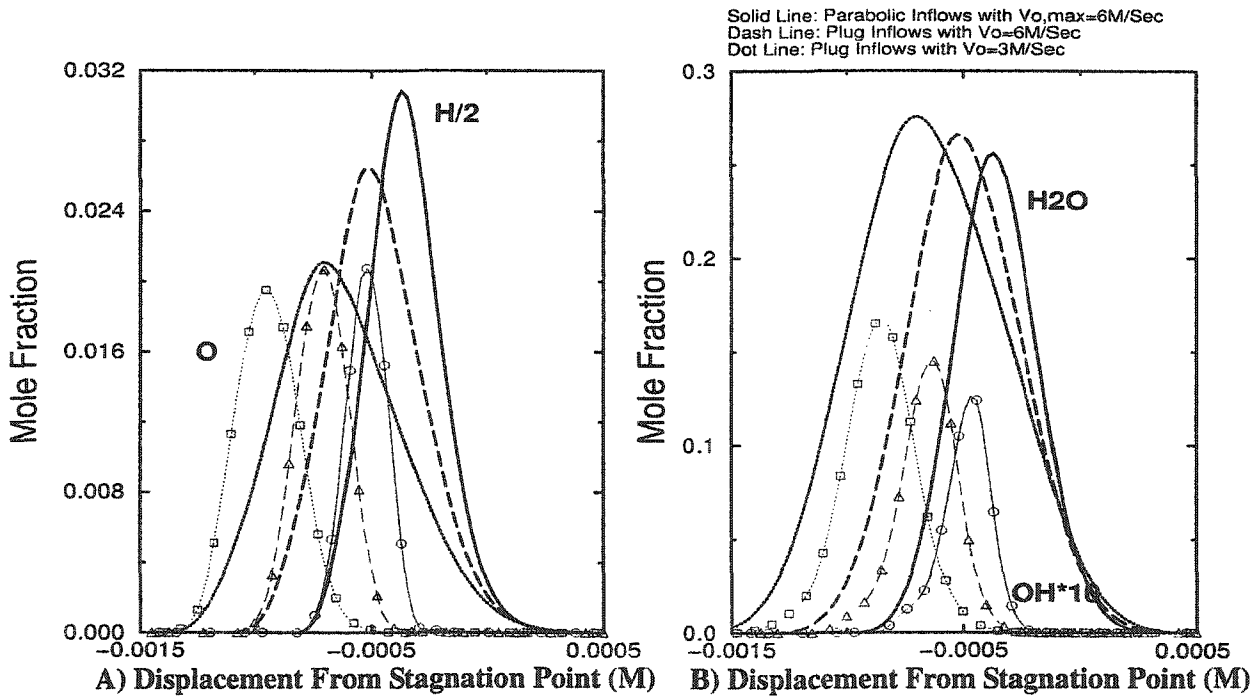

Fig. 6.3 Centerline species distributions over plug and parabolic inflow induced 100% hydrogen-air counterflow diffusion flames at relatively low oxidizer input velocities.

6.2 Diffusion Flame at Extinction Limit

Superficially, parabolic inflow induced flames show no reasonable difference in overall structural characteristics near extinction, compared to plug flames. Figures 6.4 and 6.5 illustrate that peak temperature and major species concentrations at the centerline fall precipitously as the input velocities increase towards flame extinction, as indicated by achievement of near vertical tangencies. Relatively, flame extinction occurs at lower input velocity for the Jachimowski kinetic model than the Yetter et al. model.

However, the parabolic flame has four distinct extinction characteristics that differentiate it from the plug flame. First, the parabolic flame extinction initiates from the axial centerline region and propagates outward. Whereas, the plug flame first weaken most at unit radial distance in the downstream -- note this should not be confused with true extinction, which occurs on the centerline. The parabolic flame has a 5% smaller centerline peak temperature (and major species concentration) near the extinction limit than the plug inflow flame. The parabolic flame extinguishes when the centerline peak temperatures reach 1241K and 1260K for the Jachimowski and Yetter et al. models, respectively (Tables 6.3 and 6.4). These are comparable to the extinction characteristics of and "extended" plug flame in which the local peak "extinction" temperatures at unit radius distance downstream are 1241K and 1262K with the Jachimowski and the Yetter et al. models, respectively (Tables 5.6 and 5.7). Nonetheless, a significant difference is actually seen with the plug flame in which the central flame extinguishes at centerline peak temperatures of 1306K and 1337K for Jachimowski and Yetter et al. models, respectively (Tables 5.4 and 5.5).

Second, the extinction of a plug inflow flame has a relatively wide disparity (9.6%) in centerline flame core radial strain rates for different models (13198 per second using Jachimowski model and 1453 per second using Yetter et al. model; Tables 5.2 and 5.3). However, the parabolic

inflow flame has a flame core radial strain rate that is nearly identical for the respective chemical models (13113 per second using Jachimowski model and 13034 per second using Yetter et al. model; Tables 6.1 and 6.2). The 9.6% wide disparity in the maximum **centerline** radial strain rate for the plug inflow flame using different kinetic models, appears largely due to a lack of precision of the extinction simulations derived from selection of test input velocities (see Fig. 5.29).

Third, the extinction of a parabolic flame is achieved at lower input velocity, or applied stress rate, than the plug flame (Tables 6.1 and 6.2). The parabolic input boundary flame extinguishes at the centerline oxidizer input velocity of 11.7 m/sec, or oxidizer applied stress rate of 1950 per second, using the Jachimowksi model. The Yetter et al. model predicts slightly larger values than the Jachimowski model; i.e. 12.9 m/sec and 2150 per second, respectively. In comparison, the plug flow flame extinguishes at (1) an oxidizer input velocity of 24.5 m/sec and applied stress rate of 8167 per second, using Jachimowski model; or (2) at 28 m/sec and 9333 per second, using Yetter et al. model (Tables 5.2 and 5.3). The reason for the large difference in applied stress rates for the different input types is that, as shown in the previous section, the parabolic input flame experiences far greater radial flame stretching per unit input velocity than the plug input flame.

It is noted that the computational results using the parabolic input boundaries are very comparable to earlier experimental results by Pellett et al. [17], who reported that flame extinction is achieved at the mean oxidizer velocity of 5.55 meters per second at 300K, using a 2.7 millimeters diameter tube. This translates into an applied stress rate at extinction of 2054 per second, which compared with 1950 per second for the Jachimowski model and 2150 per second for the Yetter et al. model. By accounting for the small difference in tube diameter, the predicted results

using both chemical models are respectively within -5.1%(Jachimowski) and +4.7% (Yetter et. al.) of the grand average applied stress rate measurements.

Finally, the parabolic inflow flame has different *relative* strain rate correlation characteristics as follows. First, at extinction, the airside maximum axial local strain rate (MLSR) for the plug induced flame is 1.77 times larger than for the parabolic flames. The parabolic flame has a maximum centerline axial strain rate factor (axial strain rate/applied stress rate) of 4.16. Next, the centerline radial strain rate factors (radial strain rate/applied stress rate) are much higher for the parabolic inflow flame than for the plug inflow flame. The results show that the parabolic inflow induced flame core has a centerline maximum radial strain rate factor of 6.1 and 6.7 for the Yetter et al. and Jachimowski models. The plug inflow induced flame has a factor of 1.56 and 1.62 for the respective kinetic models. Lastly, the parabolic flame has a centerline radial flame core to axial strain rate ratio greater than unity, at 1.46 and 1.67 using Yetter et. al. and Jachimowski models, respectively. On the other hand, the plug inflow flame has a centerline radial flame core to axial strain rate ratio less than unity at 0.92 and 0.95 respectively for the two kinetic models.

Thus the different input flows have significantly different flame stretching characteristics, and both sets differ from the idealized 1-D values of 0.5. This difference is partially due to the fact that, as discussed in Chap. 4, the central flow within a flame diverges greater for the parabolic input than the for plug input flows. However, an additional part of the observed "derivations" from an idealized 0.5 probably arises from the finite size of the nozzles and the use of actual flame core strain rates to measure extinction.

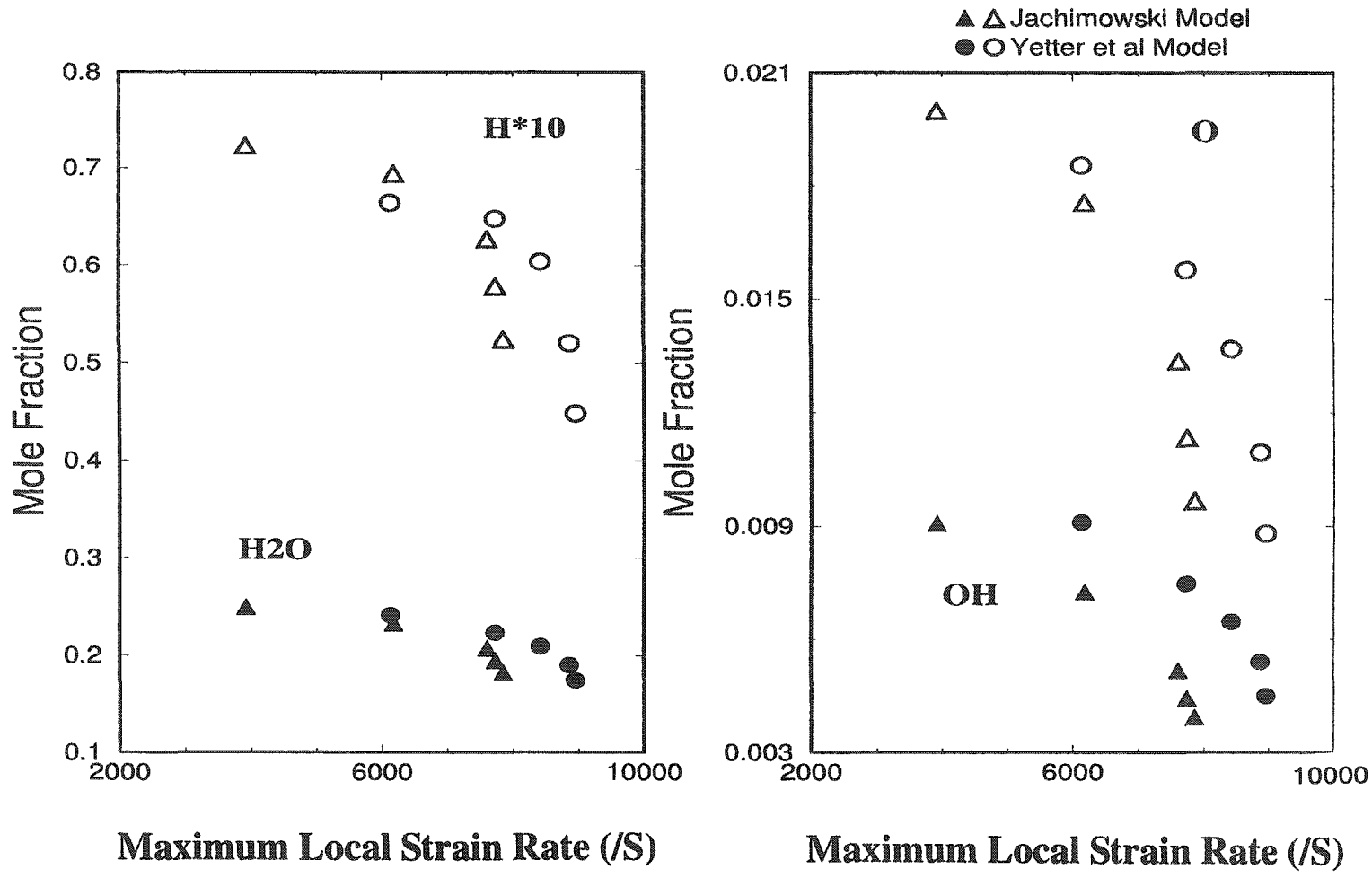

Fig. 6.4 Centerline peak species distributions of parabolic inflow induced 100% hydrogen-air diffusion flames before extinction.

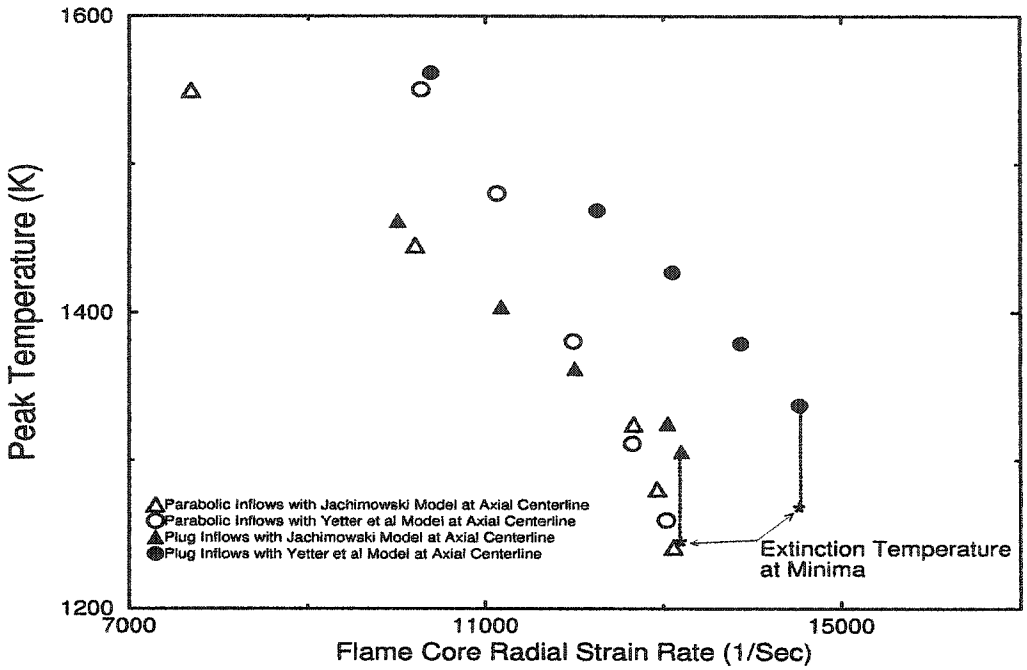

Fig. 6.5 Centerline peak temperature distributions of plug and parabolic inflow induced 100% hydrogen-air diffusion flames before extinction.

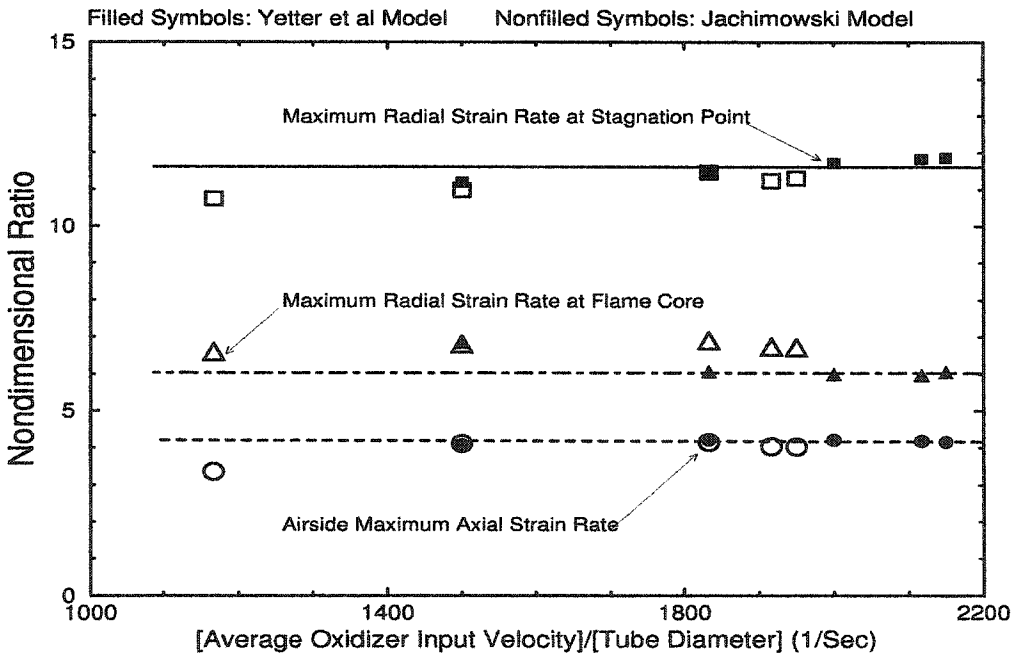

Fig. 6.6 Correlated distributions of various centerline strain rates for parabolic inflow induced 100% hydrogen-air diffusion flames before extinction (using applied stress rates).

6.3 Postextinction Flame

With an opposed jet configuration, a postextinction flame is obtained after achieving local extinction of the diffusion flame (Fig. 6.7). This "broken flame" with a hole in the center was first reported by Potter and Butler [14], but received little attention. However, due to the uniqueness in transitional characteristics between these two distinct flames which could provide building blocks for characterizing reignition and extinction in a turbulent diffusion flamelet, the postextinction flame has attracted renewed research interests recently. Experimentally, Pellett et. al. reported extensive characterizations of the so-called ring shaped flame after blowoff and its restoration [16, 17]. Numerically, some progress has been made in validating the experimental measurements [46, 47].

The postextinction flame occurs just after the stretching limit of the diffusion flame becomes critical in the centerline region, in which the rate of convective heat loss exceeds heat generation due to combustion at falling temperature. As a result, the core of the diffusion flame extinguishes radially, creating a ring type flame that stabilizes outside the jet radius, depending on jet flows and concentric "shroud" flows. The ring-like or torus flame is stable and stationary, but is not necessarily stabilized in the stagnation plane as previously thought [17]. Its radial and unsymmetrical axial position is the result of axial momentum exchange and radial divergence of flow (outward), and inward flame propagation toward the centerline region.

Unlike a premixed flame, the propagation speed of a postextinction flame depends not only on the kinetic and thermodynamic properties of the mixture, but also on the transverse and radial gradients of mixture concentration and flame curvature [66]. The postextinction flame is tribrachial, in which the flame consists of rich and lean premixed zones in the frontal edges of a positively propagating (toward the axial centerline) flame, followed by the trailing zones of fuel

rich and fuel lean diffusion flames [46]. Thus the postextinction flame has a much different flame structure than the typical counterflow diffusion flame generated with the opposed jet configuration.

This portion of the study investigates the underlying physical mechanism as well as the overall flame structure and characteristics in comparison with the preextinction flame. In this study, postextinction flames are simulated using the Jachimowski kinetic model. The flame is generated with 100% hydrogen fuel impinging against an air jet at a separation distance of 6 millimeters, where both inflows are assumed parabolic. Pure nitrogen is utilized as the coflow gas with a mean input velocity of 0.1 meters per second. This differs from the assertion in earlier work by Lee et al. [46] that the postextinction flame could only be achieved without coflowing gas. In this study, the extinction of the parabolic inflow counterflow diffusion flame is achieved at the oxidizer centerline velocity of 11.7 meters per second and mean applied stress rate of 1950 per second (Jachimowski kinetic, Table 6.1).

Figures 6.8-6.12 show the temperature and major species distributions for pre- and postextinction states, as well as the flame restoration. Thus the results clearly display that two distinctly different flames can exist for identical input conditions, although their formations are the result of complex interplay among flow, transport, and thermochemical processes in the vicinity of the impingement region.

The postextinction flame shows three distinct characteristics differentiating it from the counterflow diffusion flame. First, because the oxidizer gas impinges against fuel without reacting in the center, a density contribution of nonreacting gas to the axial momentum appears, which differs from the augmented axial velocity of a combusting flow. Consequently, the centerline stagnation point shifted physically 0.15 millimeters toward the fuel side. Second, the fuel diffuses

much further into the oxidizer through the centrally hollow impingement region. In addition, even though the input axial momentum fluxes for both fuel and oxidizer are balanced overall, momentum fluxes closer to the tube walls are relatively perturbed for fuel compared to those for oxidizer because of unsymmetrical divergence of flow about the stagnation plane. As a result, the postextinction (ring) flame is displaced and stabilizes closer to the oxidizer side, slightly above the tube exit edge. Lastly, the postextinction flame has a near symmetric flame structure in the trailing region (negative propagation region), in which no significant flame curvature is observed. But the stoichometric line in the leading edge (positive propagation zone) is inclined toward the fuel side, closer to the stagnation point. This indicates that central flame restoration would occur as the frontal region of a flame travels radially toward the axial centerline, as well as traversely closer to the stagnation point.

The postextinction flame is smaller in overall size than the diffusion flame at a radius greater than 1.5 millimeters, under identical input conditions. However, the flame retains similar maximum temperature and major species mole fractions at the flame core, comparable to preextinction flame is a counterflow diffusion flame, in which fuel diffuses into the oxidizer forming a convectively strained flame. However, the postextinction flame is tribrachial, as illustrated in Fig. 6.13, where its temperature isocontours are superimposed on the mole fraction isocontours of both fuel and oxidizer. The flame has a premixed region in the leading (positive propagation) edge (where a sudden retardation of the isocontours of both oxidizer and fuel occurs), which is much smaller than the trailing region of the diffusion flame. In particular, the fuel lean premixed zone (where a sudden retardation of fuel isocontours occurs) is located on the oxidizer side relative to the frontal propagating point. The fuel rich premixed zone (where a sudden retardation of oxidizer isocontours occurs) is located on the fuel side, along the fuel side boundary of the flame, which is

proportionally larger than the fuel lean zone. The stoichiometric line coincides with the propagating point and extends through the maximum temperature zone, dividing the diffusion part of the flame into two segments, one fuel lean and one fuel rich [46]. The first segment is bounded by the mixture fraction line and the downstream flame limit, in which the flame is mainly dominated by the availability of the oxidizer in the region [46]. The other segment is bounded by the mixture fraction line and the flame limit closer to the oxidizer outport, where the flame is dominated mainly by the availability of the fuel [46].

In the nearly restored state (with maximum oxidizer velocity of 6.1 meters per second), the flame is no longer symmetric about the radial symmetric line previously defined. The propagating edge of the flame radiates closer to the centerline stagnation point. The flame is still tribrachial and the diffusion parts of the flame are still dominant (Fig. 6.13). But the flame is relatively larger, and has higher maximum core temperature. In fact, the postextinction flame, at this state, has a nearly identical flame shape as the downstream portion of the pre-extinction flame, of identical input boundary conditions. The only difference between the two flames is that the pre-restored postextinction flame still has a nonreacting disk shape zone in the radially central region, although the size of the nonreacting hole is reduced smaller than tube exit diameter.

As the input velocities decrease further, the propagating edge of the flame moves toward the axial centerline, consuming (annihilating) the premixed gas. Ultimately, the central counterflow diffusion flame is re-established with a very small reduction (perturbation) of parabolic input velocity (i.e. airside centerline input velocity from 6.1 to 6.0 meters per second). Consequently, the diffusion flame restoration is achieved at one-half of the flame extinction input velocity.

As shown in Figs. 6.8-6.12, the flame restoration is achieved at the mean oxidizer input velocity of 3 meters per second (or centerline input velocity of 6 meters per second), and the mean

applied stress rate of 1000 per second. Earlier, Pellett et al. [17] reported that flame restoration was achieved experimentally at a mean oxidizer velocity (at 273K) of 2.6 meters per second, using a 2.7 millimeters diameter tube. This translates into flame restoration applied stress rate of 1058 per second at 300K. Thus, the calculated reattachment inflow velocity and applied stress rate are in excellent agreement with the measurement.

Figure 6.14 displays the radial velocity distribution orthogonal to the propagating point of a nearly restored flame, at the centerline oxidizer input velocity of 6.1 meters per second. The results show the radial velocity increases drastically after it reaches the edge of the flame. The local flame propagation speed is obtained at the juncture between radially flowing (outward) non-reacting gas and the positively propagating (protrusion) region of the flame. The calculated speed is about two meters per second, which qualitatively agrees with that of the (unstrained) burning velocity of a fuel rich premixed hydrogen-air system [67]. As the radial nonreacting outward flow velocity becomes smaller than the inward flame propagating speed, a disk like diffusion flame is restored, in which its formation and structure are exactly identical to the preextinction diffusion flame at the identical inflow conditions. In essence, the hysteresis in formation of two distinct flames at an identical inflow condition is observed. Thus, the strain rate itself is not sufficient to characterize the local state of a "laminar" flamelet for a turbulent diffusion flame.

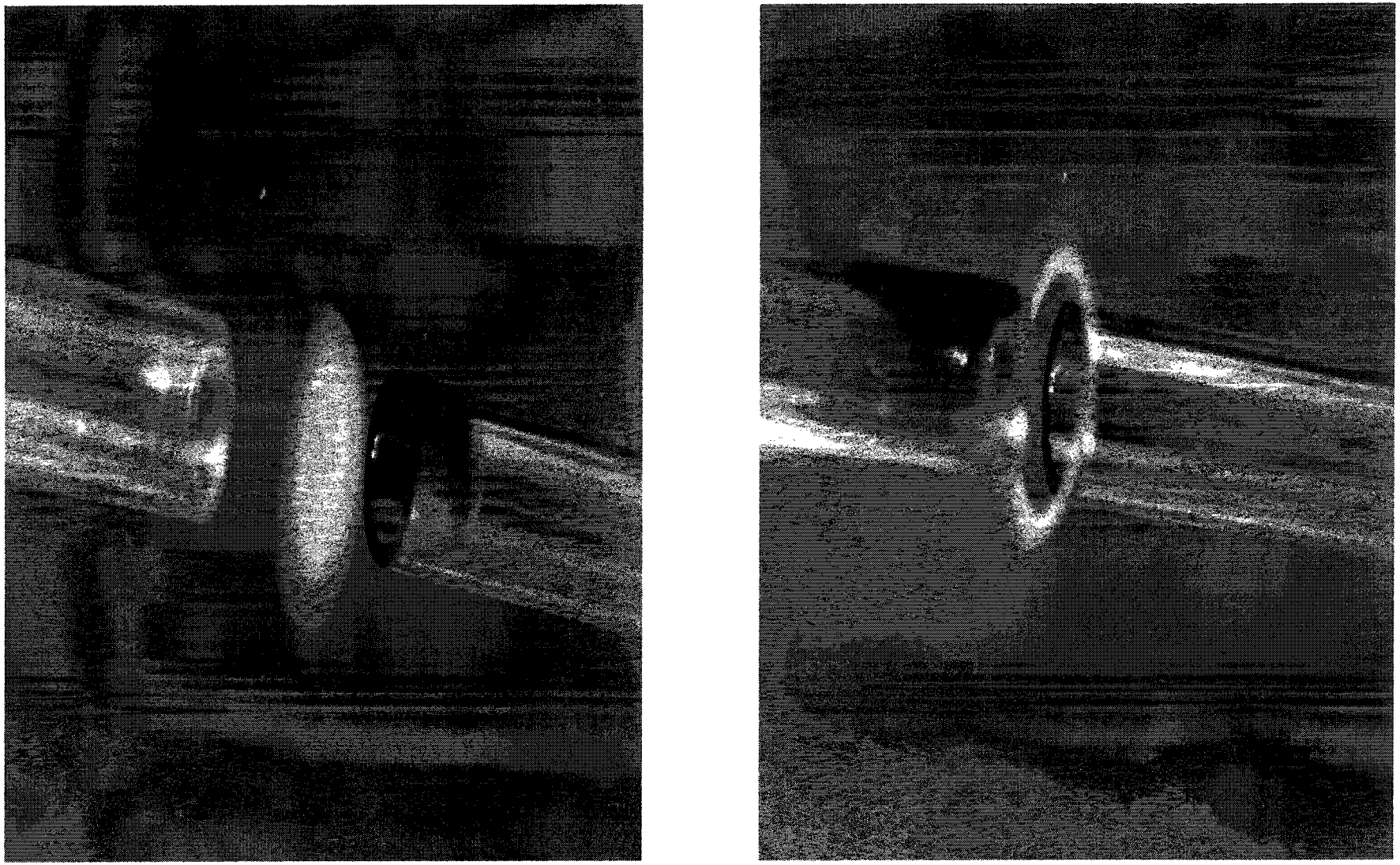

Fig. 6.7 Photographic images of parabolic inflow induced 100% hydrogen-air diffusion flame (left) and postextinction flame (right) [63].

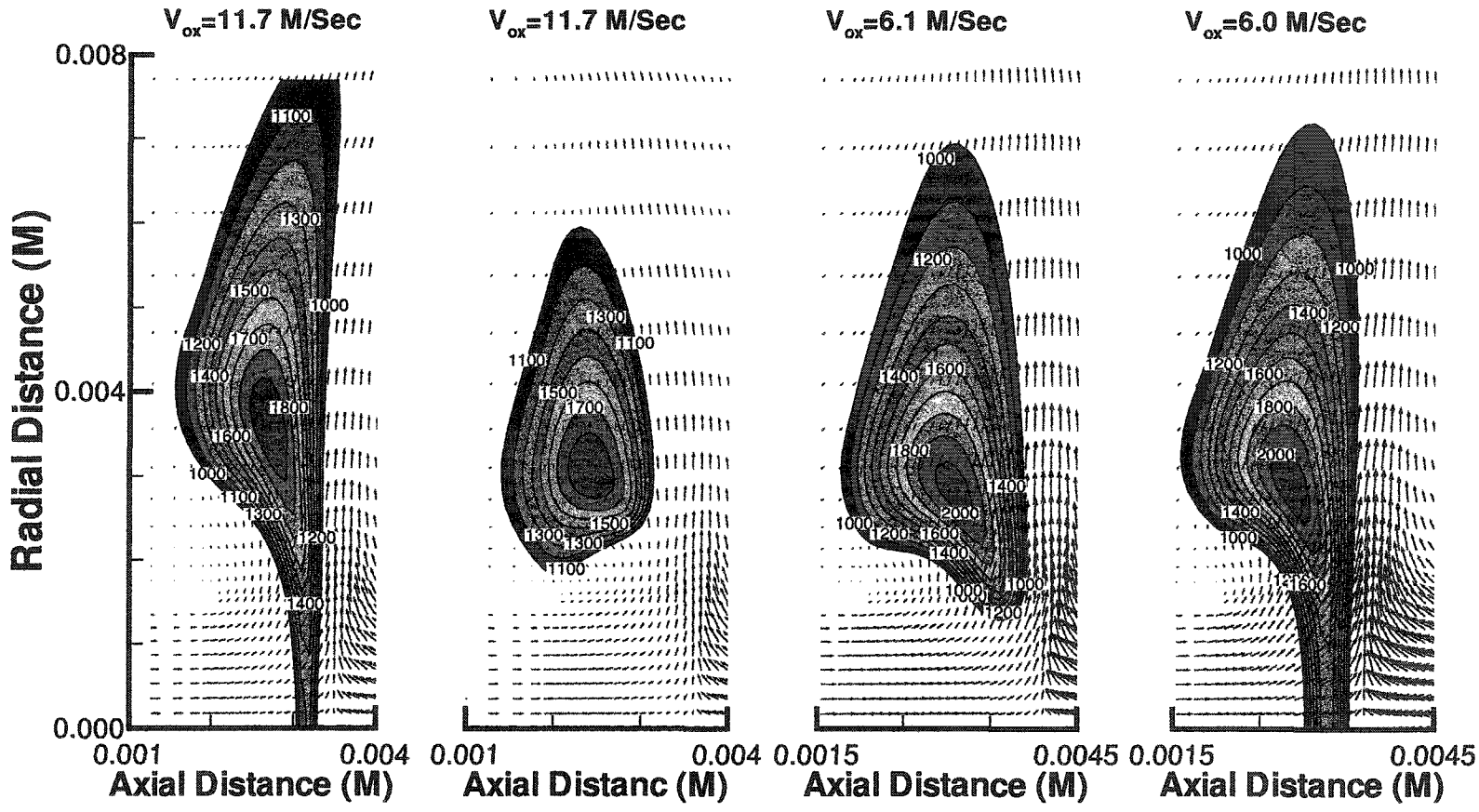

Fig. 6.8 Temperature isocontours and velocity vectors of parabolic inflow induced 100% hydrogen-air diffusion and postextinction flames, for conditions of (left to right) pre-extinction, post-extinction, pre-restoration and post-restoration. Oxidizer is on left side.

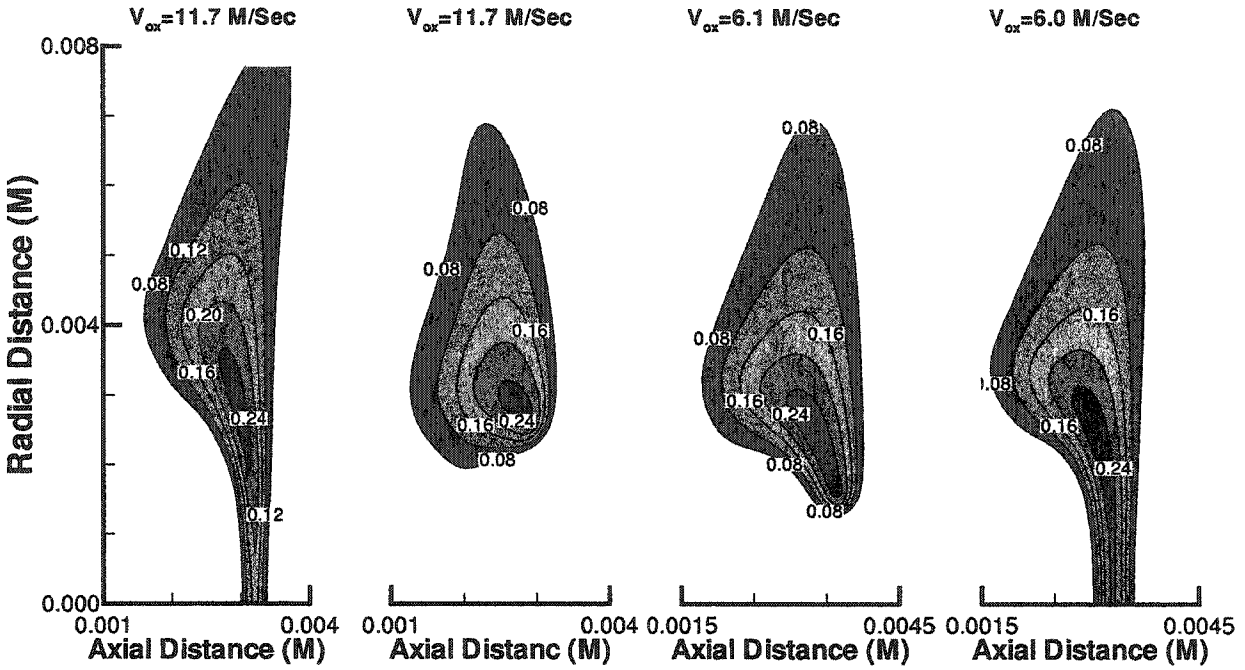

Fig. 6.9 H_2O mole fraction isocontours of parabolic inflow induced 100% hydrogen-air diffusion and postextinction flames. Oxidizer is on left side.

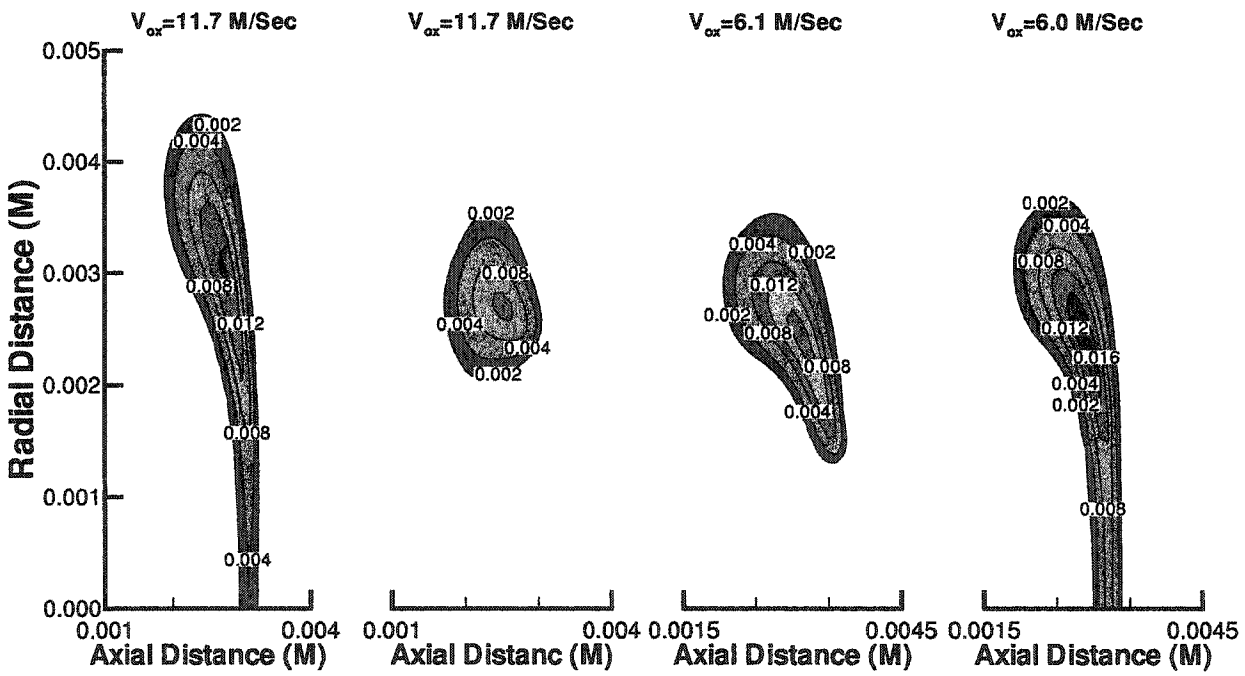

Fig. 6.10 OH mole fraction isocontours of parabolic inflow induced 100% hydrogen-air diffusion and postextinction flames. Oxidizer is on left side.

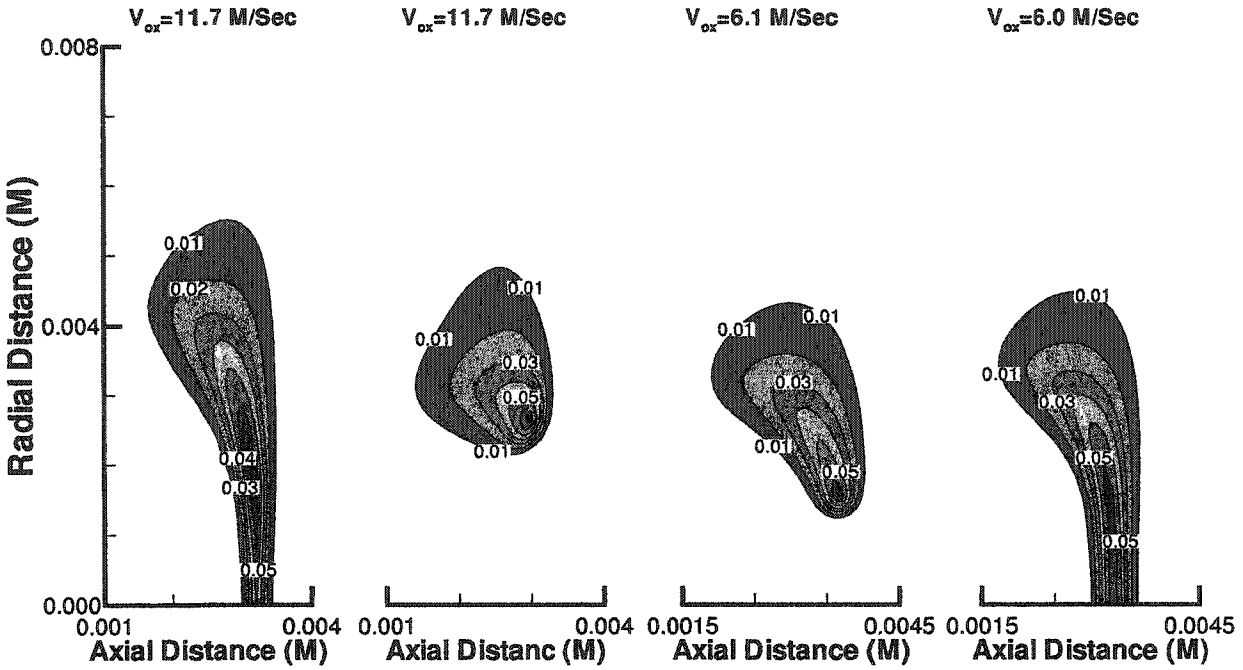

Fig. 6.11 H mole fraction isocontours of parabolic inflow induced 100% hydrogen-air diffusion and postextinction flames. Oxidizer is on left side.

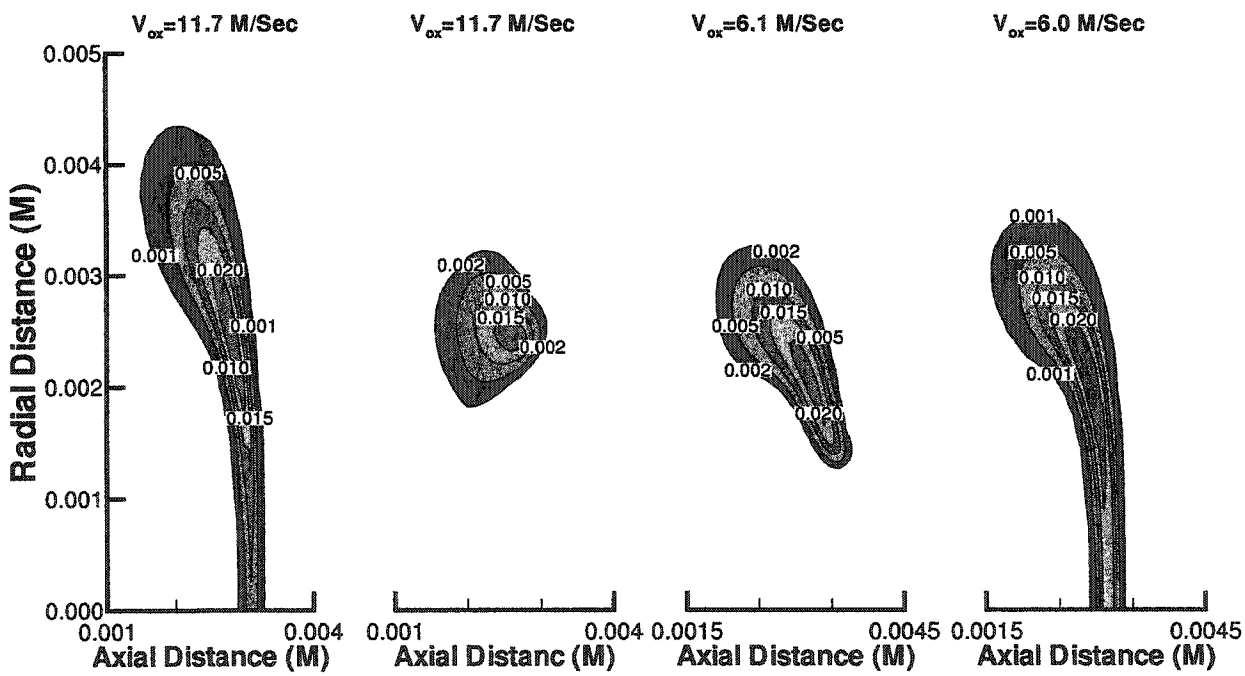

Fig. 6.12 O mole fraction isocontours of parabolic inflow induced 100% hydrogen-air diffusion and postextinction flames. Oxidizer is on left side.

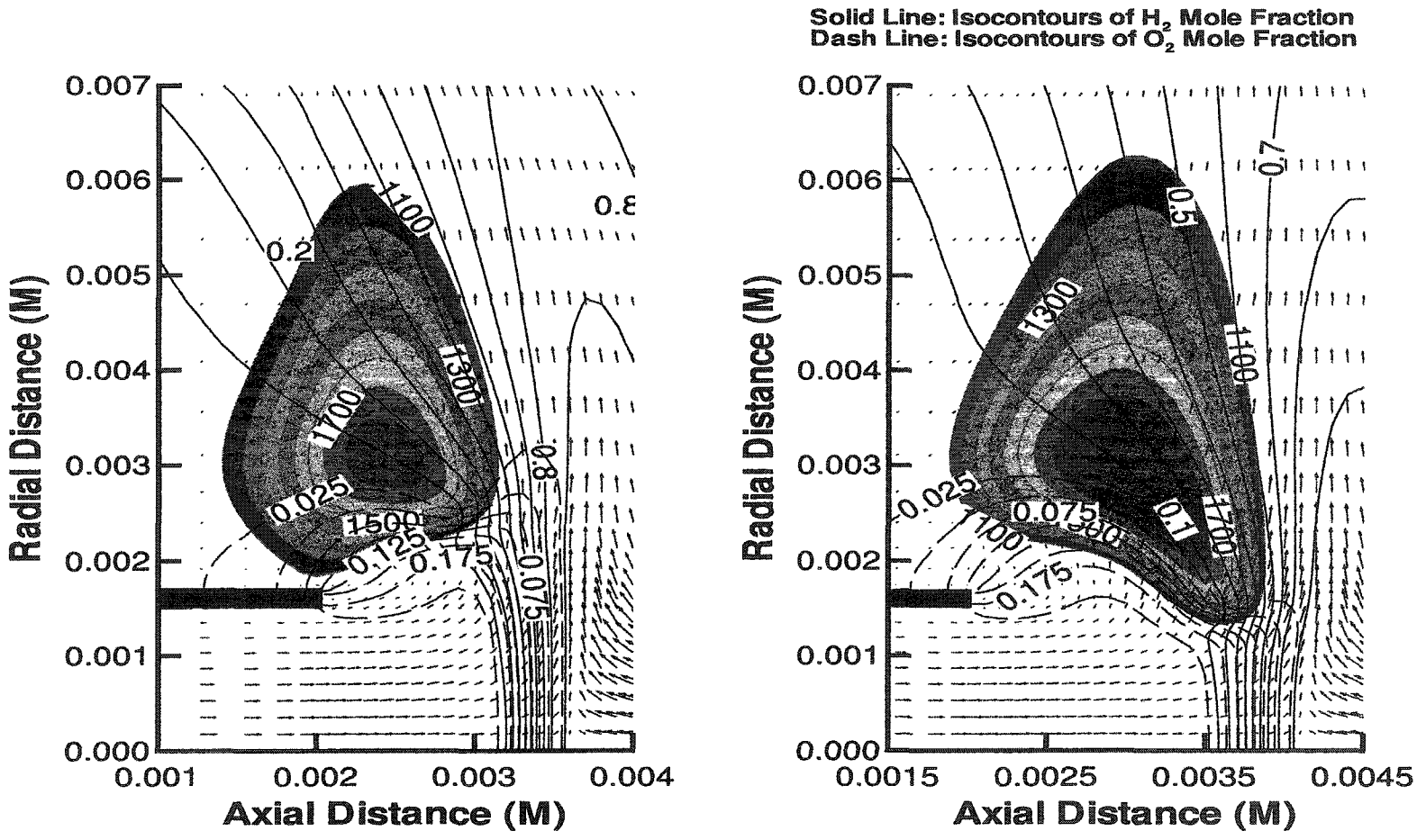

Fig. 6.13 Temperature isocontour and velocity vectors of parabolic inflow induced 100% hydrogen-air postextinction flames at $V_{max,ox}$ =11.7 M/Sec (post-extinction on left) and $V_{max,ox}$ = 6.1 M/Sec (pre-restoration on right) superimposed by fuel and oxidizer isocontour lines. Oxidizer is on left side.

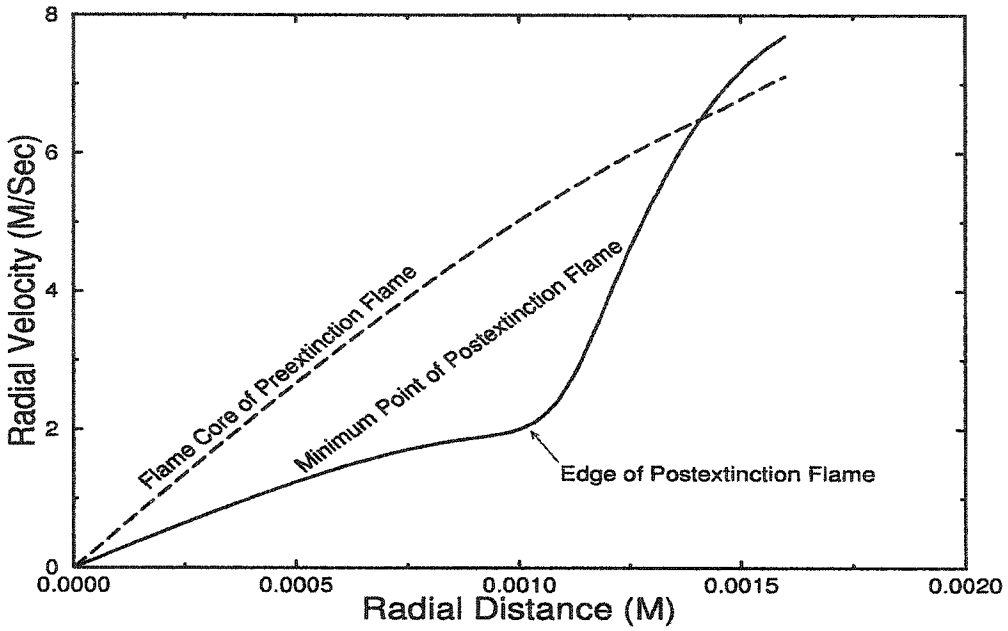

Fig. 6.14 Flame core radial velocity distributions for parabolic inflow induced 100% hydrogen-air diffusion and postextinction flames at centerline oxidizer input velocity of 6.1 M/Sec.

Table 6.1 Various axial centerline strain rates near extinction limit for 100% hydrogen-air opposed jet diffusion flames using Jachimowski kinetic model and parabolic inflows.

$V_{max,ox}$	$V_{mean,ox}/D$	Airside Maximum Axial Strain rate	Flame Core Radial Strain rate	Stagnation Point Radial Strain Rate
7.0	1167	3918	7691	12537
9.0	1500	6173	10210	16475
11.0	1833	7610	12664	21023
11.5	1917	7736	12928	21543
11.7*	1950	7855	13113	22050

Table 6.2 Various axial centerline strain rates near extinction limit for 100% hydrogen-air opposed jet diffusion flames using Yetter et al. kinetic model and parabolic inflows.

$V_{max,ox}$	V_{ox}/D	Airside Maximum Axial Strain Rate	Flame core Radial Strain Rate	Stagnation point Radial Strain Rate
9.0	1500	6127	10274	16790
11.0	1833	7726	11126	21007
12.0	2000	8421	11987	23461
12.7	2117	8860	12649	25060
12.9*	2150	8947	13034	25510

Table 6.3 Axial centerline peak temperatures and species mole fractions near extinction limit for 100% hydrogen-air opposed jet diffusion flames using Jachimowski kinetic model and parabolic inflows.

V_{ox}	MLSR (1/S)	T (K)	H	H_2O	O	OH
7.0	3918	1550	0.07227	0.2491	0.01998	0.009068
9.0	6173	1445	0.06947	0.2329	0.01756	0.007263
11.0	7610	1325	0.06274	0.2070	0.01336	0.005178
11.5	7736	1280	0.05787	0.1946	0.01133	0.004438
11.7*	7855	1241	0.05244	0.1821	0.00967	0.003928

Table 6.4 Axial centerline peak temperatures and species mole fractions near extinction limit for 100% hydrogen-air opposed jet diffusion flames using Yetter et al. kinetic model and parabolic inflows.

$V_{max,ox}$	MLSR (1/S)	T (K)	H	H_2O	O	OH
9.0	6127	1551	0.06645	0.2411	0.01853	0.009099
11.0	7726	1480	0.06485	0.2233	0.01577	0.007477
12.0	8421	1381	0.06040	0.2091	0.01367	0.006465
12.7	8860	1331	0.05204	0.1897	0.01094	0.005410
12.9*	8947	1260	0.04483	0.1745	0.00882	0.004498

CHAPTER VII

CONCLUSIONS

The counterflow diffusion flame begins as initially separated fuel and oxidizer inter-diffuse and react in an aerodynamically strained interface region. The flame burning process often depends more upon the rate of diffusive transport than the rates of chemical reactions. In such cases, the combustion rate increases with diffusion rate, which is strongly dependent on the aerodynamic flows.

In this study, a detailed two dimensional numerical technique is utilized to characterize the extinction limit of 100% hydrogen-air opposed jet diffusion flames at two extremes of input flow boundary conditions, namely, plug and parabolic. The counterflow diffusion flame is simulated using both the Jachimowski (1992) and the Yetter et al. (1994) kinetic chemical models.

First, the simulated flames show excellent agreement in the spatial distribution of centerline temperature and major species concentrations, with independent UV-Raman scattering measurements, in 50% and 100% hydrogen/nitrogen versus air flames, at various input strain rates. The Yetter et al. model leads to more accurate predictions. Also, as the flame becomes more strained, the predicted centerline peak OH concentration deviates more from the measurements, but the width of each profile is more closely predicted.

Second, the extinction state of a 100% hydrogen-air parabolic input flow flame is very well predicted, having near identical agreement (within 5%) with independent averaged measurements of global applied stress rates. Relatively, the Jachimowski kinetic model predicts flame

extinction at slightly higher temperature and lower applied stress rate (-5.1%) than the Yetter et al. model (+4.7%), although their difference is statistically not distinctive.

Third, the near extinction state of 100% hydrogen-air plug or parabolic inflow counterflow flames is predicted best, on a fundamental basis, through the flame core maximum radial strain rate. That is, flame extinction occurs at near identical rates independent of the inflow boundary types (13198/second for plug inflows and 13113/second for parabolic inflow, using Jachimowski model). However, the flame core strain rate is also strongly dependent on the kinetic model (14531/second for plug inflows and 13034/second for parabolic inflows, using Yetter et al. model). The flame core centerline radial strain rate varies linearly (results in a constant correlation factor when normalized) with either centerline maximum axial strain rate or oxidizer-side flow average global applied stress rate, at or near the extinction state. Thus, both strain rate factors provide alternate measurement methodologies for characterizing flame extinction.

However, the respective radial and axial strain rate correlation factors vary significantly with the input flow boundary types. The plug input boundary flame results in a slightly smaller normalized radial strain rate in the flame core (1.56) than the axial strain rate (1.69), based on global applied stress rates and Yetter et al. kinetics. The parabolic inflow flame results in a much larger normalized radial strain rate (6.06) that is slightly larger than the normalized axial strain rate (4.16).

In essence, there is no absolute centerline maximum axial strain rate or global axial applied stress rate that uniquely defines the extinction state of a 100% hydrogen-air counterflow diffusion flame, independent of the input flow boundary types. Only the absolute radial strain rate in the flame core appears to be approximately universal.

For both input boundaries, the flame core maximum radial strain rate does not equal the "classical" one-half of the centerline maximum axial strain rate, near the extinction state. Thus for the extreme case of 100% hydrogen-air flames, which are located far on the airside, this one-half "rule" associated with the one-dimensional stream-function approximation (Heimentz or potential flow) method appears invalid. However, this one dimensional "rule" *is* only observed here for both plug and parabolic inflows with *nonreacting* jet impingement cases.

In this study, the centerline flame extinction temperatures also differ from plug to parabolic inflows, even though the radial strain rates in the flame core are approximately identical. The parabolic input boundary flame has an extinction locus point on the axial centerline on a flame symmetry line. Similarly, the plug input boundary flame has an extinction locus point of the centerline, but the flame temperature also tends to minimize at one radii downstream on the flame symmetry line. Thus, the minimum temperature that is seen at the edge (1 radii) of the plug inflow induced flame is piloted by flame radicals, generated from the centerline flame region, which still control extinction.

Finally, the ring-shaped post-extinction flame is observed as the stretching limit of the parabolic input velocity of a counterflow flame is exceeded beyond the critical point. The post-extinction flame is tribrachial, displaying a quite different flame structure than the typical counterflow diffusion flame. Flame restoration at the center (diffusion flame) is achieved at one half of the extinction applied stress rate, which is in a good agreement with independent measurement data. Detailed results clearly illustrate a large hysteresis in the formation of two distinct flames at an identical (parabolic) inflow condition. Thus, the strain rate itself is not sufficient to characterize the local state of a "laminar flamelet" for a turbulent diffusion flame.

REFERENCES

1. Drummond, J., and Carpenter, M., "Mixing and Mixing Enhancement in Supersonic Reactor Flowfields", AIAA Journal, Vol. 137, 1991, pp.383-455.

2. Gibson, C., "Laboratory, Numerical, and Oceanic Fossil Turbulence in Rotating and Stratified Flow", Journal of Geophysical Research-Oceans, Vol. 96, 1991, 12549-12566.

3. Libby, P., and Williams, F., Fundamental Aspects of Turbulent Reacting Flows, Topics inApplied Physics, springer-Verlag, Vol. 44, NY, 1980.

4. Linan, A., and Williams, F., Fundamental Aspects of Combustion, Oxford University Press, London, 1993.

5. Peters, N., "Laminar Flamelet Concepts in Turbulent Combustion", Twenty First Symposium (International) on Combustion, 1986, pp.1231-1250.

6. Liew, S. and Bray, N., "A Stretched Laminar Flamelet Model of Turbulent Nonpremixed Combustion", Combustion and Flame, Vol. 56, 1984, pp.199-213.

7. Tsuji, H., "Counterflow Diffusion Flames", Progress in Energy and Combustion Science, Vol. 8, 1982, pp.93-119.

8. Burke, S., and Schumann, T., "Diffusion Flames", First Symposium on Combustion, The Combustion Institute, Pittsburgh, 1928, p. 2.

9. Gutheil, E., and Williams, F., "A Numerical and Asymptotic Investigation of Structures and Extinction of Hydrogen-Air Diffusion Flames at Pressures and Temperatures of High Speed Combustion", Twenty Third Symposium (International) on Combustion, 1990, pp. 513-521.

10. Smooke, M., Reduced Kinetic Mechanisms and Asymptotic Approximations for Methane-Air Flames, Springer-Verlag, NY, 1991

11. Dixon-Lewis, G., and Missaghi, M., "Structure and Extinction Limits of Counterflow Diffusio Flames of Hydrogen-Nitrogen Mixtures in Air", Twenty Second Symposium (International) on Combustion, 1988, pp1461-1470.

12. Balakrishnan, G., Trevino, C., and Mauss, F., "The Asymptotic Structure of Hydrogen-Air Diffusion Flame", Twenty Fourth Symposium (International) on Combustion, 1992, pp1893-1900.

13. Kim, J., Libby, P., and William, F., "On the Displacement Effects of Laminar Flames", Combustion Science and Technology, Vol. 87, 1992, pp. 1-25.

14. Potter, A. and Butler, J., "A Novel Combustion Measurement Based on the Extinguishment of Diffusion Flames", American Rocket Science Journal, Vol. 29, 1959, pp.54-56

15. Pellett, G., Northam, G., Guerra, R., Wilson, L., Jarrett, O., Antcliff, R., Dancy, C., and Wang, J., "Opposed Jet Diffusion Flames of Nitrogen Diluted Hydrogen vs. Air:Axial LDA and CARS Surveys; Fuel/Air Strain Rates at Extinction", AIAA-89-2522, 1989.

16. Pellett, G., Northam, G., and Wilson, L., "Counter Diffusion Flames of Hydrogen plus Methane, Ethylene, Propane, and Silane vs. Air: Strain Rate at Extinction", AIAA-91-0370, 1991.

17. Pellett, G., Issac, K., Humphreys, W., Gartrell, L., Roberts, W., Dancey, C., and Northam, G., "Velocity and Thermal Structure and Strain Induced Extinction of 14 to 100% Hydrogen-Air Counterflow Diffusion Flames", Combustion and Flame, Vol. 112, 1998, pp.575-592.

18. Wehrmeyer, J., Yeralan, S., and Tecu, S., "Influence of Strain Rate and Fuel Dilution on Laminar Nonpremixed Hydrogen-Air Flame Structure: An Experimental Investigation", Combustion and Flame, Vol. 107, 1996, pp.125-140.

19. Brown, T., Nandula, S., Skaggs, P., Pitz, R., Pellett, G., Roberts, W., Wilson, L., and Issac, K., "Multi-Point Measurement of Temperature and Species Concentrations in Opposed Jet Flame by UV Raman Scattering", AIAA-94-00226, January 1994.

20. Wehrmeyer, J., Cheng, T., Pitz, R., Nandula, S., Wilson, L., and Pellett, G., "Simultaneous Temperature and Multi-Spaces Measurements in Opposed Jet Flames of Nitrogen-Diluted Hydrogen and Air", The Combustion Institute: Central State Section, Nashville, TN, April 21-24, 1991.

21. Pai, C., Yeralan, S., and Wehrmeyer, J., "Experimental Investigation of Strained Hydrogen-Air Diffusion Flames", The Combustion Institute: Central State Section, New Orleans, LA, March 15-17, 1993.

22. Katta, V., and Roquemore, W., "Response of Hydrogen-Air Opposed Jet Diffusion Flame to Different Types of Perturbations", Proceedings of the Combustion Institute, Vol. 28, 2000, pp. 2055-2062.

23. Fiechtner, G., Carter, C., Katta, V., Gord, J., Donbar, J., and Rolon, J. "Regimes of Interaction Between a Nonpremixed Hydrogen-Air Flame and an Isolated Vortex", AIAA 99-0320, January, 1999.

24. Welle, E., Roberts, W., Decroix, M., Carter, C., and Donbar, J., "Simultaneous Particle-Image Velocimetry and OH Planar Laser-Induced Fluorescence Measurements in an Unsteady Counterflow Propane/Air Diffusion Flame", Proceedings of the Combustion Institute, Vol. 28, 2000, pp.2021-2027.

25. Yeo, S., and Dancey, C., "Experimental Determinations of the Velocity and Strain Rate Field in a Laminar H_2/Air Counter-flow Diffusion Flame via LDA", ASME Publication, Vol. 1, 1991, pp. 121-129.

26. Dancey, C., and Long, S., "Experimental Investigation of the Strain Rate Field in Stretched Laminar H_2/Air Diffusion Flames", AIAA 93-3068, July, 1993.

27. Pellett, G., Roberts, W., Wilson, L., Humphreys, W., Bartram, S., and Isaac, K., "Structure of Hydrogen-Air Counterflow Diffusion Flames Obtained by Focusing Schlieren, Shadowgraph, PIV, Thermometry, and Computation", AIAA 94-2300, 1994.

28. Hahn, W., Wendt, J., and Tyson, T., "Analysis of the Flat Laminar Opposed Jet Diffusion Flame with Finite Rate Detailed Chemical Kinetics", Combustion Science and Technology, Vol. 27, 1981, pp.1-17.

29. Dixon-Lewis, G., Gaskell, P., Fukutani, S., Jinno, H., Miller, J., Kee, R., Smooke, M., Peters, N., Effelsberg, E., Warnatz, J., and Behrendt, F., "Calculation of the Structure and Extinction Limit of a Methane-Air Counterflow Diffusion Flame in the Forward Stagnation Region of a Porous Cylinder", Twentieth Symposium (International) on Combustion, 1984, pp.1893-1904.

30. Kee, R., Miller, J., Evans, G., and Dixon-Lewis, G., "A Computational Model of the Structure and Extinction of Strained Opposed Flow Premixed Methane-Air Flames", Twenty Second Symposium (International) on Combustion, 1988, pp.1479-1494.

31. Dixon-Lewis, G., "Structure of Laminar Flames", Twenty Third Symposium (International) on Combustion, 1990, pp.305-324.

32. Zhao, J. and Issac, K., "Global Characteristics and Structure of Hydrogen Air Counter Flow Diffusion Flames", AIAA-94-0680, January 1994.

33. Ho, Y., Issac, K., Pellett, G., and Northam, G., "Analysis of Opposed Jet Hydrogen-Air Counterflow Diffusion Flame", AIAA-91-0582, 1991.

34. Chelliah, H., Law, C., Ueda, T., Smooke, M., and Williams, F., "An Experimental and Theoretical Investigation of the Dilution, Pressure and Flowfield Effects on the Extinction Condition of Methane-Air-Nitrogen Diffusion Flames", Twenty Third Symposium (International) on Combustin, 1990, pp. 503-521.

35. Balakrishnan, G., "Studies of Hydrogen-Air Diffusion Flames and of Compressibility Effects Related to High Speed Propulsion", Ph. D. Dissertation, University of California, San Diego, CA, 1992.

36. Papas, P., Glassman, I., and Law, C., "Effects of Pressure and Dilution on the Extinctionof Counterflow Nonpremixed H_2-Air Flames", Twenty Fifth Symposium (International) on Combustion, 1994, pp. 1333-1339.

37. Darabiha, N., and Candel, S., "The Influence of the Temperature on Extinction and Ignition Limits of Strained Hydrogen-Air Diffusion Flames", Combustion Science and Technology, Vol. 86, 1992, pp. 67-85.

38. Daguse, T., Croonenbroek, T., Rolon, J., Darabiha, N., and Soufiani, A., "Study of Radiative Effects on Laminar Counterflow $H_2/O_2/N_2$ Diffusion Flames", Combustion and Flame, Vol. 106, 1996, pp. 271-287.

39. Gutheil, E., Balakrishnan, G., and Williams, F., "Structure and Extinction of Hydrogen-Air Diffusion Flames", in Reduced Kinetic Mechanisms for Application in Combustion Systems, Springer, London, 1992.

40. Zhao, J., "Numerical Analysis of Hydrogen-Air Counter Flow Diffusion Flame", Ph D. Dissertation, University of Missouri-Rolla, May 1995.

41. Zhao, J., and Isaac, K., "Influence of Geometry and Heat Release on Counterflow Diffusion Flames: A Navier-Stokes Model", AIAA-95-0133, January, 1995.

42. Balakrishnan, G., Tree, D., and Williams, F., "An Experimental Investigation of Strain Induced Extinction of Diluted H_2-Air Counterflow Diffusion Flames", Combustion and Flame, Vol. 98, 1994, pp. 123-126.

43. Takagi, T., Yoshikawa, Y., Yoshida, K., Komiyama, M., and Kinoshita, S., "Studies on Strained Non-Premixed Flames Affected by Flame Curvature and Preferential Diffusion", Twenty Sixth Symposium (International) on Combustion, 1996, pp.1103-1110.

44. Kim, Y., and Kim, H., "Multidimensional Effects on Structure and Extinction Process of Counterflow Nonpremixed Hydrogen-Air Flame", Combustion Science and Technology, Vol. 137, 1998, pp.51-80.

45. Frouzakis, C., Lee, J., Tomboulides, A., and Boulouchos, K., "Two Dimensional Direct Numerical Simulation of Opposed Jet Hydrogen-Air Diffusion Flame", Twenty Seventh Symposium (International) on Combustion, 1998, pp.571-577.

46. Lee, J., Frouzakis, C., and Boulouchos, K., "Two Dimensional Direct Numerical Simulation of Opposed Jet Hydrogen/Air Flames: Transition from a Diffusion to an Edge Flame", Proceedings of the Combustion Institute, Vol. 28, 2000, pp. 801-806.

47. Frouzakis, C., Tomboulides, A., Lee, J., and Boulouchos, K., "From Diffusion to Premixed Flames in an H_2/Air Opposed-Jet Burner: The Role of Edge Flames", Combustion and Flames, Vol. 130, 2002, pp. 171-184.

48. Clarke, J., "On the Structure of a Hydrogen-Oxygen Diffusion Flame", Journal of Proceeding Royal Society, Vol. 307A, 1963, pp. 283-302.

49. Kim, T., Yetter, R., and Dryer, F., "New Results on Moist CO Oxidation: High Pressure, High Temperature: Experiments and Comprehensive Kinetic Modeling", Twenty Fifth Symposium (International) on Combustion, 1994, pp.759-766.

50. Jachimowski, C., "An Analysis of Combustion Studies in Shock Expansion Tunnels and Reflected Shock Tunnels", NASA-TP-3224, 1992.

51. Choi, Y., and Merkle, C., "The Application of Preconditioning in Viscous Flows", Journal of Computational Physics, Vol. 207, 1993, pp. 207-233

52. Turkel, E., "Preconditioning Techniques in Fluid Dynamics", Annual Review of Fluid Mechanics, Vol. 31, 1999, pp. 385-416.

53. Jenny, P., and Muller, B., "Convergence Acceleration for Computing Steady-State Compressible Flow at Low Mach Numbers", Computers and Fluids, Vol. 28, 1999, pp.951-972.

54. McBride, B., Gordon, S., and Reno, M., "Coefficients for Calculating Thermodynamics and Transport Properties of Individual Species", NASA TM 4513, February1993.

55. Svehla, R., "Estimated Viscosities and Thermal Conductivities of Gases at High Temperatures" NASA-TR-R-132, October, 1961.

56. Wilke, C., "A Viscosity Equation for Gas Mixtures", Journal of Chemical Physics, Vol.18, No. 1, 1950, pp. 517-519

57. Bird, R., Stewart, W., and Lightfoot, E., Transport Phenomena, John Wiley, and Sons, 1960

58. Warnatz, J., "Survey of Rate Coefficients in C/H/O systems", in Combustion Chemistry, Springer-Verlag, NY, 1985.

59. Hsu, K., Anderson, S., Durant, J., Kaufman, F., "Rate Constants for $H+O_2+M$ from 298 to 639K for M=He, N, and H_2O", Journal of Chemical Physics, Vol. 93, 1984, pp. 1018-1025.

60. Shuen, J., Chen, K., and Choi, Y., "A Coupled Implicit Method for Chemically Non-Equilibrium Flows at All Speeds", Journal of Computational Physics, Vol. 106, 1993, pp.306-318.

61. Anderson, D., Tannehill, J., and Pletcher, R., Computational Fluid Mechanics and Heat Transfer, Hemisphere Publishing Co., NY, 1984.

62. Kreutz, T., and Law, C., "Ignition in Nonpremixed Counterflowing Hydrogen Versus Heated Air: Computational Study with Skeletal and Reduced Chemistry", Combustion and Flame, Vol. 114, 1998, pp. 436-456.

63. Pellett, G, and Wilson, L., Humphreys, J., Bartram, S., Dartrell, L., and Issac, K., "Velocity Fields of Axisymmetric Hydrogen-Air Counterflow Diffusion Flames from LDV, PIV, and Numerical Computation", AIAA-95-3112, July, 1995.

64. Yetter, R., Dryer, F., and Rabitz, H., "A Comprehensive Reaction Mechanism for Carbon Monoxide/Hydrogen/Oxygen Kinetics", Combustion Science and Technology, Vol. 79, 1991, pp.97-128.

65. Egolfopoulos, F, and Law, C., "An Experimental and Computational Study of the Burning Rates of Ultra Lean to Moderately Rich $H_2/O_2/N_2$ Laminar Flames with Pressure Variations", Twenty Third Symposium (International) on Combustion, 1990, pp.333-340.

66. Kioni, P., Rogg, B., Bray, K., and Linan, A., "Flame Spead in Laminar Mixing Layers: The Triple Flame", Combustion Flame, Vol. 95, 1993, pp. 276-290.

67. Glassman, I., Combustion, 2nd ed., Academic Press, London, 1987.

68. Kuo, K., Principle of Combustion, John Wiley & Sons, NY, 1986.

CURRICULUM VITA

EDUCATION

Doctor of Philosophy in Mechanical Engineering
Old Dominion University, Norfolk, Virginia, May 2003

Master of Science in Mechanical Engineering
Old Dominion University, Norfolk, Virginia, December 1995

Bachelor of Science in Mechanical Engineering
Virginia Polytechnique Institute and State University, Blacksburg, Virginia, May 1992

SELECTED PUBLICATIONS

Hwang, K., and Tiwari, S., "Extinction of Hydrogen-Air Opposed Jet Laminar Diffusion Flames", AIAA2001-2824, June, 2001.

Hwang, K., and Tiwari, S., "Parametric Study of Moderately Strained Hydrogen-Air Opposed Jet Laminar Diffusion Flames", AIAA2001-1079, January, 2001.

Hwang, K., and Tiwari, S., "Two Dimensional Simulation of Hydrogen-Air Opposed Jet Diffusion Flames", AIAA2000-0579, January, 2000.

Hwang, K., and Tiwari, S., "Effects of Tube Wall Thickness Interaction with Nitrogen Diluted Hydrogen-Air Opposed Jet Flows", AIAA99-3750, June, 1999.

Hwang, K., and Tiwari, S., "Numerical Study of Atomic Oxygen Formation in a Reflective Shock Tube", AIAA98-0552, January, 1998.

Hwang, K., "Effects of Inlet Deflector Geometry Variations in the Flowfield", M.S. Thesis, Old Dominion University, December, 1995.